Final Project Report 10/2015 - 9/2020 – Award No. DE-FE0025315

Final Project Report:
A Joint Experimental/Computational Study of Non-Idealities in Practical Rotating Detonation Engines

Principal Investigator:

Mirko Gamba and Venkat Raman

Department of Aerospace Engineering
University of Michigan

Contents

Chapter 1

Objectives and Motivation

1.1 Project Goal and Objectives

The overall goal of this work is to understand non-ideal effects in practical rotating detonation engines (RDEs) that impede the realization of theoretical detonation cycle efficiencies. The main limitations in RDE operability and performance are associated with practical design considerations, where non-idealities, such as incomplete mixing, fuel leakage, secondary deflagration, instabilities and geometry-dependent effects, reduce the effectiveness of the detonation-based compression cycle. The goal of this work is to take a fundamental point of view, and use detailed experiments and simulations to understand non-ideal effects, their contribution to loss in pressure gain, and RDE operability limitations.

Current research is mainly focused on design and overall operability of RDEs. Our approach is instead to look at the physics of basic processes occurring in RDEs. In particular, we consider processes associated with non-idealities and we use a combination of the laser and non-laser diagnostics and large eddy simulation/direct numerical simulation computations to investigate these underlying phenomena. By advancing the fundamental science of detonation wave propagation in RDE flowfiels, and subject to non-ideal conditions, will enable design to progress more rapidly.

This work is a collaborative work involving experiments, simulations and external domain experts to understand the physics behind RDEs and non-idealities. Through collaboration between experimentalists and modelers, we have developed targeted experiments to investigate fundamental aspects of the operation of an RDE. Furthermore, we have developed advanced combustion models that account for non-ideal effects in the operation of an RDE and are able to capture the complexities of realistic RDE configurations. We conduct detailed experiments to investigate the flame structure ahead and behind detonation fronts in the presence of non-uniform or incomplete mixing, leakage and secondary combustion. We use optical and laser diagnostics to identify the structure of the detonation wave. We consider different working parameters, such injection scheme, geometry, flow rates and equivalence ratios. We brought in DNS/LES capabilities to RDE design by specifically incorporating detailed kinetics and pressure-sensitive combustion physics, thus improving upon current practice based on an Euler equations description that do not take into account viscous effects, while the combustion process is introduced using an induction time based global ignition model. These current models lack the capability of capturing non-ideal mixing and fuel stratification effects. Furthermore, the significant changes in pressure within the domain due to the detonation requires combustion models with time-varying pressure effects. In this regard, using DNS with detailed chemistry, and developing LES-based combustion models for complex geometries with detonation wave has enable to understand some of the underlying phenomena controlling the operation of these devices.

The main objectives of the project are as follows:

- Objective 1. Develop canonical and operational RDE configurations, as well as imaging-based diagnostics for understanding fuel stratification, leakage, deflagration and detonation structure under non-ideal conditions in RDEs.
- Objective 2. Develop detailed computational tools (DNS & LES) for studying detonation wave propagation processes in RDEs.
- Objective 3. Develop a comprehensive picture of the fundamental physics governing non-idealities and how they impact RDE performance and operability from both experiments and simulations.

1.2 Outcomes of the Work

The major outcomes of this project are:

- Development of testing infrastructure for RDEs, including a modular 6 inch RDE and a 12 inch equivalent optical RDE (race track RDE);
- Experimental measurements of detonation and deflagration structure and distribution using laser diagnostics in RDE flows;
- DNS/LES modeling of RDE operation under non-ideal conditions;
- LES models for detonation wave propagation in non-uniform and fuel-stratified RDE configurations;
- Fundamental understanding and quantification of non-idealities in RDE operation due to incomplete mixing, deflagratation (secondary combustion), viscous effects, and fuel leakage;
- Identification of secondary combustion (deflagration) phenomena, classified as parasitic and commensal combustion, and its impact on RDE operation;
- Implementations of models into open source computational platform;

- Public dissemination of results, data and models.

The following is a current list of publications based on work that originates from this project:

- Prakash, S., Fievet, R., Raman, V., Burr, J., and Yu, K. H., "Analysis of the Detonation Wave Structure in a Linearized Rotating Detonation Engine", AIAA Journal Special Issue on Continuous Detonation and its Applications, October 2019.
- Takuma Sato and Venkat Raman, "Dynamics of rotating detonation engines with a pintle-type injector ", ISABE-2019, Canberra, Australia, Sept. 2019.
- Chacon, F. and Gamba, M., "OH PLIF Visualization of an Optically Accessible Rotating Detonation Combustor," AIAA Propulsion and Energy Forum 2019.
- Feleo, A., Chacon, F. and Gamba, M., "Effects of Heat Release Distribution on Detonation Properties in a H_2/Air Rotating Detonation Combustor from OH* Chemiluminesence," AIAA Propulsion and Energy Forum 2019.
- Chacon, F., Feleo, A., and Gamba, M., "Effect of Parasitic and Commensal Combustion on Rotating Detonation Combustor Properties," 27th ICDERS, Beijing, China, July 2019.
- Prakash, S. and Raman, V., "Detonation Propagation through Inhomogeneous Fuel-air Mixtures," 27th ICDERS, Beijing, China, July 2019.
- Feleo, A., Chacon, F. and Gamba, M., "Evaluation of OH Emissoin in an Optical Accessible Continuous Wave Rotating Detonation Engine," AIAA Scitech 2019.
- Chacon, F. and Gamba, M., "Study of Parasitic Combustion in an Optically Accessible Continuous Wave Rotating Detonation Engine," AIAA Scitech 2019.
- Prakash, S., Fievet, R., and Raman, V., "The Effect of Fuel Stratification on the Detonation Wave Structure," AIAA Scitech 2019, San Diego, CA, USA, January 2019.
- Prakash, S., Fievet, R., Raman, V., Burr, J., and Yu, K. H., "Characterisation of the Detonation Wave Structure in a Linearized RDE Combustor Channel," 71st APS Division of Fluid Dynamics, Atlanta, GA, USA, November 2018.

- Chacon, F. and Gamba, M., “Development of an optically accessible continuous wave Rotating Detonation Engine,” 2018 AIAA Propulsion and Energy Conference, 2018.

- Supraj Prakash, Romain Fiévet, Venkat Raman, Jason Burr, and Kenneth H. Yu, “Numerical Study of the Detonation Wave Structure in a Linear Model Detonation Engine”, 2018 AIAA Propulsion and Energy Conference, Paper No. AIAA 2018-4966.

- James Duvall and Mirko Gamba, “Characterization of Reactant Mixing in a Rotating Detonation Engine Using Schlieren Imaging and Planar Laser Induced Fluorescence” 2018 AIAA Propulsion and Energy Conference.

- Takuma Sato, Stephen Voelkel, and Venkat Raman, “Detailed Chemical Kinetics Based Simulation of Detonation-Containing Flows,” 2018 ASME Turbo Expo, Turbomachinery Technical Conference and Exposition,” American Society of Mechanical Engineers, 2018, p. V04AT04A063

- James Duvall, Fabian Chacon, Chadwick Harvey and Mirko Gamba, “Study of the effects of various injection geometries on the operation of a rotating detonation engine”, 2018 AIAA Scitech, Paper No. AIAA 2018-0631

- Fabian Chacon and Mirko Gamba, “Shock propagation through a stratified gas”, 2018 AIAA Scitech, Paper No. AIAA 2018-0880

- Fabian Chacon and Mirko Gamba, “Shock propagation and mixing through a stratified gas”, Presented at the APS DFD meeting, November 2017

- Fabian Chacon, James Duvall and Mirko Gamba, “Effect of fuel injection scheme on rotating detonation engine operation”, Presented at the APS DFD meeting, November 2017

Chapter 2

Experimental activities

2.1 Overview

For the work described here, we utilized two main RDC systems supported by the same experimental facility. The first is a traditional round configuration RDC, while the second was an optically accessible race track configuration RDC (RT-RDC). The two devices were first characterized to establish their baseline behaviors and to ensure they behaved similarly to one another so that measurements made in one could be translated to the other with minimal caveats. Once they were described, observations and measurements made in both devices lead to a greater understanding of secondary combustion phenomena present within RDCs.

Secondary combustion was categorized into two different forms: parasitic combustion (before detonation wave) and commensal combustion (after detonation wave). This distinction was made because the two types of secondary combustion have different impacts on the resulting detonation properties present within an RDC and will ultimately impact any potential efficiency benefits differently. These types of combustion have been quantified for our axial injection scheme and have found that as more of the heat release is associated with the detonation the more 'ideal' the detonation wave behaves, in accordance with our 0D models of the secondary combustion phenomena.

2.2 Experimental RDC facility

A purpose built test facility has been constructed at the University of Michigan and all data presented here was collected using this facility. It is composed of the two RDCs used in this work, the supporting air/fuel flow system, as well as a control/DAQ system monitoring a number of measurements. The round RDC has dimensions very similar to those tested at AFRL and NETL [1, 2, 3], while the RT-RDC is designed to mimic the round RDC. The detonation channel has an inner diameter of 138.7 mm (5.46 in), width of 7.7 mm (0.30 in) and a length of approximately 101.6 mm (4 in), which varies slightly for each injection scheme. Below some of the main components of the facility and design are briefly described.

2.2.1 Round RDC

The Round RDC is based around a stackable plate injection scheme. The plates are interchangeable which allows for quick and easy modification for testing a variety of injector types. See Figure 2.1. Reactants are supplied to the injectors through inner and outer plenums. The feed lines may be easily reconfigured to have fuel or air travel through either plenum depending on the injector design. The AAI injector has air travel through the outer plenum while the JIC and SIJ injectors have air supplied to the inner plenum. The injectors considered here have quite different design which may be partially quantified by the injection area ratio, as summarized in Table 2.1. All of the injectors have the same fuel injection area, so this ratio of areas has implications in regards to the necessary inlet pressures and coupling between detonation chamber and feed plenums. A larger area ratio implies potentially greater coupling to the air plenum but less pressure loss in supplying the air from the plenum to the detonation channel. See Figure 2.2 for a comparison of the injectors.

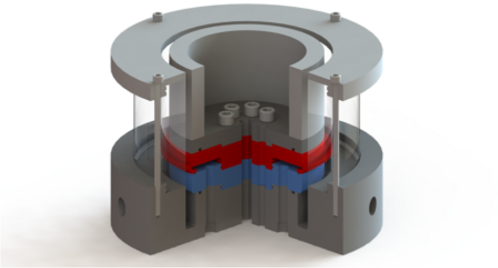

Figure 2.1: Section View of a simplified rendering of the MRDE. Blue and red components are the interchangeable injector plates and the inner plenums are visible in the image.

Injector	Area Ratio (A_{Air}/A_{Fuel})
Pintle	10.3
JIC (AFRL)	4.6
SIJ (ONERA)	1.8

Table 2.1: Area ratios of the injectors in this study.

2.2.1.1 Axial Air Inlet (AAI) Injector

The AAI injector is based on a geometry that was considered in a computational work conducted at the Naval Research Lab [4], which they labeled a pintle injector. The geometry they considered is not a true pintle geometry as one would find in a rocket injector, but shares some geometric similarity. For our purposes we will refer to this geometry as AAI. The flow field consists of air flowing axially over a smooth one-sided contoured surface. This protruding surface results in an annular air slot of 1.6 mm (0.063 in) width. Fuel is injected from an inner plenum into the detonation channel from the upper face of the contour from 120 evenly spaced individual jets arranged around the circumference. Each fuel injection port has diameter of 0.89 mm (0.035 in). The jets are angled and oriented toward the outer wall.

2.2.1.2 Jet in Crossflow (JIC) Injector

The JIC injector is based on the RDC operated by the Air Force Research Lab at Wright Patterson Air Force Base [1, 5]. In this scheme air flows around a chamfered corner expanding radially from an inner plenum. As the flow goes around the corner it passes over fuel injectors that are oriented axially and spaced evenly along the circumference. Our injector has an air slot height of 0.89 mm (0.035 in), and an array of 120 fuel injectors with diameters of 0.89 mm (0.035 in). This corresponds exactly to an RDC configuration tested by AFRL [1]. As such it serves as a benchmark to which other injection schemes can be compared. This design was included because of its extensive use in computational and experimental research in the field, as well as the simplicity of the scheme.

2.2.1.3 Semi-Impinging Jet (SIJ) Injector

The design for the SIJ injector is based on a geometry that was considered in a computational work done at ONERA[6]. The design utilizes staggered jets arranged around the circumference of the detonation channel. The jets are angled toward the center of the channel with oxidizer injecting from the inner radius and fuel from the outer radius. A key feature of the injectors is that the fuel and oxidizer jets are offset in such a way that the jets only overlap over a fraction of their exit area. In this design the injectors are oriented such that they inject towards the middle of the channel, unlike the ONERA scheme where they inject azimuthally. This change was selected for machining considerations. There are 120 fuel and air injectors, with diameters of 0.89 mm (0.035 in) and 1.2 mm (0.047 in) respectively.

2.2.2 Race Track RDC (RT-RDC)

The RT-RDC is an optically accessible RDC designed in the shape of a racetrack comprised of two linear sections combined by two curved semi circle sections. The purpose of this unique shape is for the inclusion of a large viewing window in the straight section of the detonation channel as seen in figure 2.3. The straight section of the device measures 23 cm long with optical access being available over 63.5 mm by 177.8 mm of the straight section detonation channel. This window allows optical

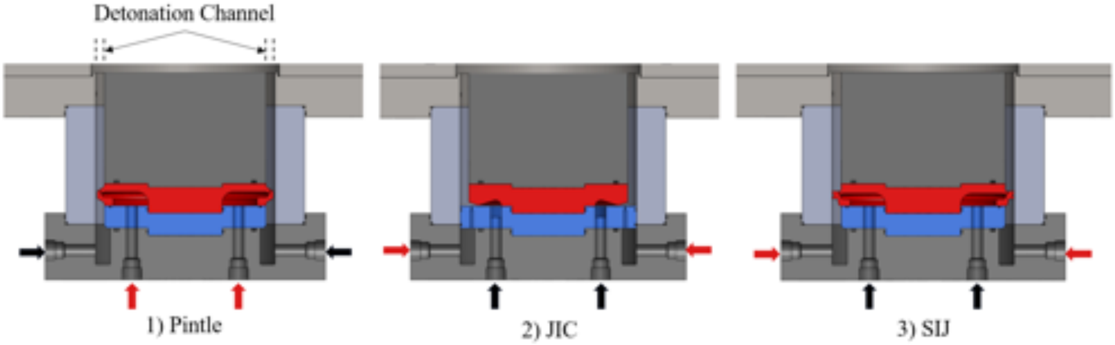

Figure 2.2: Section view of the injectors tested installed in the Round RDC. Red arrows indicate fuel supply while black arrows indicate air supply.

access for approximately the first 45 mm of the detonation channel while allowing access to the main air path constriction and upper air plenum. The detonation channel is capable of laser sheet access through a specially designed second window conformal to one of the curved sectors and makes laser imaging diagnostics possible in a linear fashion without the limited run times of typical linear RDC analogues, typically limited to two or three cycles. Because of the unique design of the detonation channel and optical components, the internal flow remains undisturbed by the presence of the optical access in the flow path. The laser access window is designed such that the laser sheet can be placed parallel to the viewing window at any span-wise plane within the linear section of the detonation channel that lies between the quarter and three quarter point of the channel width.

The internal flow path of the device is nearly identical to the round configuration, with care being taken to maintain the same flow rate per detonation channel perimeter as the round RDC it is meant to emulate. The overall size of the RT-RDC is equivalent to a round RDC having a diameter equal to twice that of the round counterpart. The fuel/oxidizer handling is conducted using an axial air inlet (AAI) flow path with angled fuel injection from a rear-facing contraction of the air inlet. The oxidizer flow path originates from a plenum, and undergoes a converging/diverging contraction before it enters the detonation channel. Fuel is injected through discrete injector portholes organized around the circumference of the contraction at an angle relative to the axial oxidizer direction. Although the mode of operation of the RT-RDC is

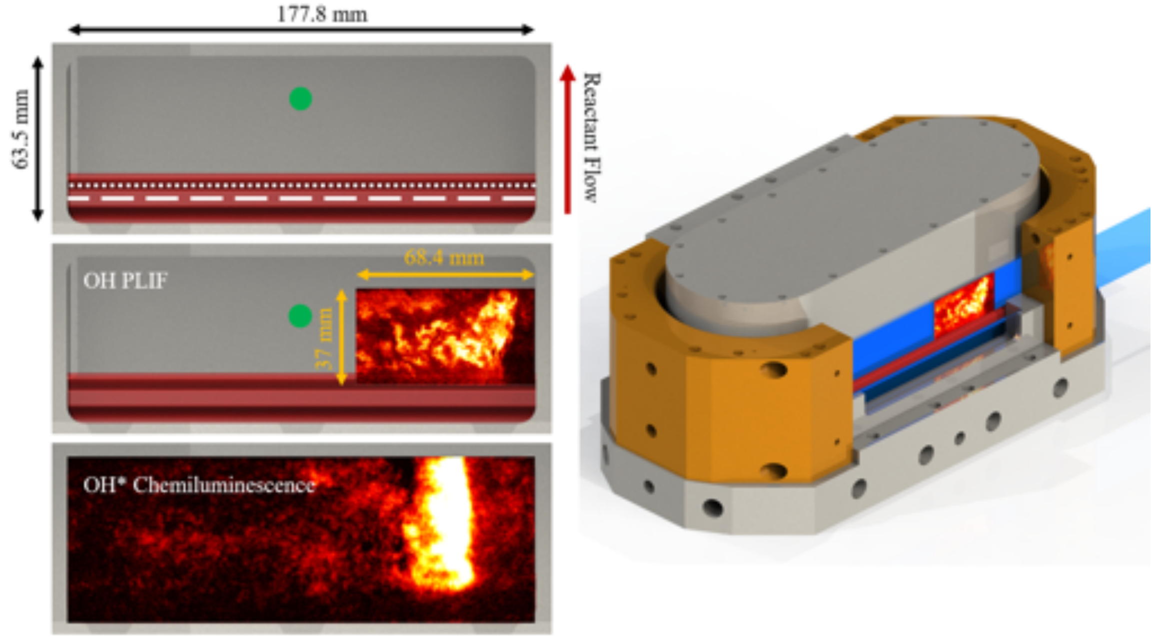

Figure 2.3: Schematic diagram of racetrack rotating detonation combustor showing a schematic of the laser sheet arrangement, the imaging region compared to the whole window. The green dot denotes the location of a high-speed pressure transducer flush mounted in the channel used for synchronization of the OH PLIF images.

found to somewhat differ from the round counterpart, judicious selection of operating conditions (nominally mass flow rates and equivalence ratio) enables to operate the RT-RDC in ways that are very similar to the round counterpart while minimizing undesired secondary effects associated with the racetrack shape of the device.

2.2.3 Air/Fuel Flow System

The test facility utilizes a high pressure air system and high temperature exhaust that can handle up to 1.0 kg/s of air and stoichiometric combustion of hydrogen. Electro-pneumatic solenoid ball valves and precision orifices are used to control and meter the supply of reactants to the device. Electronic pressure controllers are used in conjunction with air loaded regulators to set the fuel and air pressures. The system is capable of handling up to five separate gas streams aside from the air, each metered through a choked orifice and controlled remotely through a solenoid ball valve.

The RT-RDC is directly connected to an exhaust system. Because of the direct connection one of the main design and operation considerations was the design of the ignition sequence. More specifically, one of the main concerns was the potential for hard starts of the system that results from the rapid ignition of the pre-mixed fuel/oxidizer mixture that pass through the RDC without reacting and accumulate into the exhaust. Typically RDC systems use a pre-detonator for their ignition source, which is limited to a small number and low frequency of ignition attempts per experimental run. In order to increase the likelihood of ignition both fuel and oxidizer flow are initiated and allowed to stabilize before lighting of the detonator, this allows for the accumulation of reactants in the exhaust that subsequently can lead to hard starts. To limit this possibility, we have equipped the RT-RDC with an afterburner a few inches downstream of the RT-RDC exhaust plane where it is able to consume any unburnt mixture. Additionally, the afterburner (lighted separately through a small combustion wave igniter) serves as the ignition source for the main combustor. When the RDC fueling sequence is initiated, the flame from the afterburner flashes back into the detonation channel and then transitions into one of the operational modes observed in the RT-RDC. In practice, the RT-RDC is operated similarly to the MRDC.

Solenoid	On Time [s]	Off Time [s]
RDC Air Valve	0	14
RDC Fuel Valve	5.5	10.5
AB Air Valve	0	14
AB Fuel Valve	3	11
Spark Plug	2.25	3.5

Table 2.2: Typical MRDC test sequence used for data acquisition.

2.2.4 System Control and Data Acquisition

Control of all hardware and the operation of the device is conducted using a LabVIEW controller. The controller utilizes a user input timing sequence to activate solenoid ball valves during an experiment to control the flow of reactants to the device as well as the after burner and ignition source. A typical timing sequence is shown below in table 2.2. Depending on the purpose of the experimental run, the timing sequence is adjusted to better suit those needs. Across all experiments, air flow is always maintained throughout the run as a precaution against accidental accumulation of detonatable mixtures in the exhaust system. Runs end with a substantial blow down period following combustion to completely remove all hot products from the exhaust and limit the heat transfer to the exhaust. Lastly, the afterburner is lit well in advance of the main device and continues to operate after the RDC fuel line is completely shut down.

While the controller is actuating ball valves to create the desired test sequence it also records and saves data from installed sensors. Slow speed measurements are taken at 200 Hz with an NI PCI-6259 acquisition card while high speed measurements are taken at 500 kHz with an NI PCI-6133 acquisition card.

Run times for the RT-RDC are five seconds in length, in contrast typical runs on the MRDC are only 1.5 seconds. The reason for this change is also for avoiding hard starts. Igniting the RT-RDC at full flow rates of 1 kg/s have the potential for very large hard start events if unsuccessful; however, any such event at 200 g/s would be relatively harmless. For all RT-RDC runs we have chosen to therefor use a ramping sequence of both the fuel and air streams. The device is initially ignited at a low mass flow rate for both the air and fuel streams at conditions where stable detonating operation can be readily achieved. The device after 1 second of operation is then ramped up to the final testing point (air mass flow rate and equivalence ratio). Typically, at least the last second of the run time has reached a stable value of air and fuel mass flow rates, as well as equivalence ratio. Through this process we are able to achieve stable transitions between test points and safely ramp up to the large flow rates we wish to investigate.

2.2.5 Instrumentation and Measurements

2.2.5.1 Low and High Speed Pressure Sensors

The outer wall of the detonation channel was modified to include instrumentation. This includes 17 CTAPs to measure the axial variation of average pressure along the length of the channel. The taps are 36 inch long, 1/16 inch diameter tubes which attach to each port with a pressure transducer at the far end. The outer wall allows for placement of PCB and water cooled Kulite-EWCTV high speed pressure transducers. Additional high speed Kulite-XTL pressure transducers are placed in the air and fuel injector plenums. Detail on the layout of the CTAP array and outer wall is shown in Figure 2.4. All low speed static pressures are recorded at 200 Hz, while high speed pressure data is collected at 500 kHz.

2.2.5.2 High Speed Chemiluminescence Video

High-frame rate chemiluminescence video of the detonation wave as observed from the exhaust of the RDC were taken with a high-speed CMOS camera (Phantom v711) operating at 55,016 frames per second with an exposure time of 10 μs. The camera used a 50 mm lens to acquire a field of view of about 174 mm × 169 mm with a resolution of 288 × 280 pixels. The camera observed the exit of the RDC axially into the device through a fused quartz window built into the exhaust system from approximately two meters away. The same setup was used for the RT-RDC but with different frame rates and resolutions. Namely operating at 30,008 frames per second with an exposure time of 10 μs. Using a 50 mm lens the field of view captured is 398 mm × 176 mm with a resolution of 688 × 304 pixels. The camera is positioned and focused so as to capture the entire device exit plane, with the camera aligned along the center of the RT-RDC. This alignment creates small solid angles through which light from the curved sections can travel to the camera. As a consequence the curved sections of the device appear darker than the straight sections in all presented videos and post-processes data extracted from them, such as space-time diagrams of the wave propagation presented below. No image intensity correction was implemented at this time.

2.2.5.3 OH* Chemiluminescence (Round RDC)

We consider time-resolved, point-wise measurements of radiative emission of intermediate species of combustion to approximate the distribution of heat release across a detonation wave cycle within the RDC. Optical access is provided to the detonation channel by sapphire windows on the inner and outer bodies. The outer window has a 25.4 mm diameter, and the inner window has a 12.7 mm diameter. The windows are concentric and are located 60 mm downstream from the injectors, which correspond to about 60% of the total length of the detonation channel, which corresponds to where the detonation wave is believed to exist. Emissions from the detonation channel can be observed from both inside and outside the engine. The windows are shown to be co-linear; however, the inner body window can be rotated with respect to the outer body window to perform measurements with a phase shift in the detonation cycle.

The axial location of the measurement relative to the detonation channel and other instrumentation is shown in Figure 2.4, which is a schematic of the (unwrapped) outer wall with the position of various sensors. The measurement is taken at the center of the optical access window and is denoted with the blue dot at position F. To supplement the chemiluminescence measurements taken, high speed pressure measurements are taken via a water-cooled high-speed pressure transducer (Kulite EWCTV-13-312-500A) at the second location in position E. This location was chosen as it is the closest axial location to the optical access and sampling volume, and is indicated with a purple dot in Figure 2.4.

2.2.5.4 OH* Chemiluminescence (RT-RDC)

Chemiluminescence imaging relies on the collection of spontaneous emission from a chemically formed, electronically excited intermediate of combustion. Because the formation of the electronically excited intermediate occurs only during the combustion process (specifically, during the formation of the intermediate), detection of the spontaneous emission associated with the excited intermediate serves as a proxy of chemical reaction, or heat release. In our study, where we operate with pure hydrogen fuel, OH* is then a convenient marker of the heat release process and allows us to differentiate between the different spatial regions where chemical reactions occur and are

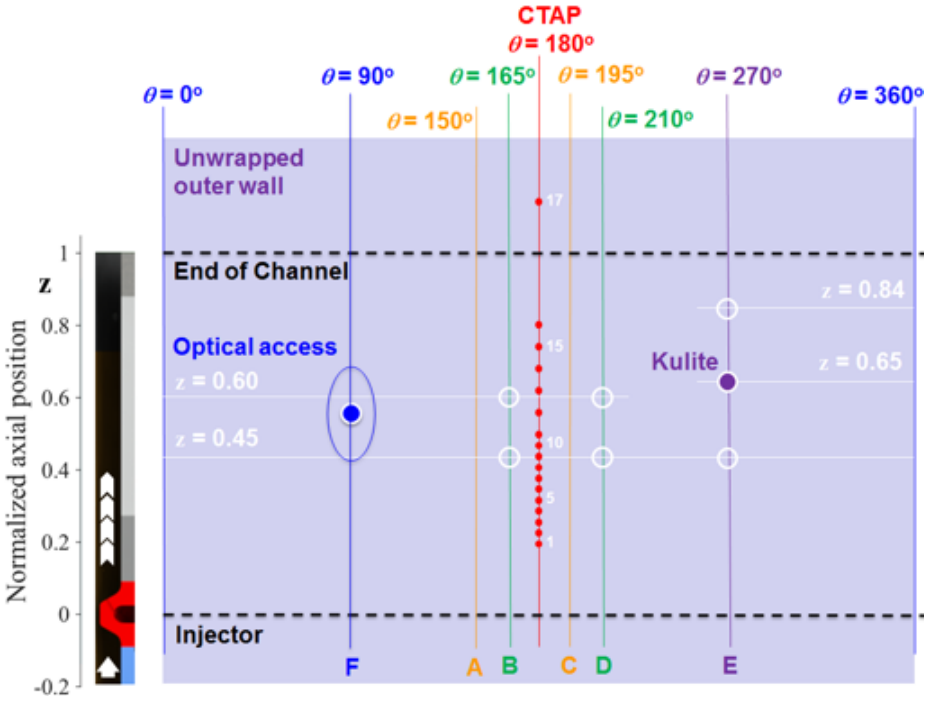

Figure 2.4: Schematic diagram of the arrangement of sensors on the outer wall of the RDC.

important for sustaining the detonation wave. The spontaneous emission from OH* occurs from the first electronically excited state to the ground state and correspond to UV emission. Hence, here we aim at emission from the $A^2\Sigma^+(v = 0) \rightarrow X^2\Pi(v = 0)$ transitions near 310 nm.

High speed OH* chemiluminescence was taken in the RT-RDC during steady operation of the device. The flow field was imaged at 80,000 fps with a 2 microsecond exposure with an intensified high speed camera (a combination of a LaVision HS-IRO intensifier coupled to a Photron high speed CMOS camera). The collected light was spectrally filtered through a 310 ± 10 nm bandpass filter positioned before the collection UV camera lens. The field of view taken comprised of 204 by 580 pixels over the 18 cm by 6.4 cm window. Visible in this view are portions of the air plenum, its constriction, fuel injectors, as well as most of the detonation channel. The two microsecond exposure also leads to a slight smearing of the detonation wave as it travels approximately 3 mm or about 10 pixels during the exposure time. Other flow features will have significantly less smear due to their much lower speeds.

2.2.5.5 Chemiluminesence Collection Optics (Round RDC)

Radiative emission from OH* for the round configuration is collected from the detonation channel with a suitable collection optics arrangement. All of the chosen optics directly interface with the inner and outer window body mounts. The light is first collimated by a collection lens, then it is passed through a second lens that focuses the light on a multimode optical fiber that delivers the collected light to a free-space detector array. This optical arrangement allows for a selective point measurement in space that can be controlled by the location of the lenses relative to the detonation channel. The optics arrangement are modeled using a custom ray tracing code to determine the sampling volume size and location within the channel as a function of collection optics characteristics and position. Based on the current configuration, the expected sampling volume is a prolate spheroid with a maximum cross-sectional diameter of 400 μm, which is limited by the chosen optical fiber. The optics were aligned such that the sampling volume is approximately 0.8 mm away from the inner body, which puts it at about 10% of the channel width away from the inner body.

The light leaving the fiber is first pitched through a 50:50 beamsplitter, refocused with a collection lens on the detector, filtered through optical filters of desired transmission properties, and finally collected by dedicated photomultiplier tubes (PMTs). The experiments presented here were performed with a 307 nm and 320 nm bandpass filters that both have a full-width at half-maximum (FWHM) of 10 nm. For the sake of conciseness, the results reported in this paper are solely from the 320 nm bandpass filter; results extracted from the 307 nm are similar to what obtained from the 320 nm filter. This optical arrangement is shown schematically in Figure 2.5. The output from the PMTs is amplified with transimpedance amplifiers and collected with a high-speed data acquisition system at a sampling rate of 1 MHz.

2.2.5.6 OH PLIF

The flow within the detonation channel of the RT-RDC was excited with a laser sheet introduced into the channel through a custom designed optic. The beam was formed from the output of a frequency-doubled Nd:YAG pumped dye laser that was frequency doubled to produce light with a wavelength of approximately 284 nm to target the $\mathrm{Q}_1(9)$ and $\mathrm{Q}_2(8)$ overlapping transitions of the $A^2\Sigma^+ \leftarrow X^2\Pi(v' = 1, v'' =$

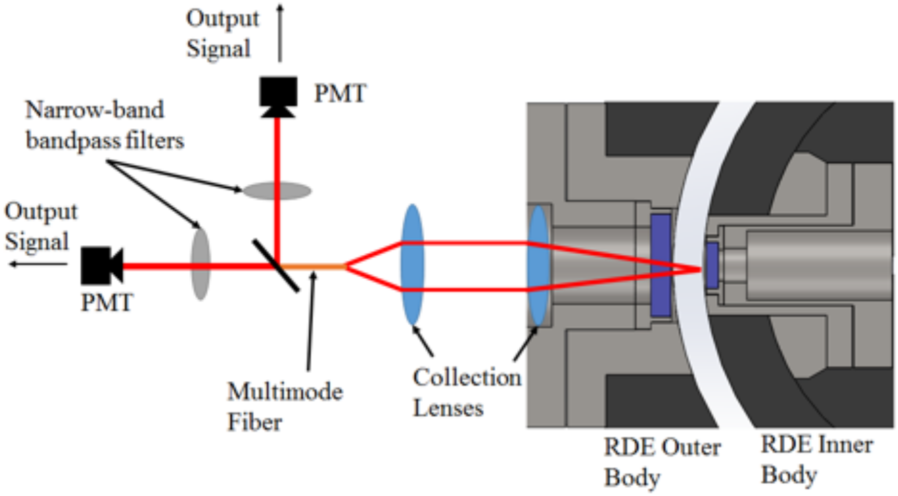

Figure 2.5: Schematic diagram of the optical arrangement for OH* emission measurements in the RDC.

0) electronic transition of OH. The laser beam wavelength was calibrated using a wavelength scanning procedure conducted on a bench top methane flame before use in the RT-RDC. The resulting images have been corrected for background light exposure, with work being ongoing for beam energy and sheet profile corrections.

The camera used was an intensified CCD camera (Andor DH334T-18F-E3) with a gate of 250 ns and equipped with an f/2.8 100 mm UV lens and a 310 ± 10 nm bandpass filter to suppress undesired light. Currently the lasers we utilize operate at 10 Hz. However, due to the camera's limitations we are limited to 5 Hz acquisition rates. Over a total run time of only a few seconds, this allow us to acquire 20 to 25 uncorrelated single shot OH PLIF images per run.

The camera and laser run independently of the RT-RDC. However, we are able to correlate snapshots taken with the camera to the cycle through the use of the information provided by the high-speed pressure transducers located in the detonation channel. Once fully processed and corrected, the images shown here cover a region in the detonation channel of 37 mm × 68.4 mm (277 × 512 pixels). Figure 2.3 schematically shows the location of the OH PLIF imaging region with respect to the RT-RDC (three-dimensional schematic on the right), as well as with respect to the imaging side windows and the fuel/air injection system (schematics on the left of the figure). In figure 2.3 an instantaneous snapshot of the OH* chemiluminescence showing the location of the detonation wave and other secondary combustion regions is shown for comparison.

2.3 Analysis Techniques

2.3.1 Evaluation of OH* Chemiluminesnce Diagnostic

The basis of the measurements taken in this work is that the heat release in the detonation cycle can be related, although perhaps only qualitatively, to the emission of chemiluminescence of electronically excited OH formed from chemical reactions. An initial evaluation of this assumption is presented here before the experimental results and conclusions drawn from them are presented and discussed. This assessment is based on performing detailed chemistry modeling of the formation of the electronically excited OH, and investigating its relation to distribution of heat release rate, the total heat release, and their dependencies on operating conditions through Zel'dovich - von Neumann - Döring (ZND) detonation structure modeling. Presented here is an initial assessment, and additional studies are required to fully address this aspect.

2.3.1.1 OH* Emission Modeling

To predict the radiative emission from electronically excited OH, or OH*, a model that combines the production and then spectral emission of OH* was constructed. To predict the production of OH* as a result of chemical reaction across a combustion front, a suitable OH* mechanism was used in conjunction with a ZND solver and a detailed chemical mechanism for H_2/air combustion. We use the mechanism of formation of OH* of Hall and Petersen [7], which they developed for H_2/CH_4 mixtures at high temperature and atmospheric pressure combustion (deflagration). We are currently evaluating other possible mechanisms. The mechanism includes a reaction for the formation of OH*

$$\mathrm{O} + \mathrm{H} + \mathrm{M} \rightleftharpoons \mathrm{OH}^* + \mathrm{M},$$

which is treated as a separate chemical species, as well as reactions to account for non-radiative quenching with different collisional partners of the type

$$\mathrm{OH}^* + \mathrm{M} \rightleftharpoons \mathrm{OH} + \mathrm{M},$$

and radiative emission representing the decay from the electronically excited state to the ground state (OH($A \rightarrow X$)):

$$\mathrm{OH}^* \rightleftharpoons \mathrm{OH} + h\nu$$

This model was then coupled to the H_2/air mechanism of Hong *et al.* [8] and used in ZND calculations using the Shock and Detonation toolbox for Cantera [9], which includes a one-dimensional ideal ZND detonation model. This model was then exercised for H_2/air mixtures for different equivalence ratios at an initial pressure of 1 atm and temperature of 300 K, which are the assumed nominal conditions ahead of the detonation wave in the experiments presented here. The solution of the ZND solver provides the distribution of species and properties (pressure, temperature and speed), including OH*, across the ideal ZND detonation wave.

Both the H_2 and OH* mechanisms used here were developed for ambient pressure conditions in constant pressure situations, which is not representative of the environment found across a detonation wave, such as what modeled by the ZND model. Since there is a lack of reported data for these reactions at elevated pressure, this mechanism was still used despite potentially being inaccurate due to effects associated with elevated pressures. Additionally, though the OH* mechanism they reported included the reactions involving carbon, we only included the reactions that would be present during H_2/air combustion. The mechanism was based on OH* emissions observed around 307 nm, which corresponds to $\mathrm{A}(v' = 0, 1) \rightarrow \mathrm{X}(v'' = 0, 1)$ transitions, and includes contributions from all rotational states in the $\mathrm{A}(v' = 0, 1)$ and $\mathrm{X}(v'' = 0, 1)$ manifolds. Therefore, we interpret the prediction of OH* as a prediction of the OH in the electronically excited A state across all possible rovibronic states.

To evaluate the expected emission spectrum, we have coupled the prediction of OH* from the chemical model to a spectral absorption and emission model for OH that was previously developed in our group [10]. The model assumes a thermalized population distribution function in the ground and first electronically excited states, and handles all rotational lines within multiple vibrational bands within a desired spectral range. In this approach, the OH* chemical model is used to compute the number density of OH in the (chemically-induced) electronically excited state across all rotational and vibrational states, whereas the population distribution in the various rovibronic states are assumed to follow an equilibrium Boltzmann distribution. Therefore, the radiative spectral emission ϵ_ν is than evaluated according to

$$\epsilon_\nu(\nu; p, T) \approx \sum_{i,j \in \Omega} n_{OH^*} f_{B,j}(T) A_{j \rightarrow i} \phi_{j \rightarrow i}(\nu; p, T) \tag{2.1}$$

where n_{OH^*} is the number density of OH*, evaluated from the chemical model of OH*; $f_{B,j}(T)$ is the Boltzmann population fraction of the electronically excited A state and includes contributions from all vibrational and rotational states; $A_{j\to i}$ is the Einstein A coefficient for a specific rovibronic transition $j \to i$; and $\phi_{j\to i}(\nu; p, T)$ is the spectral lineshape of the $j \to i$ transition, which depends on local pressure and temperature, and it is here assumed to follow a Voigt lineshape function. The Boltzmann population fraction depends on the local temperature only, and its use is consistent with the assumption of a thermalized system. The summation is extended over the set of transitions allowed within a spectral region of interest, Ω. The solution from the ZND model, including contribution of OH*, provides the spatial distribution of all species of interest, pressure and temperature, from which the expected emission spectrum from each point across the ZND detonation wave is computed.

Once emission spectra for each point across the detonation wave have been computed, the information on the optical filters that were used in conjunction with the PMT's can be applied to the resulting spectra to evaluate what would be observed by the PMT. While the spectral variation of the quantum efficiency of the PMT could also be included, the variation is nearly constant for the wavelength range of the bandpass filters used. Thus, spectral variations of the response of the PMT were neglected. To approximate the effects of finite resolution of the optical system, which is expected to smear out sharp features associated with the rapid variations of a detonation wave, the effect of probe volume size was modelled to be similar to a low-pass filtering operation with a filter kernel of size equal to the probe volume size. This final operation was applied to the spatial distribution of emission intensity across the computational domain.

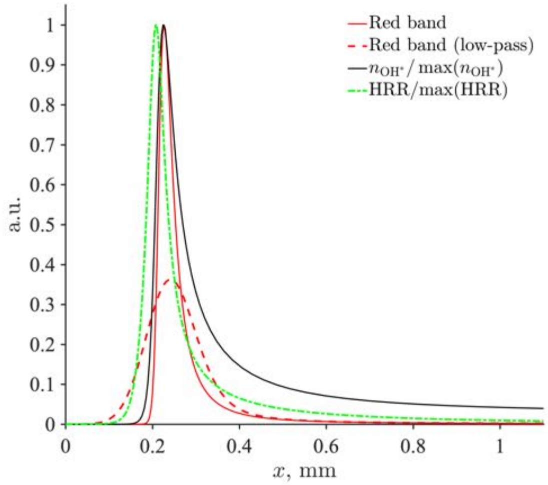

Figure 2.6: Example of radiative emission intensity and (normalized) number density of OH* across an ideal ZND detonation wave for H_2/air at $\phi = 1$. The solution shows a rapid rise followed by rapid decay across a detonation wave. The finite-size of the probe volume smears the rapid variation of OH* across wave.

An example of the results of the model is shown in Figure 2.6, where the distribution of computed OH* and radiative emission (corresponding to what would be observed across the 320 nm optical filter) are shown across an ideal ZND detonation wave for H_2/air at an equivalence ratio of $\phi = 1$. The spatial distribution of the radiative emission with and without the low-pass filtering associated with finite probe volume effects is shown. The solution shows the rapid variation in OH* and its associated radiative emission across the wave, and the decay past the initial front. This variation is somewhat attenuated by the effect of finite size of the probe volume. Figure 2.6 also includes the computed spatial distribution of the heat release rate (HRR), arbitrarily normalized by the peak value for convenience. Although there is not an exact correspondence between the spatial distribution of HRR and chemiluminescence (distribution of OH*), because of the delay between the onset of HRR and that of radiative emission, there is an overall qualitative correlation that gives some support to the underlying assumptions used in this study. Nevertheless, we continue to develop the model to more completely assess the validity of these assumptions for our purpose.

2.3.1.2 Limitations of the Diagnostic

The diagnostic approach used here has several limitations, some associated with its implementation (such as the effect of finite size of the probe volume or the presence of self-absorption), but some with the underlying assumptions used to derived the quantities of interest described below. First and foremost, the approach relies on the mostly unverified assumption that the OH* chemiluminescence remains linked to the local heat release rate, and thus can be used to infer the amount of energy released across portions of the cycle. Limitation of this assumption was anticipated in Figure 2.6 where the spatial distribution of heat release rate across a ZND detonation does not exactly correlated with the spatial distribution of estimated OH* chemiluminescence, not even in a qualitative sense. In fact, the HRR is seen to precede the onset of OH* chemiluminescence. Although a comprehensive study of this has not been concluded in this work yet, we anticipate that this effect will remain similar across different initial conditions and it will be a limitation that needs to be kept in mind as the results of this work are discussed. An example of a study that can be done is to establish the dependence of results of the type shown in Figure 2.6 on the models being implemented

Even more fundamental, a unique relationship between the total heat released and equivalence ratio cannot be established. For example, for a given fuel and initial conditions, the total amount of energy released across the combustion front would increase with equivalence ratio of the mixture up to stoichiometric conditions, and would remain constant afterwards since all of the oxidizer has already been consumed. This means no additional chemical energy can be released. Thus, this asymptotic value of the total heat release would no longer directly relate to the OH* chemiluminescence, which is seen to decrease in rich conditions. Figure 2.7 shows the relationship between the heat released, Q_T, (arbitrarily normalized by the maximum value for demonstration purposes) as a function of equivalence ratio, ϕ. The heat release in Figure 2.7 is defined as the integral under the spatial profile of various quantities, such as the synthetic OH* chemiluminescence predicted assuming the blue filter (the 307 nm bandpass filter), the red filter (the 320 nm bandpass filter), or broadband collection. Although the three measures do not exactly match, all three of them exhibit a non-monotonic dependence on equivalence ratio. This breaks down a direct dependence with equivalence ratio, as it is implicitly assumed here.

In general, it is observed that the integrated values from the OH* chemiluminescence decrease with equivalence ratio after stoichiometric because of dependencies of pressure and temperature on equivalence ratio, pressure effects on chemistry, variation in predicted OH* distribution, and inaccuracies associated in the models used here. On the contrary, for the lean and stoichiometric cases, the predicted integral of the OH* emission increases nearly linearly with equivalence ratio, following a relationship that would be expected for the total heat released with ϕ. Thus, at least for lean conditions, this might provide some initial validity to the approach. Clearly, the approach may not be able to fully capture the physics of rich conditions, though for completion of the operation map, these conditions will be also be presented here. It should be noted that despite we describe the operation of the RDC in terms of a global equivalence ratio, in real-

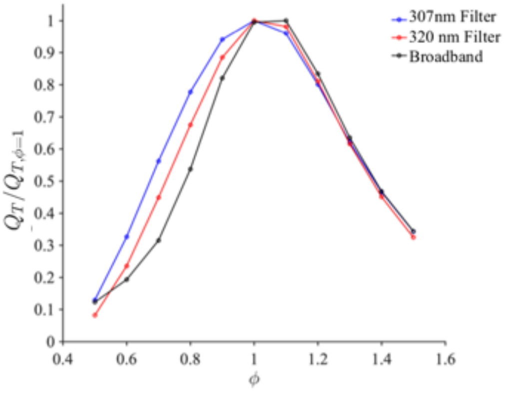

Figure 2.7: Expected variation of heat release as inferred from OH* chemiluminescence with equivalence ratio.

ity this may not be representative of its exact operation since fuel/air stratification effects might exist and might alter the properties of the detonation wave, as well as the interpretation we can make of the OH* emission in light of the qualitative results of Figure 2.7. In fact, for example under global conditions near stoichiometric, stratification associated with the mixing process could lead to local distributions that straddle $\phi = 1$, making equivalence ratio dependencies of the type shown in Figure 2.7 unavoidable.

2.3.2 Phase Averaging Procedure

To more readily study the distribution of chemical reactions occurring in the detonation channel, it is advantageous to construct a phase-average profile of the OH* emission across the detonation cycle. While there will be variations within the individual cycles, having a representative cycle allows for the analysis of the presence of secondary combustion.

In order to produce the most representative phase-average profile of the OH* emission, the phase averaging is conducted over the portion of the total run when the operation of the RDC is stable. The portion of stable operation is here defined as the portion of the total run time where the detonation speed, direction, and characteristics of the secondary waves remain constant. This is determined by examining the waterfall spectra constructed from the high-speed measurement of pressure and OH* emission. After determining the stable portion of the run, individual detonation cycles are identified through a line detection algorithm of lines marking the propagation of the detonation wave in space-time (wave) diagrams generated from the high-speed chemiluminescence videos taken aft of the RDC. By defining the detonation cycle in this manner, a cycle-averaged wave speed can be computed for each detonation cycle as well as a cycle time between each detonation cycle. Using this information, individual cycles in the stable portion can be parsed through and by accounting for cycle-to-cycle variation of the cycle time, individual cycles can be aligned on a cycle phase-average profile with respect to their periods. For each phase, the individual cycles are then re-sampled before being added to the value of that phase. After all the phases have been parsed through, the resulting values are appropriately normalized without losing or affecting amplitude information, so that different cases can directly be compared.

2.4 Round RDC Operation

2.4.1 AAI Injector

2.4.1.1 Combustion Mode

The AAI injector is seen to operate in mode 1, 4, or 5. Mode 1 is stable rotation of a single detonation wave and is denoted by a strong tone at roughly 80% of the ideal CJ frequency. See Figure 2.8a for a waterfall spectra created using Kulite sensor at location E1 for AMF = 115 kg/m^{2}s and ER = 1.0 which is typical for this mode. This corresponds to wave speeds of 1380-1650 m/s which increase with ER. Higher frequency harmonics of this tone are also present, as well as a tone at roughly the ideal CJ frequency and its harmonics. The correspondence to wave speed is confirmed using high speed video. A single, clear detonation wave can be seen in Figure 2.11a, which is a single frame captured using the high speed camera at AMF = 85 kg/m^{2}s and ER = 1.0. The detonation wave is propagating clockwise as apparent by the luminous head. The chemiluminescence light intensity at a point within the detonation channel was analyzed to construct a frequency power spectrum and a strong peak was observed at 80% of the CJ frequency. Weak tones are also seen at 50% and 25% of the CJ frequency which are believed to be related to coupling and interaction with the plenums. The main fuel valve opens at 5.5 s and the transition to detonation can be seen in the first 0.4 s. During transition the signal is noisier and the tone at 80% of the CJ frequency is not as clearly defined. Mode 4 is unsteady deflagration and many azimuthally propagating disturbances and standing wave modes are observed but no clearly distinguishable detonation wave is seen for the majority of a given run. See Figure 2.8b which corresponds to AMF = 50 kg/m^{2}s at ER = 1.2. Unsteady deflagration is indicated by tones near 50% the CJ frequency and a series of other weaker tones between 50-80%. The signal also has greater low frequency noise content when operating in this mode.

At ERs of 0.6 and 0.8 a single detonation wave is seen for all AMFs considered. For ERs of 1.0-1.2 and AMF of 55 kg/m^{2}s or less, unsteady deflagration persists. At greater AMFs a single detonation wave is seen once again. Between these regions, at AMF around 50-60 kg/m^{2}s, mode 5 behavior is seen. Mode 5 is characterized by unpredictable, rapid transition between unsteady deflagration and steady single wave detonation. This behavior is exemplified for AMF = 55 kg/m^{2}s atER = 1.0, where the unsteady deflagration exists for roughly half a second before transition into detonation occurs. See Figure 2.9. Additionally, within this transition region

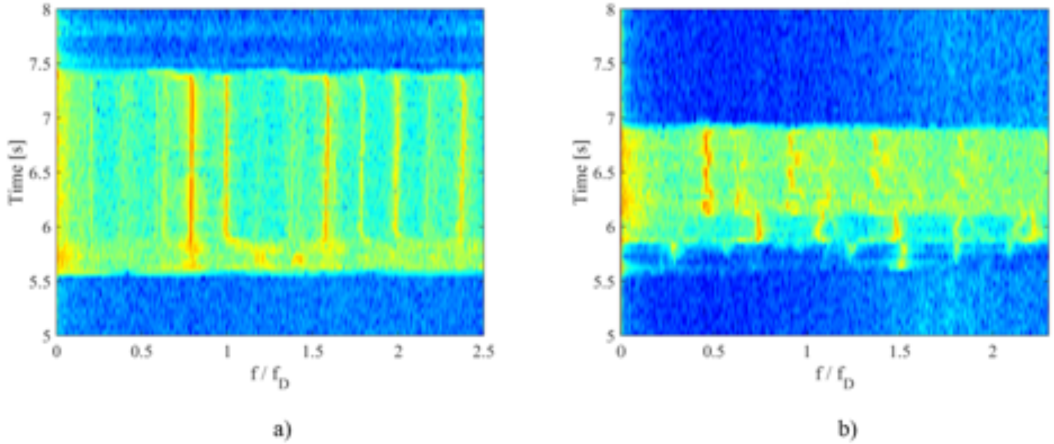

Figure 2.8: a) Waterfall spectra for AAI injector at $\mathbf{AMF = 115\ kg/m^2s}$ and $\mathbf{ER = 1.0}$. This spectra is typical of mode 1, single detonation wave operation. b) Waterfall spectra for $\mathbf{AMF = 50\ kg/m^2s}$ and $\mathbf{ER = 1.2}$ corresponding to mode 4 unsteady deflagration.

there is variation from run to run, with progression from deflagration to detonation not guaranteed.

Additional insight into the ignition and transition to detonation may be gained by plotting the CTAP data for single runs as contour plots, as shown in Figure 2.10 for ER = 1.0. Figure 2.10a corresponds to spectra in Figure 2.9, and Figure 2.10b corresponds to Figure 2.8a. In the contour plots time progresses left to right and the axial location of the sensors is on the vertical axis. At CTAP1, the pressure is 95% of the air plenum pressure. In many of the cases on the waterfall spectra there appears to be a 'dead zone' after ignition, where little signal is observed. During this period the flame is anchored downstream of the detonation channel, near the afterburner. This can be seen clearly in Figure 2.10a. The bright red region at t ≈ 5.75 s is the ignition event. The pressure upstream of the air throat increases when the flame flashes back into the channel and enters an unstable deflagration mode. At t = 6.5 s a transition to detonation occurs and this is marked by a further decrease in the upstream CTAP pressures. This decrease in pressure during detonation versus unsteady deflagration is seen in many cases. Compare this to Figure 2.10. In this case the flame flashed back

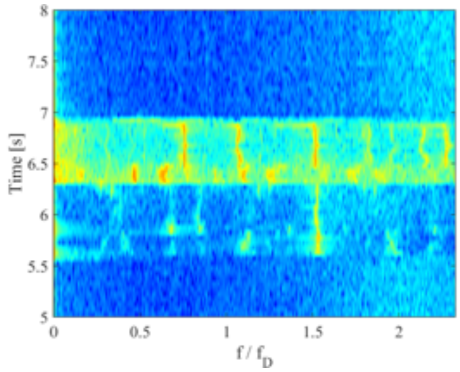

Figure 2.9: Waterfall spectra for AAI injector at AMF=55 kg/m^{2}s and ER=1.0 showing transition from downstream flame anchoring, to unsteady deflagration in the channel, to stable detonation.

into the channel immediately after ignition and transitioned directly into detonation. In general, anchoring at the afterburner appears to be a strong function of mass flow rate, with longer periods of time spent anchored downstream at lower mass flow rates.

2.4.1.2 Static Pressures

Examination of the pressure within the plenums as a function of AMF rate reveal substantial difference between the cold flow (before combustion) and hot flow (during combustion) cases, as shown in Figure 2.12 for ER = 1.2. The air plenum pressure trends show a similar profile but with increased pressure in the hot flow cases. The cold flow pressures increases monotonically with air mass flow rate, while the hot flow case has a downward step discontinuity in the transition region: the plenum pressure under detonating conditions is lower than for operation in deflagration mode. The decrease in plenum pressures seen during transition is larger for ER = 1.2 than it is for ER = 1.0.

The momentum flux of the air and fuel jets at their respective throats may be estimated in a time averaged sense for each case. First the mach number of the flow at the throat is computed numerically using Newton's Method and a Mach number/area relation. The Mach number/area relation and its first derivative with respect to the

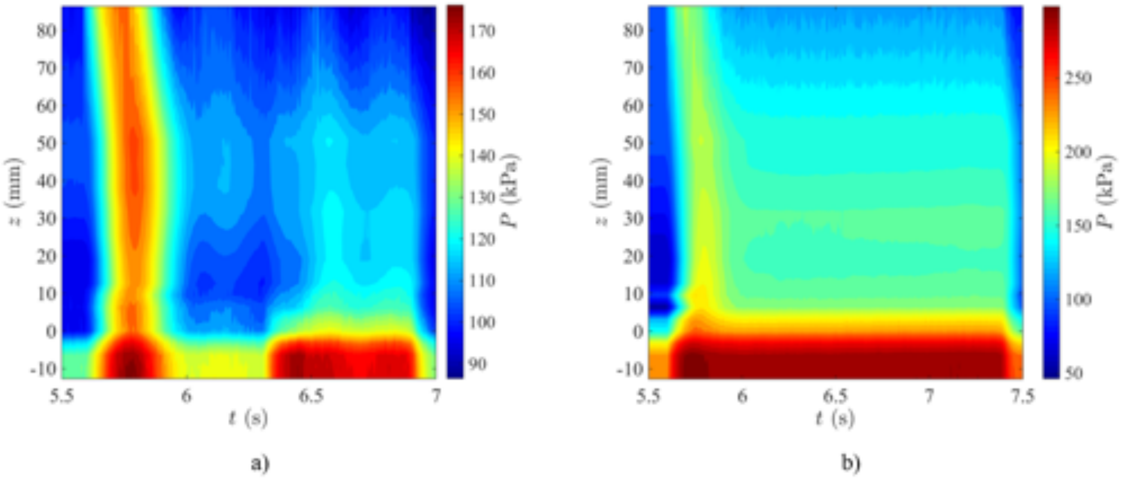

a) b)

Figure 2.10: a) Pintle injector CTAP Contour plot for air mass flux of 55 kg/m^2s and equivalence ratio of 1.0 showing the flame stabilized downstream near the afterburner before flashing back into the channel. b) Pintle injector CTAP contour plot for air mass flux of 115 kg/m^2s and equivalence ratio of 1.0. In this case the flame flashes back and transitions to detonation immediately.

mach number are shown in Equations 2.2-2.4.

$$f_M = \frac{1}{M}\left[\frac{1+\frac{1}{2}(\gamma-1)M^2}{\frac{1}{2}(\gamma+1)}\right]^{\Gamma} - \frac{A_t}{A^*} \tag{2.2}$$

$$f'_M = 2\Gamma\frac{(\gamma-1)}{(\gamma+1)}\left[\frac{1+\frac{1}{2}(\gamma-1)M^2}{\frac{1}{2}(\gamma+1)}\right]^{\Gamma-1} - \frac{1}{M^2}\left[\frac{1+\frac{1}{2}(\gamma-1)M^2}{\frac{1}{2}(\gamma+1)}\right]^{\Gamma} \tag{2.3}$$

$$\Gamma = \frac{(\gamma+1)(\gamma-1)}{2} \tag{2.4}$$

The critical area A^* is computed using the known mass flow rate and plenum pressure according to Equation 2.5, where n is the number of injection elements and the plenum pressure is taken as the stagnation pressure p_0. This is a reasonable assumption since the cross sectional area of the plenums is large compared to the throats so the flow speeds in the plenum are low relative to the throat. A_t is the throat area for the injector of interest. The discharge coefficient C_d is taken to be 1.

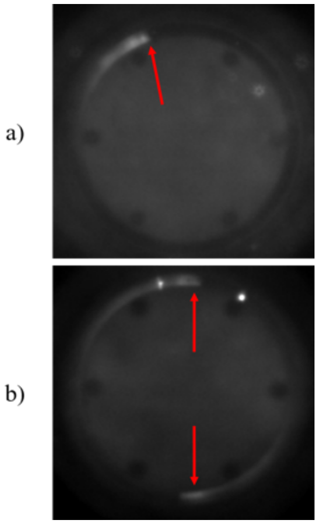

Figure 2.11: a) Single frame from high speed video showing the presence of a single, stably rotating detonation wave at **AMF = 85 kg/m^{2}s ER = 1.0** obtained using the AAI injector. b) Two stably co-rotating detonation waves at **AMF = 85 kg/m^{2}s** and **ER = 1.0** obtained using the JIC injector.

$$A^* = \frac{\dot{m}_{exp}}{nC_d p_0}\sqrt{\frac{RT_0}{\gamma}\left(\frac{\gamma+1}{2}\right)^{\frac{\gamma+1}{\gamma-1}}} \tag{2.5}$$

Then Newton's method is applied as shown in Equation 2.6 to iteratively solve the equation until the residual is less than a specified value. Subscript j is the iteration variable. A tolerance of $1e^{-05}$ was used.

$$M_{j+1} = M_j - \frac{f_M(M_j)}{f'_M(M_j)} \tag{2.6}$$

The pressure and temperature at the throat may then be computed using standard isentropic relations, as shown in Equations 2.7-2.9.

$$p = p_0\left[1 + \frac{(\gamma-1)M^2}{2}\right]^{\frac{(\gamma-1)}{\gamma}} \tag{2.7}$$

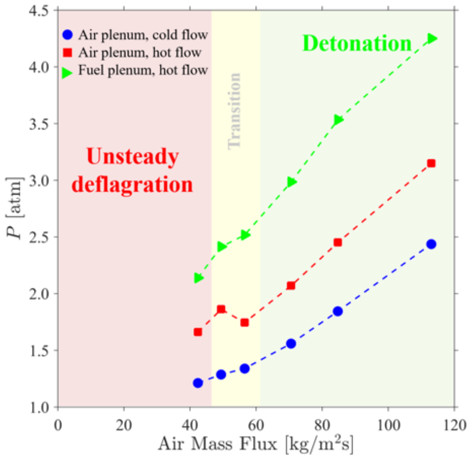

Figure 2.12: Transition of combustion mode seen with the AAI injector at **ER = 1.2**. Plenum absolute pressure traces plotted against air mass flow rate with the combustion modes denoted.

$$\rho = \rho_0 \left[1 + \frac{(\gamma - 1)M^2}{2} \right]^{(\gamma - 1)} \tag{2.8}$$

$$T = T_0 \left[1 + \frac{(\gamma - 1)M^2}{2} \right]^{-1} \tag{2.9}$$

The momentum flux for each stream may be computed according to Equation 2.10.

$$q = \rho u^2 = \gamma p M^2 \tag{2.10}$$

We then define the momentum flux ratio as shown in Equation 2.11, using values computed at the respective throats. In addition, the pressure ratio between the plenums and the mixing region is computed and compared to the critical pressure ratio. This comparison is a rather crude approximation of choking but provides another metric for evaluating choking along with the Mach number.

$$J = \frac{q_{Fuel}}{q_{Air}} \tag{2.11}$$

This is computed for each case and may be plotted against AMF, as shown in Figure 2.13a for the AAI injector. The AAI injector detonates most easily at ER $= 0.6$ and this corresponds to a momentum flux ratio around $J = 0.6$. In the transition region for ER $= 1.0 - 1.2$ and AMF $\approx 50 - 60$ kg/m^{2}s we can see that the momentum flux ratio takes on higher values of $1.2 - 1.8$. Additionally, when J approaches 0.6, the fuel and air plenum pressures become similar to another, indicating that the injectors may be responding similarly.

The output from this model is useful but the simplicity of the derivation should be remembered. The model treats the flow as quasi-one dimensional and ignores all viscous and dissipative effects. Flow field components such as flow separation may have a strong effect on the performance of a given injector and in the interpretation of computed results. For example, in the case of the air stream it is possible to compute the throat Mach number during cold and hot flow. Comparing across these two cases we can see that the temporally averaged Mach number is lower during combustion than prior to ignition despite a constant mass flow rate during the entire experiment. See Figure 2.13b.

Additional, there are three scenarios involving flow restriction which may persist, as represented in figure 2.14. First, it is possible that the RDC annulus is unobstructed by any effect. Second, it is possible that the annulus is affected by a physical blockage such as a constriction or separation region. And lastly in the case of the detonation wave, the annulus may be effectively obstructed by the pressure rise associated with the detonation wave. As discussed earlier, directly adjacent to the detonation wave there may be a region where the flow may be stopped or reversed. If one views the wave as a simple reduction in air injection area then we should expect an increase in the throat temporally averaged Mach number as would be the case for a physical obstruction. In the case of a physical obstruction which reduces the injector area while maintaining the same mass flow rate, the Mach number will always increase until the choking point is achieved. Yet our calculations show a decrease rather than an increase. The reason this is possible is because the wave also creates a rise in the stagnation pressure measured in the flow, which we would expect to cause a decrease in the throat Mach number. This pressure rise is more substantial an effect than the reduction in injection area, causing a lower temporally averaged Mach number seen in experiments. It is important to note that in the case of a physical obstruction the stagnation pressure also increases as the injector area is reduced, however this rise is not sufficient to overcome other competing effects.

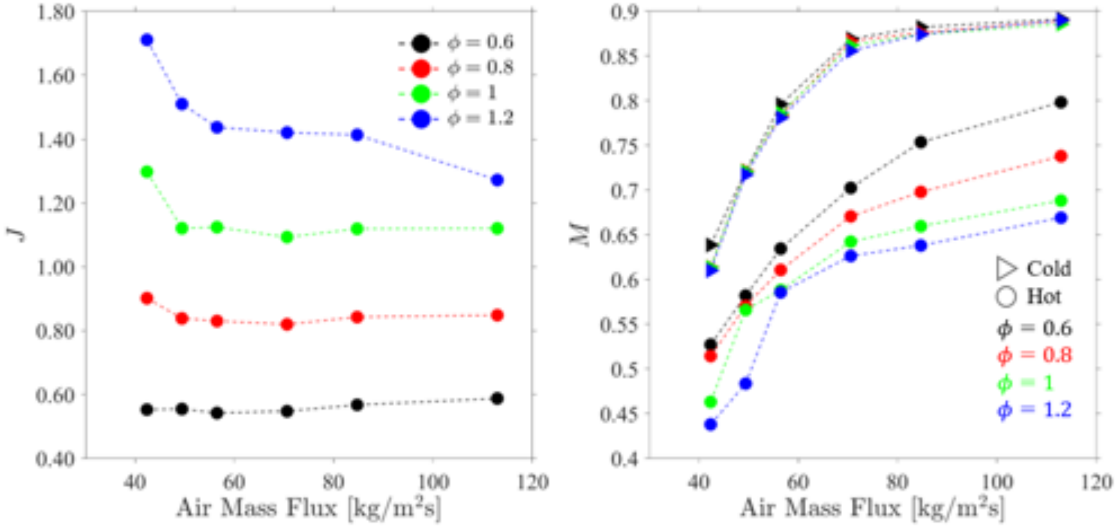

a)

b)

Figure 2.13: a) Pintle injector estimated momentum flux ratio. b) Pintle injector air mach number computed using the simplified model for hot and cold flow cases.

2.4.2 Statistical Analysis of Static Pressure Measurements

From high speed pressure measurement a very large amount of information is collected for every experimental run. In order to condense this information, statistical analysis of wave properties inferred from the pressure time traces is carried out. Specifically, a series of metrics defining the characteristic of the temporal evolution of measured pressure is conducted as described next. How these metrics are defined and computed from the pressure time traces is shown in figure 2.15.

For each run a period of steady operation is determined by analysis of the waterfall spectrum. Typically, we consider a duration of 0.75 seconds. During this steady period the data is segmented into N windows. This segmentation is shown in figure 2.15 by the black lines. Here we typically take $N = Tf_W$ where T is the steady period duration and f_W is the measured frequency of the rotation of the detonation wave. Thus, each window is approximately the length of one period of rotation of the detonation. For each period, the time of passage of the detonation wave at the measurement point, as well as the peak and minimum pressure is recorded.

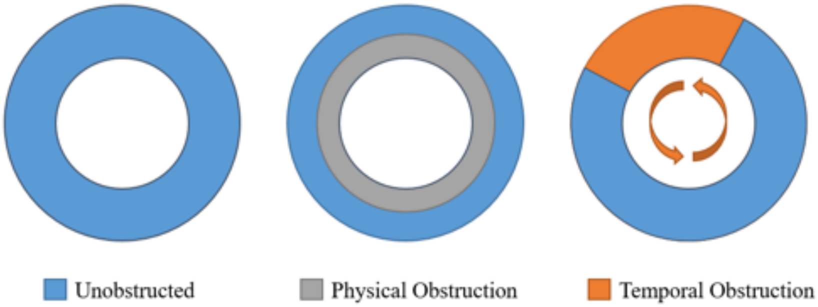

Figure 2.14: An exaggerated annulus for an RDC is shown in three possible states of operation. On the left is a channel which is entirely unobstructed by any fluid effect or by any physical obstruction. In the middle is the case of some physical obstruction such as a constriction or a large separation region. On the right is the case of a temporal obstruction where flow issues over the unobstructed portion of the annulus but is stopped in the orange region by some fluid effect, for instance the detonation wave.

From these two measurements, we are able to calculate five different metrics of the detonation wave properties. These metrics and how they are extracted from the pressure traces is shown in figure 2.15. Firstly, the pressure as the detonation wave passes the sensor is termed the peak pressure, shown as green dots. Secondly, the low pressure value across all windows can be used to calculate a lower bound pressure for the entire period, shown as blue lines. For each window, the time of arrival of the detonation wave is used to interpolate between low pressure values in order to calculate what we termed the base pressure. This base pressure needs to coincide temporally with the peak pressure in order to calculate a (peak-to-base) pressure ratio. The difference between a peak pressure and its base pressure is termed the amplitude pressure, shown as an orange line. The mean pressure is simply a temporal average across the entire steady period, shown in purple. Lastly, a pressure ratio is calculated by dividing the peak pressure by its base pressure. From each run there are approximately 2500 cycles that are used to calculate both a mean value over all cycles, as well as the corresponding standard deviation.

In the figures that follow, points represent average values computed over the steady period, while the error bars indicate one standard deviation from the mean value. All

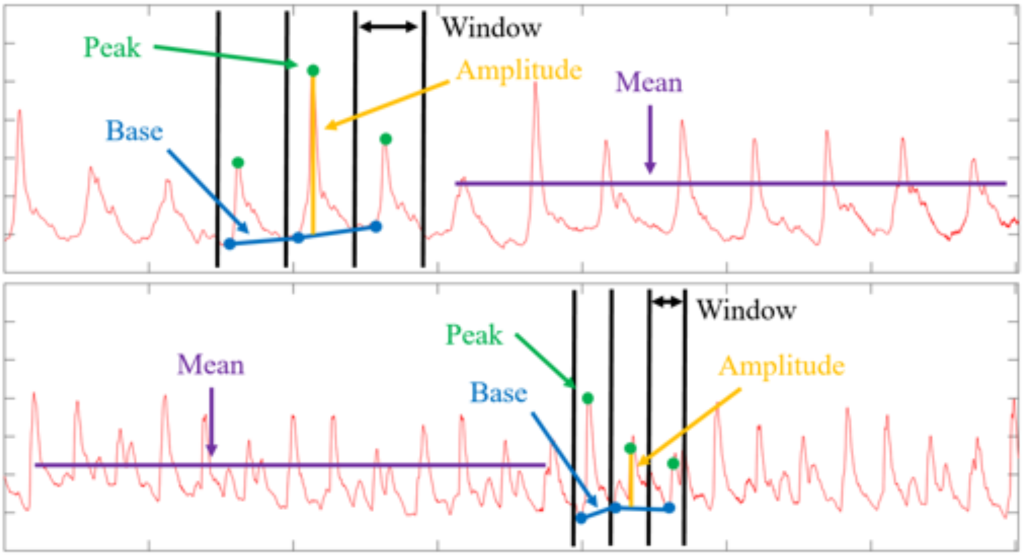

Figure 2.15: Typical pressure traces taken from two separate experiments at the same sensor location E1. The top pressure trace is for a run operating in the deflagration mode. The bottom trace is for a run operating in the detonation mode. Peak pressures are shown as green dots. Base pressures shown as blue dots with blue lines shown for information interpolated between points. The amplitude pressure shown in orange is the difference between a peak pressure and the blue line base pressure. The pressure ratio is likewise taken for an instance in time. The mean is a simple temporal mean over the entire period.

metrics have been normalized by the air plenum pressure of each experimental run. Cases that exhibit the deflagration mode are denoted by squares, while the detonation cases are all denoted by circles. Results from measurements taken at location E1 and E3 are presented, and are used to assess differences between the properties of the flow at these two locations. Referring back to figure 2.4, E1 is the upstream sensor and E3 is the downstream one. The range of conditions and their mode of operation of the device is shown in figure **??**. The majority of runs operated in detonation mode (green in figure **??**). However, for those cases were both main modes were present (yellow in figure **??**), information was extracted solely from the detonation mode portion of the run. Only three cases showed only the deflagration mode. These cases are at air mass flux of 43 kg/s/m^2 at equivalence ratios of 1.0 and 1.2 as well as air mass flux of 50 kg/s/m^2 at equivalence ratio of 1.2.

2.4.2.1 Peak Pressures

For peak pressure measurements the standard deviation is much smaller for detonation cases than deflagration cases as seen in figure 2.16. In addition peak pressures are substantially greater for the deflagration cases than the detonation cases for the upstream sensor located at E1 as seen in figure 2.16(a). These large pressure peaks caused by the system are suppressed at the downstream location E3 however, and are approximately the same as detonation cases whose peak pressures were smaller at E1. At sensor position E3, the pressure peaks are approximately 1.5 to 2 for almost all cases regardless of which operational mode it resides in. For both sensor locations, there is a tendency for higher equivalence ratio runs to have higher peak pressures for a given mass flux. In addition, with increasing mass flux pressure peaks measured at E1 always tend to decrease, whereas at location E3 there is a local maximum in peak pressure for the air mass flux of 57 kg m^{-2}s^{-1}. It is likely that with increasing mass flux the resting axial position of the detonation wave begins to move further and further downstream. As the wave moves further downstream pressures measured at E1 would tend to decrease with increasing mass flux, as observed in measurements. By noting the local maximum in E3 measurements we can infer that the detonation wave's peak intensity lies between E1 and E3 at low mass fluxes. As the mass flux increases the wave sits further downstream, coming closer to position E3 and increasing the measured pressure. Further increasing the mass flux pushes the wave further downstream and decreases the pressure measured by both sensors. This trend of decreasing pressure at E1 and a local maximum at E3 will also be found in a number of other measures to be discussed in further sections and is most clearly seen in figure 2.18.

2.4.2.2 Amplitude Pressures

Similar to peak pressure measurements, the deflagration cases have substantially higher amplitudes at the E1 position as seen in figure 2.17(a). These large variations are not present at the E3 position. Amplitude pressure exhibits no trend in equivalence ratio for either sensor location. This implies that the amplitude pressure is independent of wave properties, such as Mach number and heat release. There is however a slight decrease in amplitude pressure with increasing mass flux for both

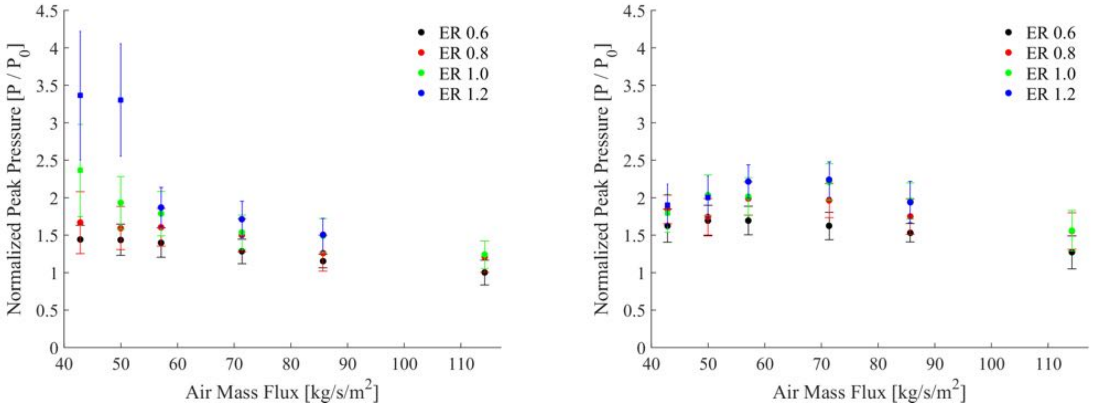

(a) (b)

Figure 2.16: Average peak pressures normalized by plenum pressure, error bars shown are one standard deviation. a) Sensor measurements taken at position E1. b) Sensor measurements taken at position E3.

sensor locations. For both sensors values begin at approximately 1 for the lowest mass flux case and reduce to approximately 0.6 for the highest mass flux cases.

2.4.2.3 Mean Pressures

Similar to peak pressures and amplitude pressures, the mean pressure of deflagration cases is substantially higher at position E1 than detonation cases, but rapidly decreases at position E3 where they are approximately the same as detonation cases. In contrast detonation cases all experience a slight pressure increase from position E1 to E3. As with peak pressure measurements, higher equivalence ratio measurements tend to have higher pressures. In addition for high equivalence ratio cases the temporal mean pressure of the flow is higher than the air plenum pressure at position E3 as seen in figure 2.18(b). While we would ideally see an increase in stagnation pressure, as pressure gain is properly described as an increase in stagnation pressure, out measured increase in static pressure is still a positive indicator of a favorable thermodynamic process. In addition the trends seen in peak pressure are also seen in the mean pressures, there is a decrease in mean pressure measured with increasing mass flux for position E1, and a local maximum seen at position E1 at approximately 57 kg/s/m^2.

2.4.2.4 Base Pressures

The base pressure is the average minimum pressure measured during a cycle. This measure has many of the same trends seen in mean pressure. This is to be expected from the relatively small variation in amplitude pressure seen in figure 2.17. This small variation means that for all runs the mean and base pressures are approximately proportional. For deflagration cases there is a decrease going from sensor location E1 to E3. For detonation cases however there is an increase from E1 to E3. Like mean and peak pressure measurements there is a decrease in base pressure for sensor location E1 with increasing mass flux and a local maximum present at E3 as seen in figure 2.19. Lastly higher base pressures are measured for high equivalence ratio cases.

2.4.2.5 Pressure Ratios

The pressure ratio defined as the peak pressure caused by the passing detonation wave divided by the base pressure over which it passes is the pressure measurement that is most easily compared to ideal detonation wave computations. This is because one of the key parameters that defines a detonation is the static pressure ratio across the wave. Here we consider the Pressure Ratio we have defined to be equivalent to

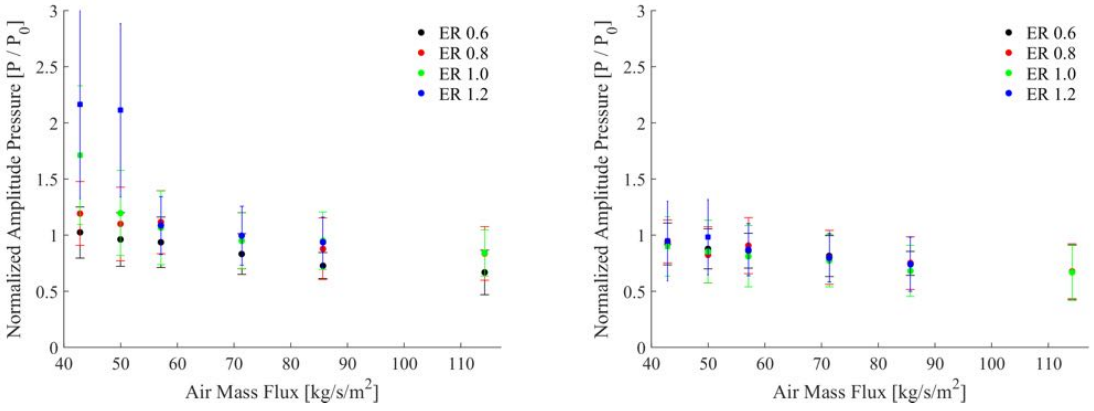

(a) (b)

Figure 2.17: Average amplitude pressures normalized by plenum pressure, error bars shown are one standard deviation. a) Sensor measurements taken at position E1. b) Sensor measurements taken at position E3.

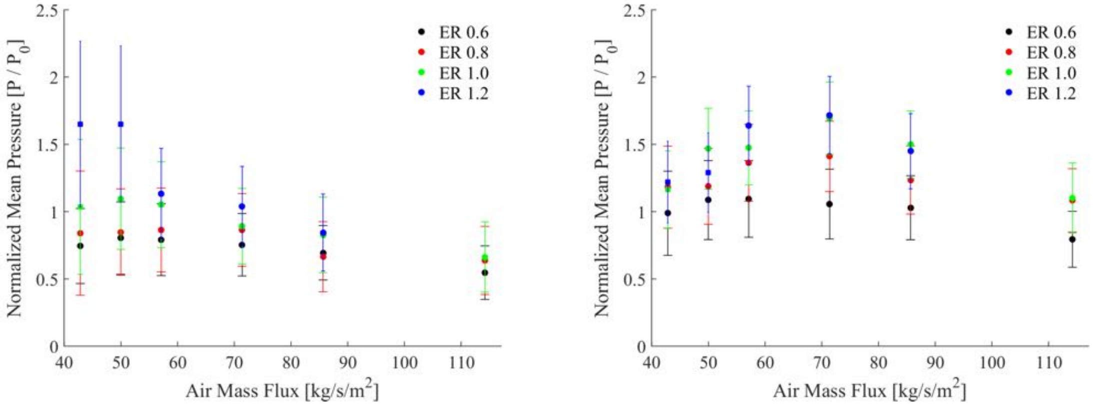

(a) (b)

Figure 2.18: Mean pressures normalized by plenum pressure, error bars shown are one standard deviation. a) Sensor measurements taken at position E1. b) Sensor measurements taken at position E3.

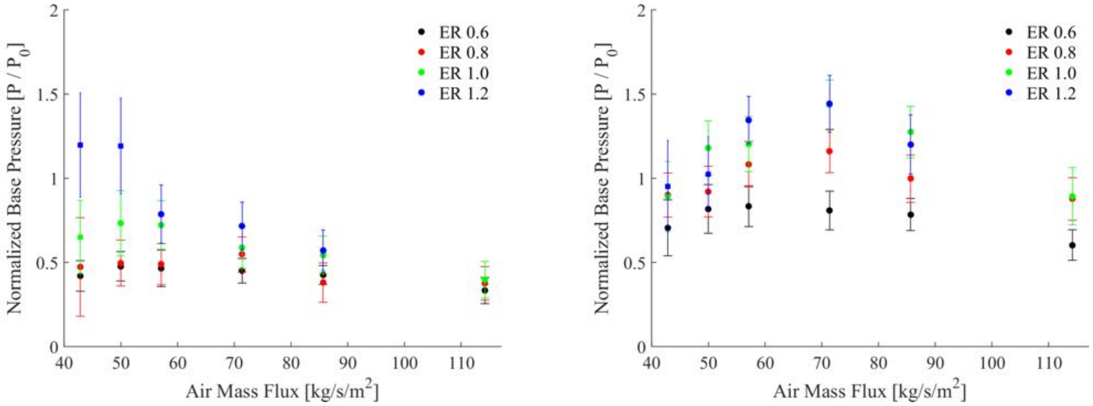

(a) (b)

Figure 2.19: Average base pressures normalized by plenum pressure, error bars shown are one standard deviation. a) Sensor measurements taken at position E1. b) Sensor measurements taken at position E3.

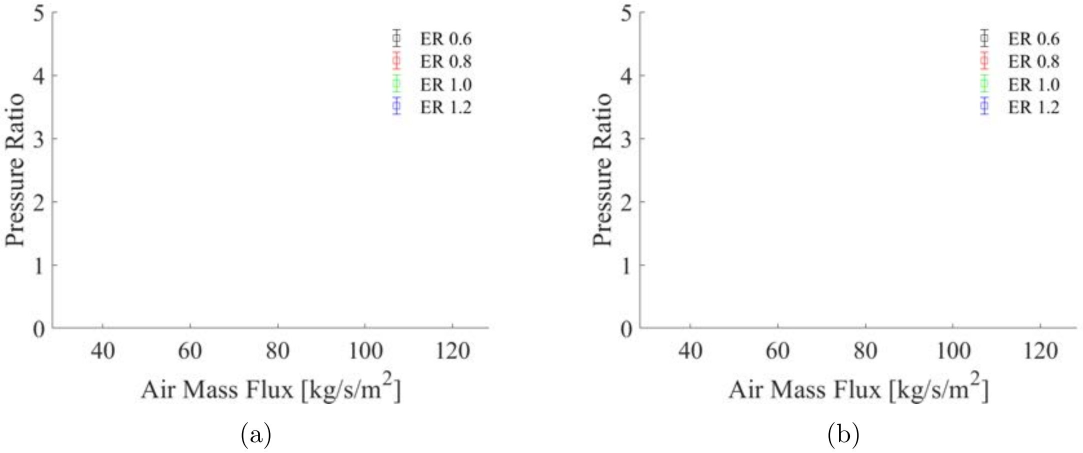

(a) (b)

Figure 2.20: Pressure ratio taken as peak pressure divided by the base pressure, error bars shown are one standard deviation. a) Sensor measurements taken at position E1. b) Sensor measurements taken at position E3.

the static pressure ratio from ideal one dimensional detonation wave calculations. For ideal detonation waves the static pressure ratio is on the order of 15 to 25 depending on fuels and equivalence ratios [11]. However in the MRDC measured pressure ratios are approximately 2 to 3 with a very wide variability in pressure ratio for sensor location E1. In contrast Sensor location E3 shows smaller variability with most runs having ratios of approximately 2 regardless of mass flux and equivalence ratio as seen in figure 2.20(b). The measured pressure ratios are substantially smaller than what would be expected of an ideal detonation. Although it has to be kept in mind that the dynamic pressure transducers might not be able to properly respond to the fast transients imposed by the passage of a detonation wave, this result could be an indicator that the waves present in the RDC might not be classical detonation waves. Ideal detonation waves in an RDC is not to be expected, frictional losses, fuel stratification and other real effect are expected to change the wave behavior. However, it is surprising that while the wave still travels at approximately 80% the ideal speed, the strength of the wave is greatly diminished. How the thermodynamics of these unideal waves compare to the ideal thermodynamic cycle of a detonation will have large implications for the future of RDC technology.

2.4.3 JIC Injector

2.4.3.1 Combustion Mode

The JIC injector operates in either mode 1, 2, or 4. Mode 1 corresponds to a single stably rotating detonation wave and a typical spectrogram created using the Kulite sensor at location E1 is shown in Figure 2.21a for AMF = 55 kg/m^{2}s at ER = 1.0. As with the AAI this mode is identified by a strong tone at 80% of the CJ frequency with weaker tones at its harmonics and corresponds to wave speeds of 1380-1650 m/s. The AAI spectra for this mode was rich with tones at and below 50% of the CJ frequency, but these tones are absent for the JIC injector. It was theorized that for the AAI injector these tones were a result of interaction with the feed plenums, and their absence from the JIC plots may be understood with the area ratio shown in Table 2.1. The JIC air injector is choked to a greater degree with a larger pressure ratio between the air plenum and the detonation channel, and as a results the average air mach number is greater than 0.8 for all cases. Thus there is limited coupling between the detonation channel and the air plenum. Additionally the tone around the CJ frequency is absent or very weak. It is unclear what this tone physically corresponds to and further investigations are under way to identify the sources of all tones seen in the spectra. The JIC injector operates in mode 2 with 2 co-rotating detonation waves at AMF $= 85 - 115$ kg/m^{2}s and ER $= 1.0 - 1.2$, with a typical waterfall spectra shown in 2.21b. The co-rotating waves can be seen in the high speed video, as shown in Figure 2.11b. As one would expect, the presence of two detonation waves results in a strong tone at double the frequency seen for a single wave. The transition to two waves is often preceded by counter rotating detonation waves which bounce back and forth in a 'ping-pong' like mode before stabilizing into two co-rotating waves. There is noisy content at 80% of the CJ frequency and the low frequency bands are absent for this case as well.

Mode 4 operation is seen for ER = 0.6 at all air mass fluxes except AMF = 40 kg/m^{2}s which detonates unstably. See Figure 2.22 for a spectrogram for AMF = 55 kg/m^{2}s at ER = 0.6. These spectra are characterized by horizontal striations and low frequency noisy content. The striations correspond to the RDC periodically dying out, then relighting in a ring and attempting to flash back into the channel. There is a tone seen at roughly 20% of the CJ frequency, which is around 750 Hz. It is possible that this is LPD behavior, but it differs somewhat from the criteria established by other researchers, who noted frequencies around 1-1.6kHz[12, 13]. Forward traveling detonation waves have been seen traveling around 70% of the ideal CJ frequency with a reflected shock propagating backwards at roughly 30% of the CJ frequency[14]. Further, onset of LPD was seen only when the pressure ratio across the air injector was between 1.4 and 1.85[14], while this pressure ratio varies from 2-5 for the cases considered here. Further analysis needs to be conducted to understand this behavior. Chaotic azimuthal modes are seen during these runs, some with frequencies near 80% of the CJ frequency, indicating an attempt to transition to rotating detonation.

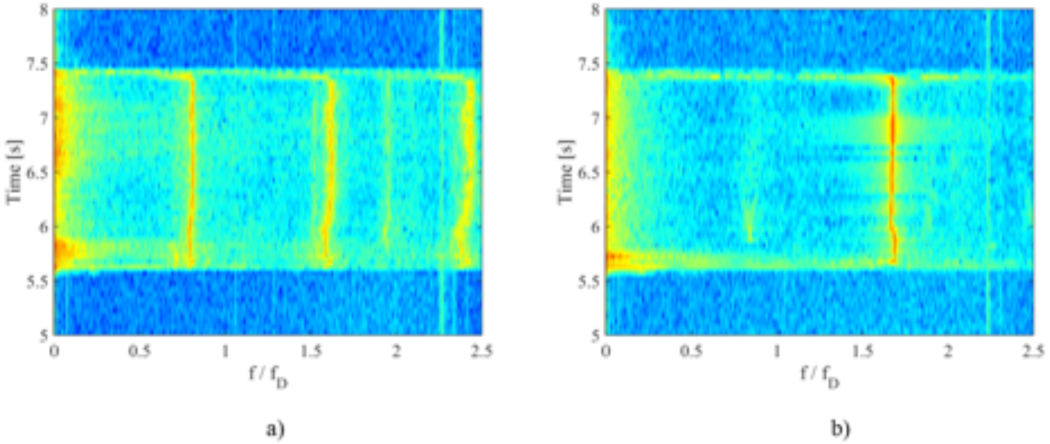

Figure 2.21: a) Waterfall spectra for JIC injector at **AMF = 55 kg/m^{2}s** and **ER = 1.0**. This corresponds to mode 1 operation with 1 detonation wave. b) Waterfall spectr for the JIC injector at **AMF = 115 kg/m^{2}s** and **ER = 1.2**. This corresponds to mode 2 operation with 2 co-rotating detonation waves.

2.4.3.2 Static Pressures

To aid in characterizing our test facility our CTAP measurements are compared against those taken at AFRL for the same air gap of 0.89 mm[1]. We find that our data agrees relatively well for AMF = 40 kg/m^{2}s, see Figure 2.23 which shows comparisons for ER = 1.0. The coordinate z is as defined earlier, with z=0 corresponding to the air throat of the AAI injector. A dashed line at the fuel injector surface is included. The datasets lie near each other though the trends seen are not exactly the same. Both show an initial drop as you progress downstream, but AFRL's data shows more undulation and a greater upward trend as you progress downstream

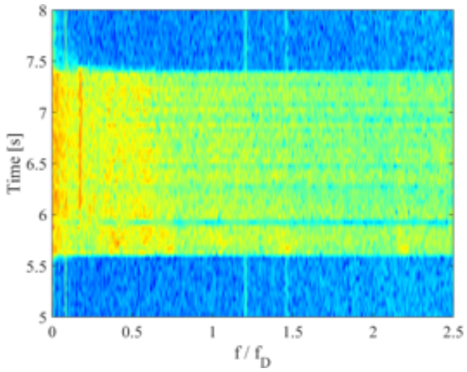

Figure 2.22: Waterfall spectra for JIC injector at $\mathbf{AMF = 55\ kg/m^2s}$ and $\mathbf{ER = 0.6}$. This corresponds to mode 4 operation of unsteady deflagration.

past the midpoint. The agreement is lesser as the MFR is increased. AFRL's dataset for AMF = 90 kg/m^{2}s lies between our datasets for AMF = 85 − 115 kg/m^{2}ss except for one point. These trends hold for the other equivalence ratios they report, though the ERs used are different than ours.

The momentum flux ratio of the air and fuel stream were computed as described previously and shown in Figure 2.24. As with the AAI injector, J decreases with decreasing ER, which makes qualitative sense. The JIC injector detonates most readily at ER = 1.2, which has J around 0.5. The AFRL was not able to detonate at ER = 0.6 except for the lowest mass flow rate case. As mentioned earlier, the air injector appears to be choked for a large portion of the detonation cycle and there is little variation in J with mass flux for ER = 0.8 − 1.0. As the momentum flux ratio approaches 0.5, the fuel and air plenum pressures approach one another.

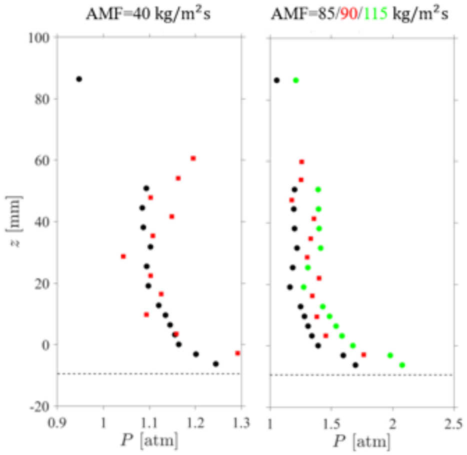

Figure 2.23: Comparison of our data set with that collected at AFRL[1] for **ER** = **1**. AFRL's data is shown in red and ours in black and green.

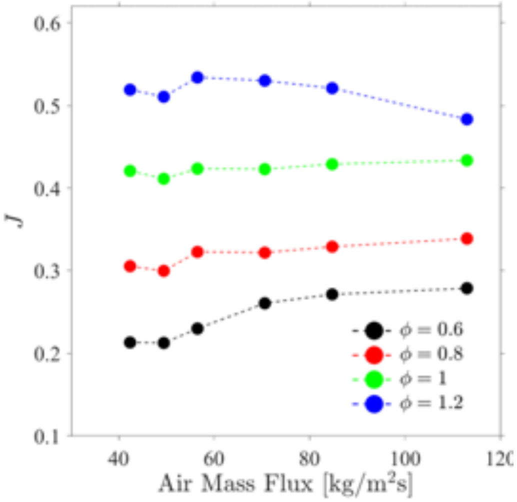

Figure 2.24: JIC injector estimated momentum flux ratio.

2.4.4 SIJ Injector

2.4.4.1 Combustion Mode

The SIJ injector operates in either mode 1, 3, or 4. As with the other cases operation in mode 1 with a single detonation wave corresponds to a single strong tone at 80% of the ideal CJ frequency. Figure 2.25a shows a typical spectrogram for this mode. As with the JIC injector, the bands below 50% of the CJ frequency are absent. This again makes sense as the area ratio for this injector listed in Table 2.1 is the smallest of those tested. Unlike the AAI injector, detonation is associated with the disappearance of a tone around the ideal CJ frequency. Progression from ignition to detonation is preceded by a period of noisy deflagration, with tones appearing at half the CJ frequency during this period. Mode 1 is only achieved for AMF=85-105 kg/m^{2}s at ER=0.8-1.2. This injector was the only one tested to operate in mode 3, which is steady deflagration with a counter-rotating wave structure. A waterfall spectra for this mode is shown in Figure 2.25b. This tones for this mode are evenly spaced, with the lowest strong tone lying near the expected detonation frequency. There is a lot of low frequency noise which appears to be greater burning further downstream. The high speed video of these cases shows what looks like a weak single detonation wave counter-rotating with an azimuthal disturbance which has peaks on opposing sides of the detonation channel. Mode 3 is seen for AMF=40-50 kg/m^{2}s. The rest of the cases fall into mode 4, unsteady deflagration, with a spectrogram shown in Figure 2.26. Tones are seen near 50% and at the CJ frequency and their harmonics. There are also other tighter groupings of weaker tones, which are inconsistent in their location between cases. For come cases the high speed video shows the counter rotating structure with an overall pulsation overlain. This pulsation seems to coincide with the strong tone at 50% of the CJ frequency.

2.4.4.2 Static Pressures

The momentum flux ratio was computed for the SIJ injector and ranged from 0.28-0.12, which is much less than for the other injectors. Additionally the fuel and air plenum pressures are much more disparate. The air injector is hard choked for all cases, with the pressure ratio ranging from 5-12. This is in contrast to the fuel injector which only chokes for the higher MFR and ER cases. Figure 2.27b shows a combustion mode map, where the choking state is estimated as described earlier. The symbols and background colors indicate the combustion mode while the symbol fill indicates

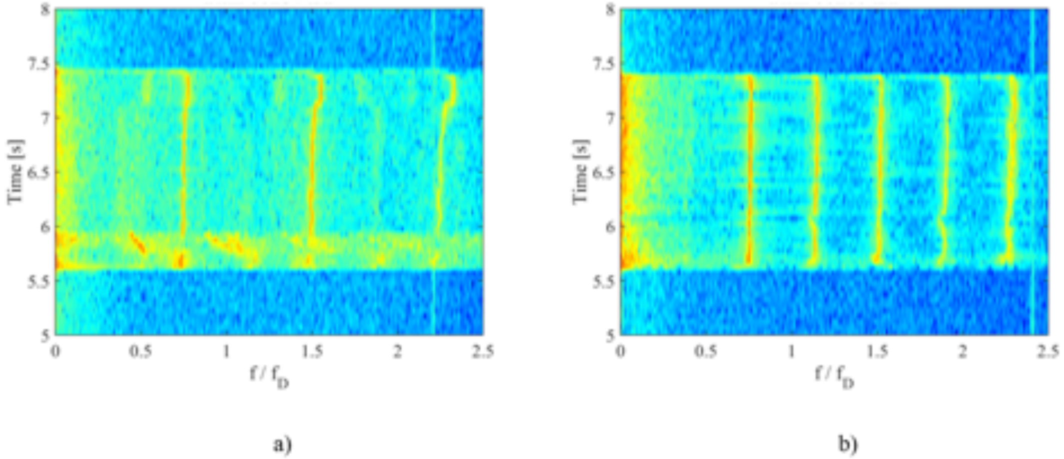

Figure 2.25: Waterfall spectra for SIJ injector at a) AMF=105 kg/m^{2}s, ER=1.2 and b) AMF=50 kg/m^{2}s, ER=0.8.

the state of the fuel injector, with a black symbol indicating choking. From this we can see that choking of the fuel injector is a necessary but not sufficient condition to achieve stable detonation. This is supported by Figure 2.27a, which plots the fuel and air mach numbers. The detonation region is circled in green. The air injector is choked in an average sense for all cases as the Mach number is approximately 0.94. As the fuel Mach number approaches 1 stable detonation may be achieved. When the fuel injector is not choked there is likely a severe mismatch between the injector responses. After the detonation wave passes it is unlikely that the air injector ever fully shuts down while the fuel injector does. This would result in an axially stratified mixture which may explain the pulsation seen in a few runs and may contribute to the formation of the counter rotating structure seen for this injector. It is unclear if the counter rotating elements lie on the same axial plane. Further investigation into the formation and structure of the complex modes seen is required.

2.5 RT-RDC Operation

The RT-RDC exhibits a variety of operation modes depending on the values of the air mass flux and equivalence ratio. Initial runs have established the existence of

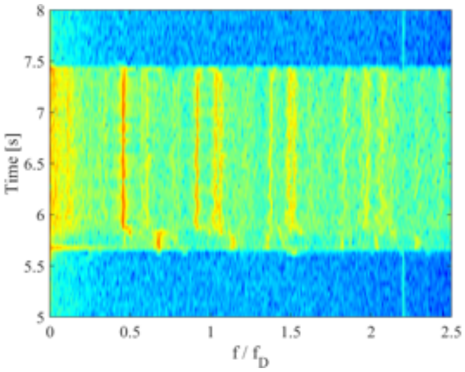

Figure 2.26: Waterfall spectra for SIJ injector at AMF=55 kg/m^{2}s, ER=0.6.

four modes that we have named as follows: (1) two-wave detonation; (2) three-wave detonation; (3) slapping; and (4) chaotic modes. Here we will describe each of the modes we observe based upon high speed chemiluminescence imaging measurements as well as high speed pressure measurements in the detonation channel. The high speed chemiluminescence video was processed into a space-time diagram (here simply referred to as x-t diagram) for a portion of the steady flow by, for each frame of the video, discretizing the arc-length of the detonation channel into 200 sectors and unwrapping them into a linear representation of the distribution of the intensity of the combustion fronts. In practice, this reduces each image in the video to a column vector of light intensity. Combining all of the frames throughout the video creates the x-t diagram showing the propagation of the waves (i.e., the trajectory) through the device. For clarity the transition points between straight and curved sections are shown as red dashed lines. The high speed pressure measurements will be used to construct waterfall spectra showing the change in spectral content with time. All frequencies shown will be normalized by the ideal detonation frequency $f_D = \frac{U_{CJ}}{P}$, which is defined to be the frequency an ideal detonation speed moving at the CJ speed would create if it traveled the distance of the mid channel perimeter of the device. In all cases we consider only steady state operation beyond all transient portions of a given run. The device currently exhibits four modes from initial testing, an operational map over our initial test points is shown in figure 2.28. The target operation mode (i.e., stable detonating mode with multiple waves) is currently observed for high equivalence ratio cases at a variety of air mass fluxes.

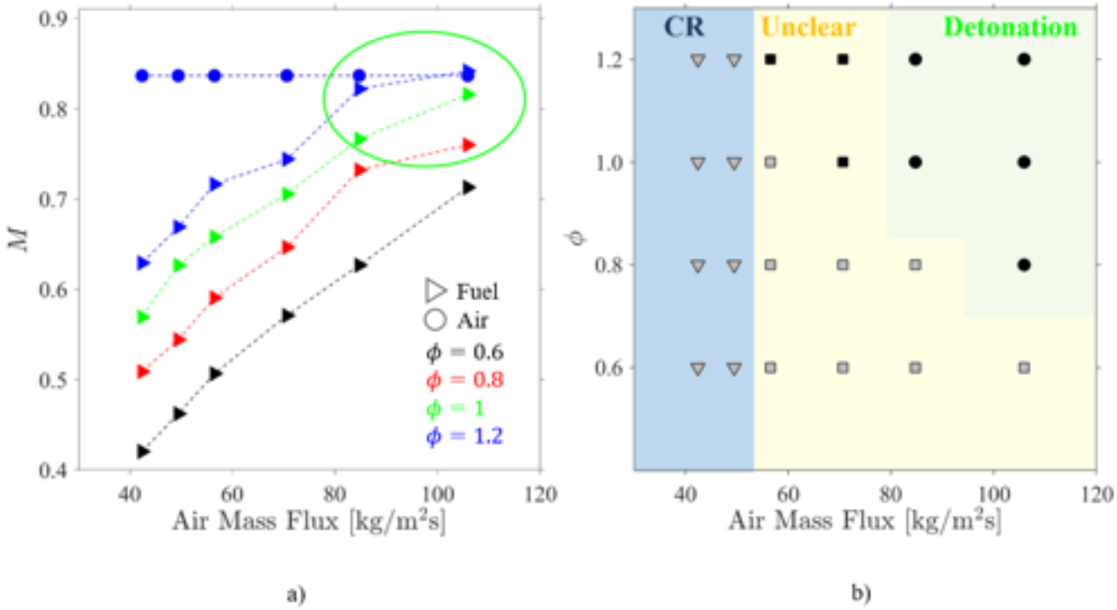

Figure 2.27: Plots showing the operating range of the SIJ injector. a) Fuel and Air Mach Mach numbers, circled green region indicates detonating cases. b)SIJ injector combustion mode map. The symbols and colors correspond to the combustion mode, where 'CR' denotes the counter rotating structure. A symbol filled black indicates choking of the fuel injector, while gray is unchoked.

2.5.1 2 Wave Detonation (MRDC Analogue)

The 2 wave operation point for the RT-RDC is the target operation mode for which the device was designed to investigate. When the device is operating at the proper conditions we observe two co-rotating discrete waves traveling through the channel 180 degrees out of phase from one another. A number of frames from high speed video is shown in figure 2.29 over the period of 1 full cycle. Each wave travels at a mean speed of approximately 1450 m/s or 75% of the Chapman-Jouguet (CJ) speed. While the waves do propagate for dozens of cycles without incidence there is a tendency for the direction of rotation to spontaneously reverse. This reversal process is seen more frequently in the RT-RDC than was observed in the MRDC. This transition process is often initiated or enforced when either wave travels from the straight section into

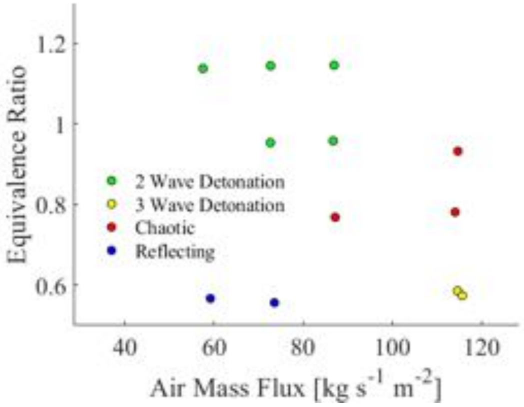

Figure 2.28: Operational map for the RT-RDC as a function of air mass flux and equivalence ratio.

the curved section or vice versa. The transition process induces a reflected wave that travels counter to the incident detonation wave. In some instances, the reflection can grow to become a new detonation wave that ultimately reverses the overall rotation direction. Stable wave propagation duration varies from run to run and operating point, but typically lasts for upwards of dozens of cycles, with transitions between directions typically about three to four cycles before stable co-propagating waves are re-established. While the device does exhibit some directional instability, the operation mode seen throughout the run is stable, with two waves present in the channel for the vast majority of the run.

Additional information can be inferred from waterfall spectra. An example spectra for the two wave detonation mode is shown in figure 2.30. Here we can see that at the beginning of the fueling sequence the RT-RDC begins in a different mode with a much sharper spectral shape, whereas the final operation mode toward the end has more distributed spectral content. As we will discuss later this sharp spectral region is associated with the slapping mode. The broader spectral content during two wave operation is a consequence of the directional instability.

2.5.2 Three Wave Detonation

The other detonation mode seen during operation is similar to the target operation mode for which the device was designed, wherein there are discrete co-rotating waves

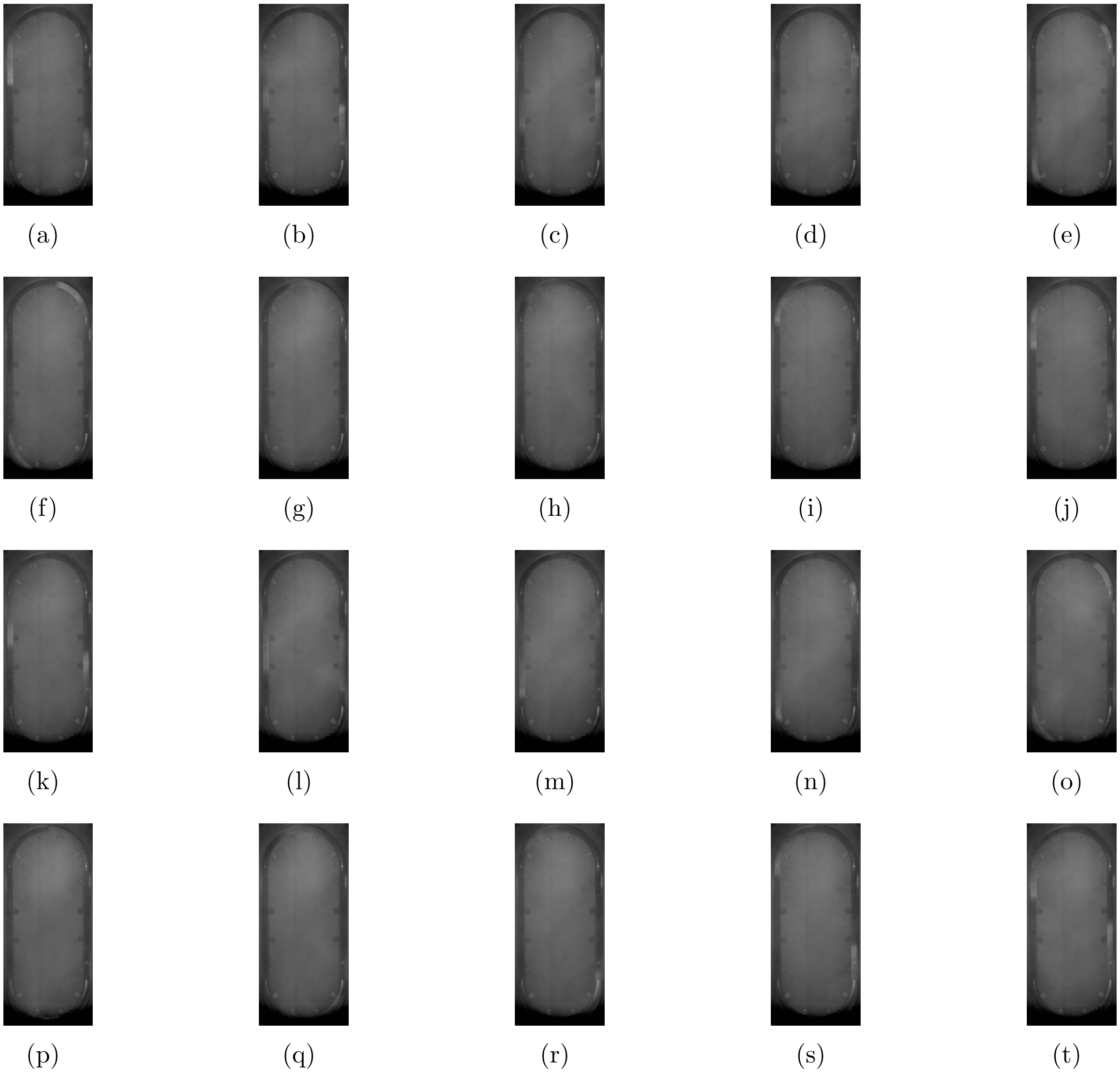
(a) (b) (c) (d) (e)

(f) (g) (h) (i) (j)

(k) (l) (m) (n) (o)

(p) (q) (r) (s) (t)

Figure 2.29: High speed chemiluminescence taken at 30,008 frames per second of the detonation channel looking axially into the device for one full cycle. Frames shown are from target operation mode of two co-rotating waves. Results shown for air mass flux of 57.6 $\text{kgs}^{-1}\text{m}^{-2}$ at an equivalence ratio of 1.14.

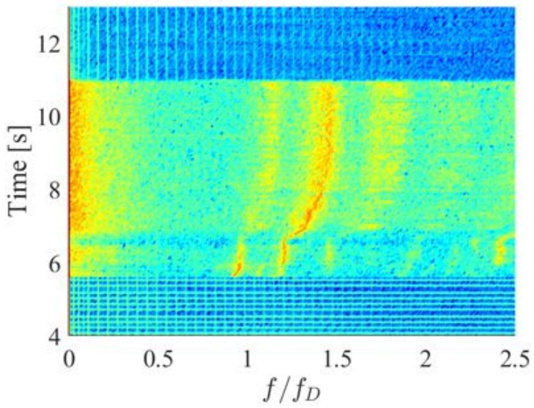

Figure 2.30: Waterfall spectra constructed from high speed pressure measurements. Spectra shown is for the 2 wave detonation mode. Results shown for air mass flux of 57.6 $\mathrm{kgs^{-1}m^{-2}}$ at an equivalence ratio of 1.14.

travelling stably through the detonation channel. This mode is characterized by three co-rotating waves, travelling at a mean speed which is approximately 73% of the CJ speed. While the waves are traveling through the device, there appears to be an acceleration as a wave transitions into the curved section and deceleration as it transitions out. The three waves all go through the same process of acceleration and deceleration as they travel throughout the device. This cycle of acceleration and deceleration lead to a cyclic pattern for the position of the three waves. This pattern is stylized in figure 2.31. A typical cycle begins with the three waves, colored red, green, and yellow in the positions as shown on the left hand side of the arrow in figure 2.31. The red wave is just about to enter the straight section on the left, the green wave is about to enter the bottom curved section, and the yellow wave is at approximately the mid point of the right hand straight section. As time progresses the red wave decelerates, the green wave accelerates, and the yellow wave moves at approximately the same speed as when the cycle started. Over the course of the next 120 microseconds, the waves have moved to the configuration shown on the right hand side of the arrow, which looks like a mirrored version of how the cycle started. Now the red wave will continue its propagation, the green wave will decelerate and the yellow will begin to accelerate. Over the next 120 seconds the waves will propagate until they have returned to a shifted version of the starting position, with the cycle repeating over and over. This process was gleaned from inspection of the high speed

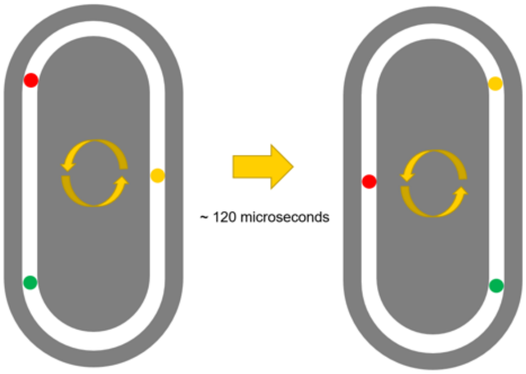

Figure 2.31: Stylized version of the detonation mode's acceleration and deceleration cycle. Each colored dot represents one of the waves.

video, and a more detailed analysis is necessary to verify and quantify this initial qualitative observation.

As shown in figure 2.32 the device also begins in a slapping mode before transitioning to its end operating condition. Once the detonation mode has been established it persists until the end of the run. The peak tone during this region of operation is approximately $2.2f_D$. When considering that there are three waves present during operation this means each wave has a frequency of $0.73f_D$. This speed and frequency are comparable to what was seen in the MRDC investigated previously. The distributed spectral content shown here is caused by a relative instability. While the three wave system persists for many dozens of cycles at a time, it does intermittently break down into something more reminiscent of the chaotic mode to be discussed later. Similar to the two wave system, the time between breakdown and stable propagation corresponds to approximately three to four cycles.

2.5.3 Slapping Mode

The slapping mode is a mode that occurs at operation points that are both low air mass flux and relatively low equivalence ratio, in this case lower than 0.8. This mode is characterized by what appears to be four waves persisting in the channel. Of these four waves two co-rotate clockwise on opposite points in the circumference while the other two co-rotate counter clockwise, also on opposite points of the circumference. This wave system and the interaction between the two sets of waves seems to be

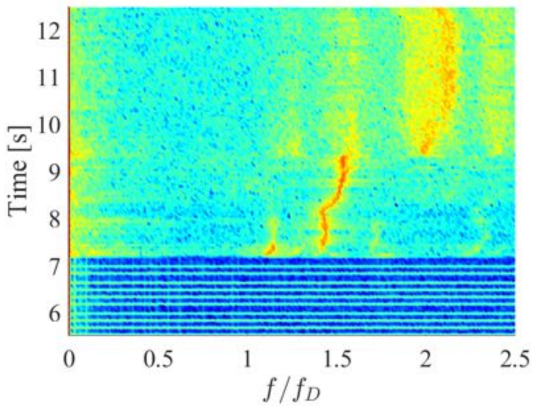

Figure 2.32: Waterfall spectra constructed from high speed pressure measurements. Spectra shown is for the detonation mode. Results shown for air mass flux of 114.6 kgs^{-1}m^{-2} at an equivalence ratio of 0.57.

stabilized by the entering and exiting of the wave from the curved and straight sections. As the wave transitions from one section to the other, there will necessarily be a series of waves that emanate from the transition point. In general both a compression and expansion wave will emanate. Because the traveling waves transition in opposite directions at the same location and time, the emanating waves from the simultaneous transitions will be of opposite character. The corners of the device may therefore be a natural settling point for the wave system. With the emanating waves acting as a restorative force that will gradually drive the interaction back to the intersection point. This behavior is most easily seen through an x-t diagram as shown in figure 2.33, where dashed red lines denote the transition points between straight and curved sections. The portion shown is representative of the entire run sequence and video, throughout the test waves can be seen to interact and intersect repeatably at the transition points between different sections of the device. The cross hatching pattern seen in the x-t diagram for this operating condition is indicative of counter propagating waves.

The waterfall spectra for this mode is well defined and spectrally sharp with most of the spectral energy contained very close to the primary tone and its associated harmonics, an example is shown in figure 2.34. For this mode there is a primary tone at $1.5 f_D$, which corresponds to the propagation of the wave systems. Because there are two waves co-rotating in a given direction, this means that a single wave would have

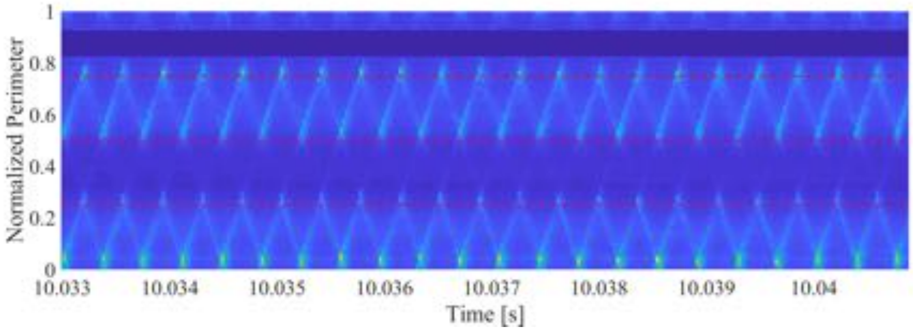

Figure 2.33: A portion of the x-t diagram constructed from high speed video. The red dashed lines denote the transition points between straight and curved sections. The perimeter regions from 0 to 0.25 and 0.5 to 0.75 are the two straight sections. Results shown for air mass flux of 59.2 kgs^{-1}m^{-2} at an equivalence ratio of 0.57.

a propagation frequency of about $0.75f_D$. The second set of waves provides spectral power at the same frequency and therefor causes no distortion to the spectral shape of the operation mode. This mode is seen in the beginning of most runs as it persists at the low flow rates and equivalence ratios where the device is ignited.

2.5.4 Chaotic Mode

The chaotic mode is a mode that defies a readily understood system like the detonation and slapping modes. In this mode there are still discrete waves that can be discerned, but the matter in which they interact and how the system evolves is difficult to understand. A representative segment of the x-t diagram for this particular mode is shown in figure 2.35. As shown in the diagram, interaction points between counter propagating waves are no longer confined to the transition points as was the case in the slapping mode. Here the interaction points vary much more readily throughout the detonation channel. At a given time there are as many as six waves present throughout the channel, with new waves being occasionally created and old waves dying out. This operation mode tends to be found on the boundary between the slapping mode and the detonation mode, and may represent a quasi stable transition mode between the two operating modes.

The waterfall spectra for the chaotic mode is composed of several broad spectral tones all of which are of approximately equal strength. As shown in figure 2.36

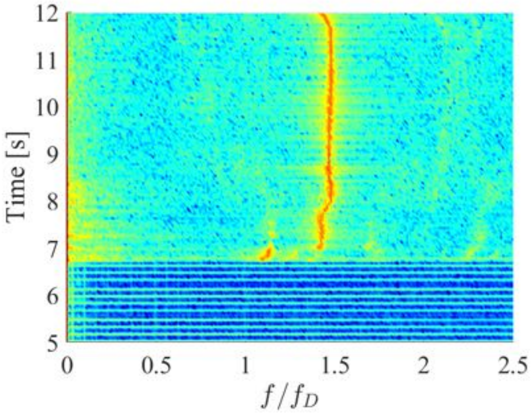

Figure 2.34: Waterfall spectra constructed from high speed pressure measurements. Spectra shown is for the slapping mode. Results shown for air mass flux of 59.2 kgs^{-1}m^{-2} at an equivalence ratio of 0.57.

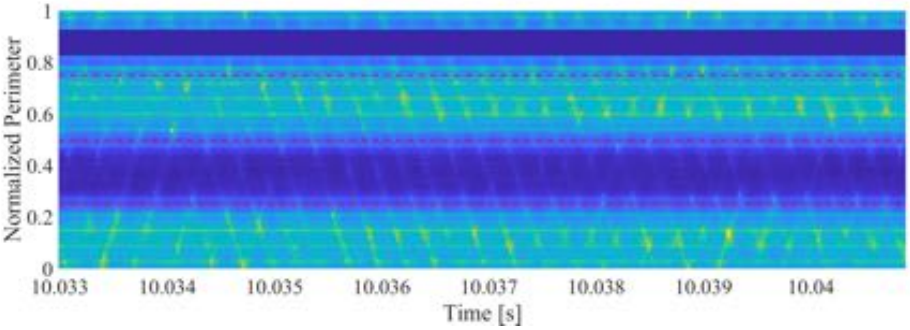

Figure 2.35: A portion of the x-t diagram constructed from high speed video. The red dashed lines denote the transition points between straight and curved sections. The regions from 0 to 0.25 and 0.5 to 0.75 are the two straight sections. Results shown for air mass flux of 87.2 $kgs^{-1}m^{-2}$ at an equivalence ratio of 0.77.

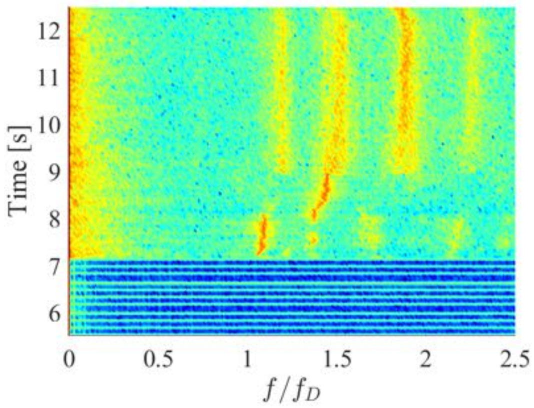

Figure 2.36: Waterfall spectra constructed from high speed pressure measurements. Spectra shown is for the chaotic mode. Results shown for air mass flux of 87.2 $\mathrm{kgs^{-1}m^{-2}}$ at an equivalence ratio of 0.77.

the main tones for this operational mode appear at $1.2f_D$, $1.5f_D$, $1.9f_D$, and $2.2f_D$. The large number of frequencies appearing in the spectra suggest a large amount of coupling between different components. These interactions are likely the cause of the seemingly random nature of the video and x-t diagrams.

2.6 Secondary Combustion: Parasitic and Commensal

2.6.1 General Observations in RT-RDC

Over the course of this study the same qualitative flow field to be presented below was observed for all mass flow rates and equivalence ratios combinations that resulted in stable two-wave operation. Here we will consider a set of representative still images taken from the high speed movie collected from one representative run to outline the general behavior of the flow field in the RDC. The set of representative still images is shown in figure 2.37. Because of the large dynamic range between the emission of the detonation wave and that of other modes of (non ideal) combustion, and because here we are primarily interested in non ideal combustion, in an attempt to emphasize regions affected by it we have contrast stretched the OH* chemiluminescence images.

Therefore, the emission associated with the detonation wave appears to saturate the image. In addition, because of the large dynamic range of the emission, we operated the intensifier at fairly large gates (2 μs) but moderate gains. As a consequence the strong emission associated with the detonation wave seems to have caused some level of electron depletion in the microchannel plate stack of the image intensifier (pore paralysis). This is rendered as a depleted (dark) region trailing the most intense regions of the detonation wave (see the dark region to the right of the detonation wave in the frame at 200 μs in figure 2.37) and corresponds to the location of the detonation wave in the previous frame. These depleted regions appear to persist one frame after exposure to high intensity events. Hence, care must be taken in interpreting regions devoid of OH* emission immediately trailing the detonation wave in frames containing the detonation wave (e.g., frame at 200 μs in figure 2.37).

Before we present the results of the OH chemiluminescence imaging on the RT-RDC, we first define three important terms that we develop and use in this work, and that have helped us differentiate between different regions where combustion occurs. This terminology has been informed from the results of the OH chemiluminescence imaging reported below, but we anticipate its definition to aide the discussion. The terms of interest are: (1) *parasitic combustion*, (2) *mixture or heat release leakage*, and (3) *commensal combustion*. The idea of parasitic combustion in RDC research has traditionally been associated with a combustion mode that is not associated with the detonation wave and usually is of deflagration nature. The term parasitic is typically used generically to refer to the negative impact non-detonation combustion has on the overall thermal efficiency that could be achieved with an ideal detonation because it subtracts energy to the support of the detonation wave. Thus, the term has been used to refer to any type of non-detonation combustion. However as it will be shown below, in this work we have identified two types of non-detonation combustion with distinct relationships to the detonation wave and separate origins, necessitating differentiation between the two. The first type of non ideal combustion occurs in the region upstream of the wave (relative to the wave) and has a direct negative impact on the detonation wave (decrease in wave speed and pressure rise). Thus, we term it *parasitic combustion*. The term parasitic is here used to draw an analogy with biology, where parasitic is used to describe the relationship between two species where one species benefits at the detriment of the other one [15]. In our use parasitic is taken with respect to the detonation wave where the combustion prior to the detonation has a direct negative effect on detonation properties (wave speed and pressure rise) because it takes away energy that is not released behind the wave to support it. The second type of non-ideal combustion occurs downstream of the wave and is a consequence of mixture or heat release leakage by which a portion of the heat release occurs after the sonic plane of the wave and therefore does not support its propagation. Although mixture or heat release leakage is a loss to the wave, the energy released after the wave does not directly influence the detonation wave in either a positive or negative wave. Thus, we term *commensal combustion* this type of non-ideal combustion that occurs past the wave. To draw again an analogy with biology, commensal is the biology term to describe the relationship between two species where one species benefits from the relationship but without either a positive or negative impact on the other one [15]. In our use commensal is again taken with respect to the detonation wave where combustion after the sonic plane of the wave neither improves or degrades performance because it does not impact the speed or pressure rise of the wave. It is important to separate these two types of non-ideal combustion because they are related to different phenomena and affect the wave in different ways. The parasitic form has a direct negative impact on wave properties, while the commensal form is a consequence of the non-ideal process of mixture and heat release leakage and does not itself have a direct impact on the detonation, although the presence of leakage does have an impact on wave propagation.

Figure 2.37 shows a time series of OH* chemiluminescence images showing the typical structure of the reacting field. At first, the flow field appears largely the same as the canonical flow field described above. In figure 2.37 we can recognize the detonation wave (DW) passing through the detonation channel (see frame at 200 μs), inducing back flow (BF) into the air inlet, which ultimately recovers and allows fresh mixture back into the detonation channel, beginning the filling process of the annulus. As the detonation passes by, large regions of OH* chemiluminescence persist throughout the post detonation products indicating commensal combustion (CC), suggesting that incomplete chemical reaction occurs through the detonation wave and continues behind the wave (see frame at 0 μs). Completion of combustion (heat release) past the detonation wave likely progresses through deflagration. Bordering on the commensal combustion (CC) is a triangular region devoid of reaction: this is the refill region (FFR) where fresh reactants are being injected and mixed (see frames at 0 μs and 50 μs). As time progresses, sustained emission can be seen on the border between the products from the cycle and the fresh reactants (CB1): this can be recognized to be the contact burning interface in the canonical RDC flow.

At some later times (100 μs frame) a second line of contact burning (CB2) is also visible below the first one. Between these two contact burn lines is a black

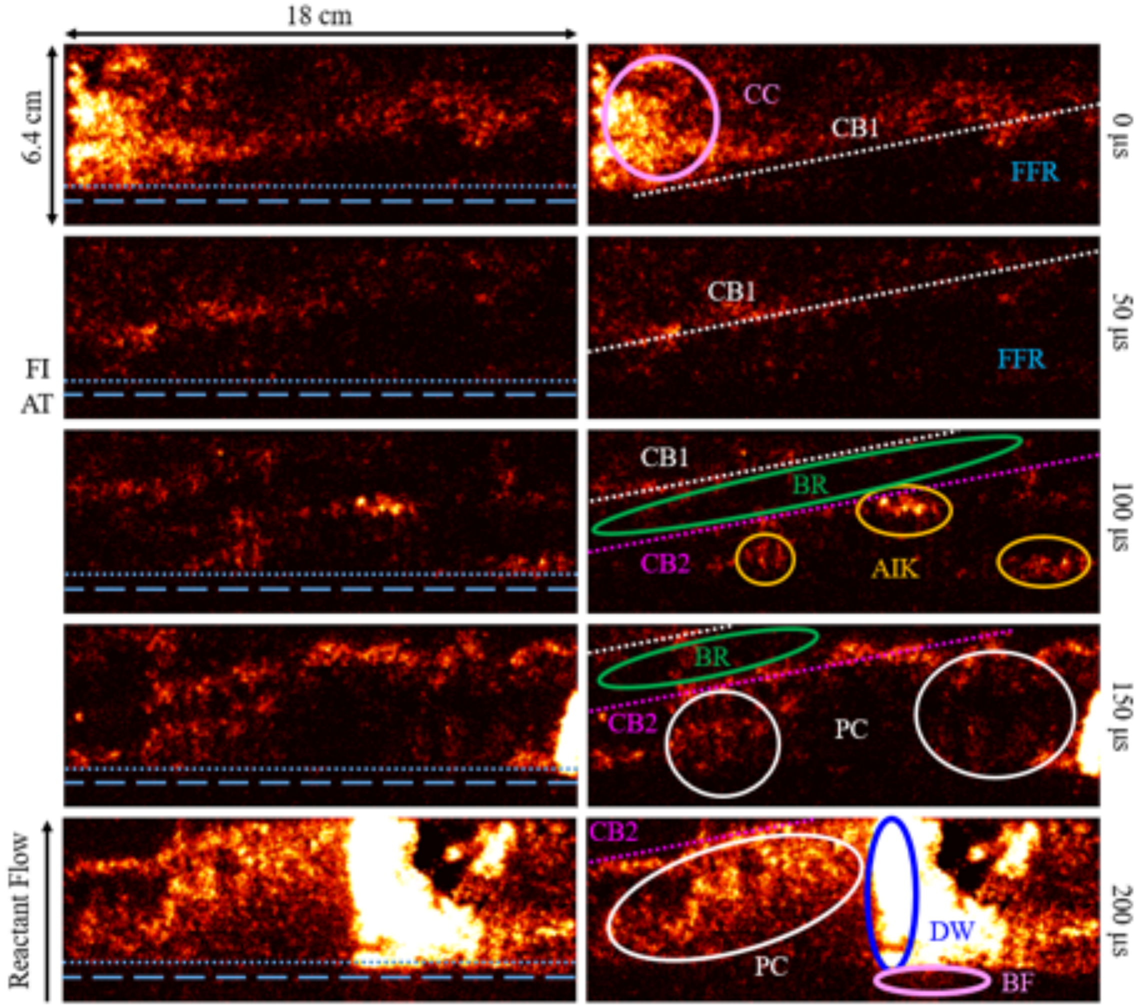

Figure 2.37: Time series of OH* chemiluminescence images showing the typical structure of the reacting field. The right set is an annotated version of the left set showing the main features: DW, detonation wave; CC, commensal combustion; BF, back flow into air inlet; CB1, contact burning 1; FFR, fresh fill region; BR, buffer region; CB2, contact burning 2; AIK, auto ignition kernels; PC, parasitic combustion; FI, fill injection line; AT, air throat. The dashed blue line represents the air inlet throat, while the dotted blue line indicates the position of the discrete fuel injectors.

region devoid of chemiluminescence, but not devoid of flow. Because the injection system for the air and fuel have different response times, one of them must recover first and begin filling before the other. This creates a region that is incapable of sustaining reaction either by being approximately pure air or approximately pure fuel. Chemical reactions can be sustained on the borders of this region, because of different stabilization mechanisms, but not within the region. We can define this region as a buffer region (BR) between the post combustion gases of the previous cycle and the fresh mixture of reactants. The first contact burning interface lies between hot products and the pure fuel/air buffer region. The ignition source for the first contact burn is likely the hot products from the previous detonation cycle. The second contact burning interface however, must be ignited through an additional mechanism. Some potential mechanisms for the second contact burn ignition include: (1) entrainment of hot products from recirculation zones around fuel injectors / air inlet; (2) hot components in the detonation chamber (e.g., a hot fuel injection rim); (3) hot products that were back flowed into the air inlet or fuel injection systems; and (4) autoignition induced by the coupling with secondary wave systems, for example acoustic waves co- or counter-propagating to the main detonation wave and induced by a combination of the acoustic characteristics of the air/inlet manifolds, the detonation chamber and the high amplitude, periodic forcing imposed by the unsteadiness associated with the propagation of the detonation wave along the annulus. While the exact mechanism is not currently known, the consequences of this early ignition of the fresh mixture can be clearly identified by the OH* chemiluminescence measurements. As the fill region ignites at various locations, the onset of additional OH* chemiluminescence can be seen throughout the fill region (see frame at $200 \mu s$). These secondary ignition events can be identified by spots of OH* chemiluminescence and are here referred to as autoignition kernels (AIK). These kernels continue to grow in size and intensity until they can coalesce and extend into a large fraction of the fill region. As a consequence, the detonation wave propagates through the partially burnt fill region, at which time the region has experience substantial parasitic combustion (PC) – see frame at $200\ \mu s$.

The processes described here and the formation of the reacting flow field structure seen in the time sequence of figure 2.37 repeat at every cycle as the detonation wave cycles through the combustor. The general pattern described here is seen in all of the two-wave detonation operation conditions we have investigated to date. The most noticeable difference between operation conditions is the size of the buffer region. The buffer region seems to grows larger with increasing fuel mass flow rate. This corresponds to an increasing pressure in the fuel plenum, which implies that the fuel

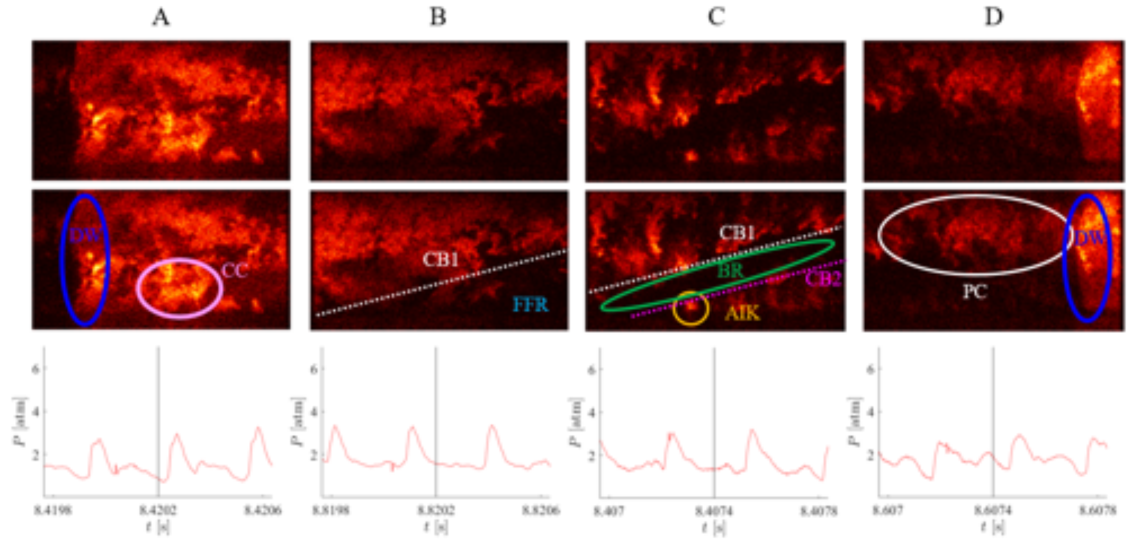

Figure 2.38: Four instantaneous snapshots taken at different points in the cycle, arranged to show a general representation of what the flow field looks like. In addition, the time of the frame is shown with respect to a pressure transducer out of frame to the left of the field of view.

injectors become in practice stiffer at a given operating condition. This suggests that the fuel speed is higher at the injector exits and that the response time of the fuel injector is shorter. Both of these effects would lead to a buffer region of pure fuel, or at least very rich in fuel, with the overall size of the buffer region increasing at larger fuel mass flow rates at constant air mass flow rate. A quantitative estimate of buffer region size has not yet been conducted and is left as future work.

Figure 2.38 shows an approximate arrangement of uncorrelated still OH PLIF images which, combined and timed together, comprise a pseudo-flow field over the detonation rotational cycle (the lower set is an annotated set of the top one). In addition, below each image pair is a pressure trace with a vertical line denoting the time at which the frame was captured. The sensor from which this trace was taken sits outside of the frame to the left of the images shown (see figure 2.3). Thus for example, the first image is taken before the detonation has arrived at the sensor. Based on a qualitative assessment of what observed from these initial OH PLIF measurements, the general flow field as it is rendered in the OH PLIF images agrees with our previously discussed observations using high-speed OH* chemiluminescence imaging under the same operating conditions in the RT-RDC.

In frame A, the detonation wave front is moving from right to left and it is about to exit the field of view propagating into the mostly dark refill region. In the wake of the detonation wave (DW), there are spatially extended regions where OH is present from the chemical reactions that have just taken place. There are large regions of spatial non-uniformity including dark regions and bands, which we will discuss at greater length in the next section. In addition to dark regions there are portions of the OH distribution that are much stronger and brighter than what is typically seen across the frame, especially towards the lower part of the frame. These regions of intense OH correspond well with previously identified regions of continuing commensal combustion (CC). These are regions where chemical reaction occurs far behind the detonation front.

As the detonation wave moves further and further away in frame B, the injection scheme begins to recover from the sharp pressure rise and it begins to issue fresh reactants (FFR) into the channel. The fresh fill region (FFR) is bounded by a region of the post combustion products that typically still exhibit some ongoing reaction, termed a contact burn (CB1) due to the contact of detonation products with new reactants. The boundary between these two regions is highly corrugated with a variety of folds and structures present in the OH distribution. This corrugation is likely caused by a number of factors including the presence of discrete injectors and the starting jet vortices that likely accompany the jet start up process at the beginning of each cycle.

In frame C long after the detonation wave has passed the injectors, we are able to see a buffer region (BR) devoid of any OH surrounded on either side by contact burns (CB1) and (CB2). The buffer region (BR) is devoid and has been devoid of chemical reaction since its introduction into the detonation channel. In RDCs, the response time of fuel and air injectors are likely different, with one responding before the other. The difference in response times makes it likely that air or fuel is issued into the detonation channel before the other, creating a buffer region of pure air or fuel, depending on which one responds the fastest. In a companion work to the current one [16], we have investigated the response time of both air and fuel injectors for the RT-RDC. For the condition for which these images were taken, we have found longer air response times[16], suggesting this region is composed predominantly of fuel – thus if this region would transition through the RDC unreacted, it would contribute to incomplete combustion. This dark band of pure fuel is then bounded by two contact burn lines representing continuing or partial reaction in the detonation products as well as in the fill region. Lastly, in frame C we can observe the presence of what appears to be an auto ignition kernel (AIK) in the bottom center of the picture. In our previous work on the reactions present in the detonation channel, it was unclear whether the source of ignition in the fresh fill region (FFR) was contact with the products, through interruption of the buffer region, or through some other source. Based on the images we have observed that contain this flow feature, we believe it is likely that the buffer region represents a sufficient obstacle to the inter-mingling of hot products and the fresh fill region, and therefore there is another more significant ignition source to the fill region. The presence of what appears to be an auto ignition source low in the fill region further suggests that ignition is likely influenced by another mechanism separate from the hot products flowing upward.

In frame D, regions with broad distribution of OH are present, which are the result of parasitic combustion (PC) in the fresh fill region that originated with the auto ignition kernels (AIK). This combustion is not yet complete and so the oncoming detonation wave (DW) is still able to propagate through the partially burnt mixture to complete the cycle. The presence of any of these features can typically be seen in any cycle as we had discussed in our previous work, but it is worth mentioning that the intensity and exact distribution of any of these features are likely to vary with other effects, such as secondary wave propagation, coupling of plenums with the detonation channel, and specifically to the racetrack geometry, the influence of the curve to straight transitions present in the RT-RDC. Currently we believe that our PLIF imaging corroborates what we previously observed with OH* chemiluminescence, but have yet to acquire a large enough number of images with sufficient timing control to confirm our previous observations by leveraging the spatial and temporal resolution that the PLIF technique offers.

2.6.2 0D model of Parasitic combustion impact on Detonation properties

The OH* chemiluminescence visualizations conducted and discussed in previous sections have highlighted the presence of non-ideal behavior in RDCs. The first is parasitic combustion, the partial combustion of the fresh mixture of reactants; the second is commensal combustion, the consequence of the non-ideal mixture leakage process. These two combustion types have different natures and implications on the properties of the detonation wave. However, the presence of both types ultimately limits the thermodynamic benefit that could be expected from the use of a detonation wave in an energy conversion system. We can think of parasitic combustion as a type of vitiation, while commensal combustion indicates the existence of mixture leakage through the detonation wave (C-J plane). Although both of these processes are important to understand and resolve for the effective implementation of detonation-based combustion in practical energy conversion systems, in this work we primarily focus on the effects of vitiation induced by parasitic combustion on the detonation wave properties, leaving the effects of mixture leakage to future work.

Before we look closely at the potential impact of vitiation effects on the properties of the detonation wave it is worth nothing that, at least within an ideal one-dimensional representation of a detonation wave structure, the effect of mixture leakage is that energy released past the sonic plane in the wave will not directly support the detonation. This will result in reduced detonation wave speed and pressure rise than without leakage. Recent detailed computations [17] of RDC flowfields have shown that the detonation wave in practical RDEs may be a non-compact (distributed) region rather than a sharp discontinuity, which may be one of the key factors influencing mixture leakage. While this leakage is likely an important factor in determining the detonation properties of practical RDC systems, a quantitative evaluation of mixture leakage impact on detonation properties is left for future work.

Let us now focus more in some detail on the effects of vitiation due to parasitic combustion of the unburnt mixture on the detonation wave. Parasitic combustion in the fresh reactants mixture has two effects. The first effect is that partial combustion of the fresh mixture consumes part of the unreacted mixture, releasing energy before the detonation wave that is then not available to support the detonation wave. The second effect is that in practice, partial combustion of the fresh mixture vitiates the mixture. As a result, the local composition of the mixture is altered, fuel and oxidizers are partially consumed to leave products, and the temperature of the mixture is raised. The temperature raise ahead of the wave alone, and its effects, could be significant. An increase in temperature of the mixture ahead of the detonation wave can lower the effective propagation Mach number of the incoming wave, even at fixed propagation speed. This would lead to a reduction in compression across the shock wave, which can affect the stability of the wave, for example by altering the induction time and/or cell size, as well as the effective pressure gain that could be expected. It is also important to note that a similar effect would exist if, instead of partially consuming the fresh mixture due to premature ignition, the fresh mixture would entrain post-combustion gases from the previous cycle. For example, entrainment could occur

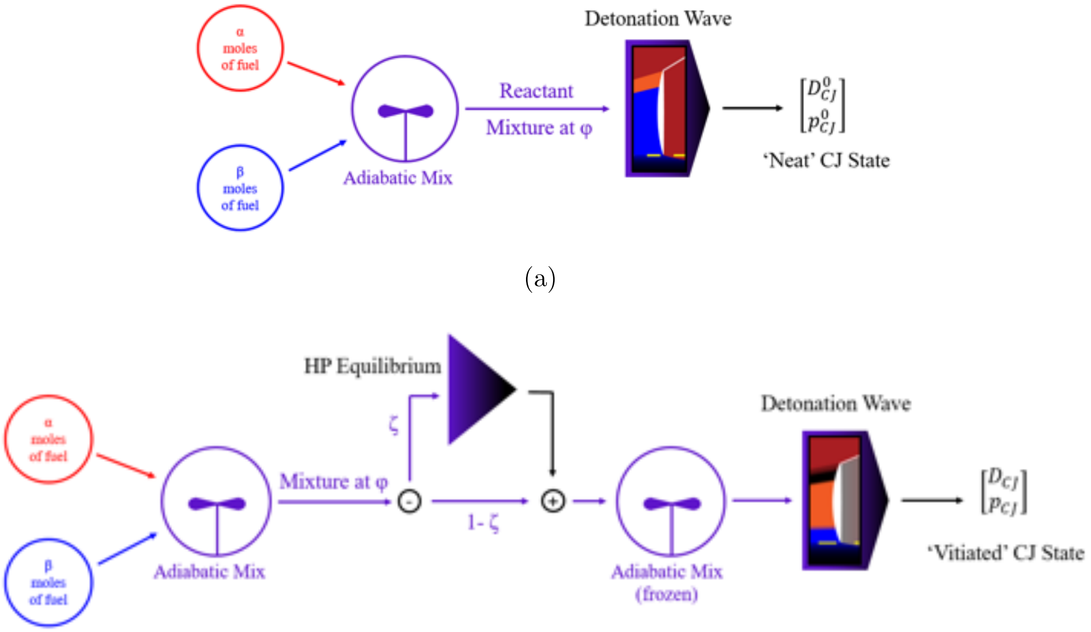

(a)

(b)

Figure 2.39: Schematic representation of the zero-dimensional model constructed to assess vitiation effects due to partial combustion of the mixture on detonation wave properties: a) ideal (neat) detonation case; b) vitiated detonation case.

at the beginning of the recovery of the air/fuel streams when they need to displace existing post-combustion gases from the current cycle, or because of the presence of flow recirculation regions (e.g., around the fuel injectors) that trap post-combustion gases but release them into the fresh unburnt mixture as it forms.

To quantitatively evaluate the potential impact of vitiation on the detonation wave we have constructed a zero-dimensional model of a detonation wave that would evolve into a partially reacted air/fuel mixture. The model is based on a chemical equilibrium model of the detonation wave and uses the Chemical Equilibrium and Applications (CEA) code [11]. The model, which is outlined schematically in figure 2.39, is constructed based on the following considerations and targets specific detonation properties, such as the detonation wave speed and pressure ratio:

1. Define an initial fuel/air mixture based on the global equivalence ratio ϕ as-

suming ideal mixing at some initial pressure and temperature;

2. Take a volume fraction of the mixture ζ and compute its equilibrium composition and properties through a constant pressure combustion process (deflagration);

3. Take the resulting equilibrium composition at its equilibrium temperature and mix it adiabatically with the remaining $(1 - \zeta)$ unreacted portion of the initial mixture while freezing the chemistry;

4. The resulting mixture defines the vitiated mixture at some elevated temperature that depends on the vitiation fraction ζ and it is used to compute its detonation properties using the chemical equilibrium detonation code;

5. The resulting C-J state dictates the wave speed D_{CJ}, pressure (p_{CJ}) and temperature (T_{CJ}) ratios for a detonation that would propagate through the vitiated initial mixture, where the degree of vitiation is described by the vitiation volume fraction ζ.

For the purpose of evaluating this model on available data, we have considered only hydrogen/air mixtures at an initial pressure of 1 atm and temperature of 295 K, and over a range of equivalence ratios. The detonation wave speed D_{CJ}, pressure p_{CJ} and temperature T_{CJ} computed for the vitiated mixture over a range of vitiation fraction are then compared to the corresponding values obtained for the neat mixture (i.e., for $\zeta = 0$). Values for the neat mixture are indicated with a superscript '^{o}'.

The resulting detonation properties normalized by the corresponding value of the neat mixture as a function of vitiation volume fraction are shown in figure 2.40 in the form of isocontour lines. The results show that for the range of conditions considered, vitiation has the effect of lowering the detonation speed and pressure ratio relative to the ideal un-vitiated case. The pressure ratio is particularly sensitive to vitiation. It has a rapid drop off for even small amounts of vitiated volume fraction, dropping to 50% of the un-vitiated pressure ratio for a vitiated volume fraction of 12%. In contrast, detonation speed remains relatively high even for large vitiated volume fractions, with 50% vitiated volume fraction resulting in only a 20% decrease in wave speed. For low vitiation fractions there is a weak dependence on the equivalence ratio of the initial mixture over the range considered. Equivalence ratio effects become more important as the the volume fraction of vitiated flow grows larger, with leaner initial mixtures having a smaller deficit in detonation properties.

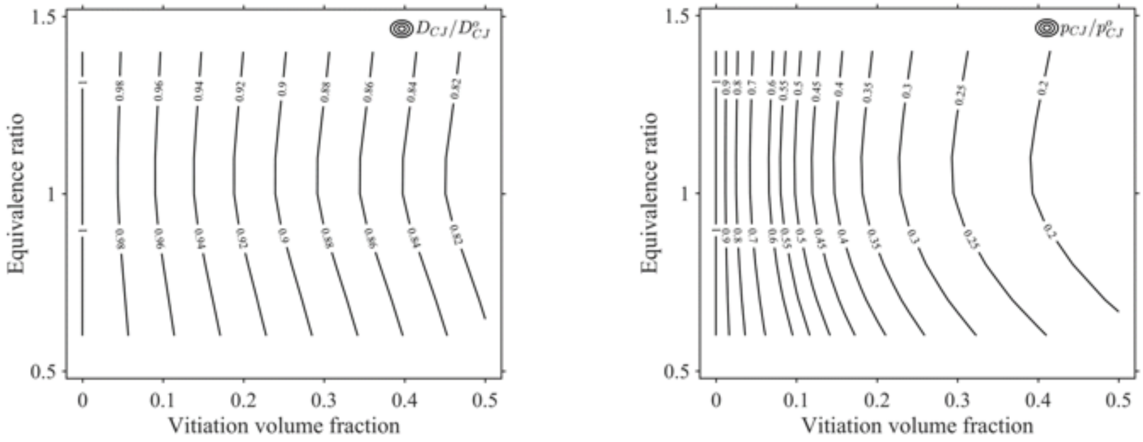

(a) (b)

Figure 2.40: Isocontour plots of (a) D_{CJ}/D^o_{CJ} and (b) p_{CJ}/p^o_{CJ} as a function of equivalence ratio and vitiation volume fraction of the initial mixture for a hydrogen/air mixture initially at 1 atm and 295 K.

In order to assess the validity of this model we have constructed a plot comparing the measured detonation properties, normalized by the corresponding values assuming an ideal detonation at the global equivalence ratio, and those computed from the zero-dimensional model of figure 2.40. The comparison is shown in figure 2.41. One set, described by the ▲ symbols, refers to the computed data. The relationship between p_{CJ}/p^o_{CJ} and D_{CJ}/D^o_{CJ} as ζ is varied from $\zeta = 0$ (where $p_{CJ}/p^o_{CJ} = 1$ and $D_{CJ}/D^o_{CJ} = 1$) to $\zeta = 0.5$ (where $p_{CJ}/p^o_{CJ} \approx 0.2$ and $D_{CJ}/D^o_{CJ} \approx 0.8$) follows an exponential-like curve. The second set, described by the other symbols, corresponds to measurements taken on our three air inlet / fuel injection schemes in our six inch round RDC for the operating conditions tested thus far that resulted in detonation operation. The data measured with RDC operation cluster together around a region corresponding to about 78% of the ideal CJ speed and about 20% of the CJ pressure ratio across the wave. Measurements align with computed values at large values of vitiation volume fraction, on the order of $\zeta = 0.5$. This analysis suggests that there may be a link between the reduction in wave speed and peak pressures seen in operation and the amount of vitiation due to parasitic combustion present in the RDC. However, in this work we have identified that there are two sources of heat release loss at the wave, one due to parasitic combustion ahead of the wave, which

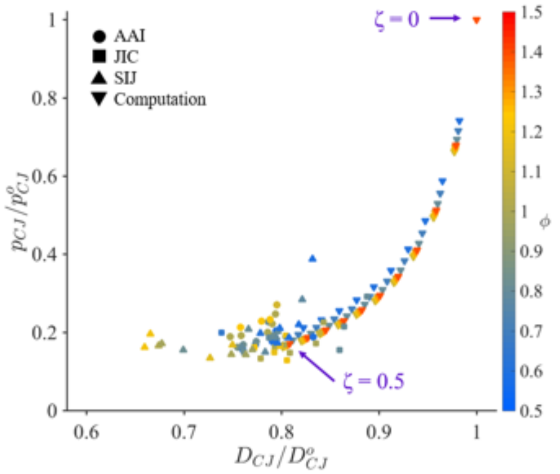

Figure 2.41: Comparison between idealized computations of detonation properties under varying degrees of vitiation and measured detonation properties. AAI is an axial air flow configuration, JIC is a radial jet in cross flow configuration, and SIJ is a rocket style semi impinging jet configuration.

is considered by this analysis, and the other due to mixture leakage which leads to commensal combustion behind the wave. It is the combination of these two effects that result in the observed reduction of wave speed and peak pressure. Future work will integrate the second mechanism of mixture leakage into our zero-dimensional model, with consideration being given to additional mechanisms such as non-homogeneous mixing and lateral relief effects.

2.6.3 Quantification of Parasitic and Commensal Combustion *in-situ*

2.6.3.1 Instantaneous OH* Profiles

Before considering the phase-average profiles, the instantaneous profiles are examined. A short duration of the raw PMT signal is shown in Figure 2.42, where 7 detonation cycles are captured in a window of 2 ms. This figure is from the steady portion of a run with a mass flux of 83 $\mathrm{kg\,s^{-1}\,m^{-2}}$ at $\phi = 1$. A quick qualitative analysis of these profiles shows that combustion occurs before and after the spike in signal caused by

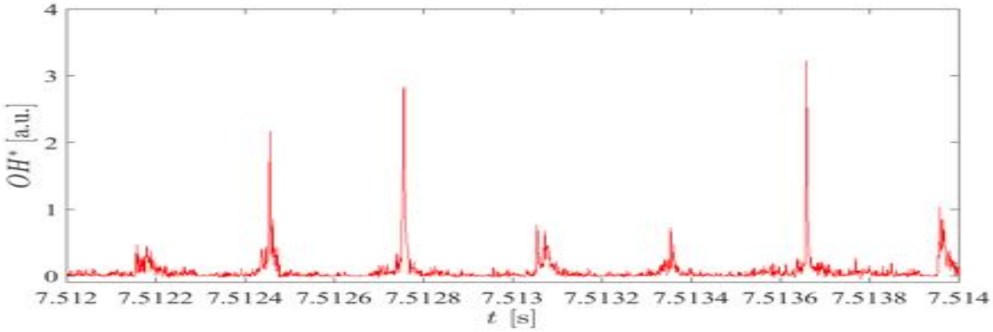

Figure 2.42: Time trace of OH* signal for 2ms during steady portion of run with a mass flux of 83 $\mathrm{kg\,s^{-1}\,m^{-2}}$ at $\phi = 1$

the passage of the detonation wave. Regions of large intensity exhibit values that are greater than the noise in the data acquisition that can be seen between cycles when emission does not occur. We generically associate the presence of these regions with *secondary combustion*. The prominence of these secondary combustion regions varies from cycle to cycle, as indicated by the variation in the shape of the profile for each cycle. The observed variation is believed to be associated with the chaotic nature of the combustion events occurring before and after the detonation wave, but also within the (broadened) detonation wave and its propagation dynamics within the turbulent field provided by the injection system, that are observed by the chemiluminescence detection systems. Some of these effects have been observed both computationally [18, 17] and experimentally [19] in our systems. What is of most interest here, is the phase-average behavior, and to establish whether secondary combustion do exist on average, quantify its extent, and analyze its effect in an average sense.

In addition to noting that secondary combustion (pre- and post-detonation wave) does exist instantaneously and its onset and manifestation appear rather chaotic, it is also important to note that there is a significant cycle-to-cycle variation in the observed OH* chemiluminescence observed at a fixed point. This implies that there potentially is a significant cycle-to-cycle variation in the onset of pre-ignition ahead of the wave and local heat release evolution. This is most notable in the difference of the amplitude of the signal spike caused by the detonation wave, but also by the structure of the profiles pre- and post-detonation wave. To further evaluate cycle-to-cycle variations, the total heat release seen across each individual cycle i ($Q_{T,i}$), as defined by the total area under the OH* chemiluminescence curves for each cycle, was computed during the steady portion of the run. From there, a probability density function (PDF) of this quantity provides a sense of the magnitude of these variations. Two examples are shown in Figure 2.43. The total heat release from the phase-average profiles (Q_T), which will be discussed in greater detail in a later section, is shown for reference as the vertical black dash line. Figure 2.43(a) is constructed from the same case of Figure 2.42, whereas Figure 2.43(b) is taken from a run at a lower mass flux (mass flux of 51 $\mathrm{kg\,s^{-1}\,m^{-2}}$ and an equivalence ratio of 1.0). This second case is provided to show that while the phase-average value of Q_T is a good representation in some runs, it is less representative in some other cases because of large cycle-to-cycle variations and skewness in the distribution of cycle-average values. This should be kept in mind during the discussion of the results from the phase-average profiles.

In general, the distribution of $Q_{T,i}$ is fairly broad, potentially suggesting a significant cycle-to-cycle variation in the heat release distribution. The PDF shows that the heat release at each cycle may vary from nearly zero to twice the value of Q_T, which is a significant amount of variability. We hypothesize that this may be a result of a secondary wave interacting with the detonation wave, potentially creating variations in the progress of reaction at the detonation wave. Further investigation will be required to gain more understanding into the cause of this large variation, but it should be noted that since this is nearly a point measurement there is potential that the detonation wave exists more prominently at other points within the channel. So, the variability observed here can be associated with the cycle-to-cycle variation of the propagation dynamics of the wave. The presence of skewness in the distributions of Figure 2.43 is currently not known.

2.6.3.2 Determination of Combustion Regions in Detonation Cycle

While the instantaneous profiles exhibit secondary combustion characteristics as previosuly discussed, to easily define the regions, phase-averaging is applied. Figure 2.44 shows an example of the phase-average distribution of OH* chemiluminescence acquired for operation at 0.3 kg/s and $\phi = 0.6$, and introduces some important features of the phase-average profile. All cases tested show qualitatively similar profiles. As indicated by the presence of chemiluminescence, in all cases tested, heat release occurred pre- and post-detonation. This supports the hypothesis that there exists regions where secondary combustion in the form of deflagration occur in the detonation cycle. These secondary combustion regions are regions of reacting fuel/oxidizer mix-

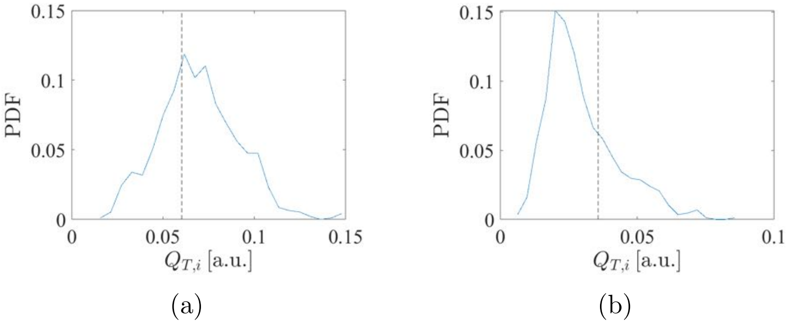

Figure 2.43: Probability density function of cycle heat release for two different conditions: mass flux of (a) 83 kg s^{-1} m^{-2} and (b) 51 kg s^{-1} m^{-2} at $\phi = 1$. Dashed black line indicates the phase-average value, Q_T

ture that do not directly support the detonation wave or even impede its evolution. Figure 2.44 identifies the various regions where heat release occurs as a consequence of the different modes of combustion, as well as important points along the detonation cycle that will be discussed below.

While the combustion regions are discernible, a systematic method to define critical events during a detonation cycle is needed to ensure a consistent discussion between runs. In an ideal cycle where only the detonation wave is present, no OH* emission prior to the detonation wave would exist. The point at which the OH* emission increases from the baseline can be classified as the ignition event. If this ignition event occurs before the detonation wave, which is identified as a very sharp rise in OH* emission, the ignition event is associated with ignition of the fresh fuel/oxidizer mixture ahead of the detonation wave and thus, it can be associated with parasitic combustion. The region where parasitic combustion occurs ends with the detonation wave arrival. While there is a continual increase of OH* emission during parasitic combustion, the slope of the OH* emission abruptly increases upon the arrival of the detonation wave. This is expected since chemical reactions would be the greatest within the detonation wave. After the peak OH* emission is reached, the signal then begins to decay in a manner similar to what was seen in the model shown previously in Figure 2.6. In nearly all cases observed, the decreasing signal from the detonation wave reaches a point where the manner of decay changes. This is another critical point, and indicates the start of commensal combustion. This point can be associated with a slow decay or plateau in OH* emission, or even with an increase in OH* emis-

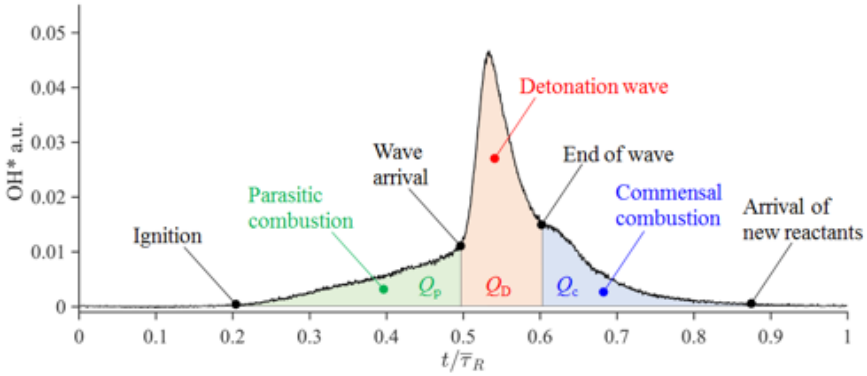

Figure 2.44: Representative phase-average cycle of OH* emission detailing the different combustion regions and critical points, such as ignition of the fresh mixture ahead of the detonation wave.

sion to define a second point of maximum OH* emission (basically a second "bump" in the profile). After this, the OH* emission begins to decrease again, though at a rate different than that associated with the detonation wave. The decay continues until the signal reaches the baseline, which is believed to indicate the arrival of new reactants for the next cycle. Currently, we have not developed an automated algorithm based on an unequivocally, well-defined measure for determining these critical points and combustion regions, so at this stage they were manually selected based upon the discussed trends.

2.6.3.3 Definition of Heat Release Budget

Despite the limitations that were discussed in previous sections, we assumed that the OH* emission measured can be used as a surrogate measure of heat release for H_2/air combustion. Thus, an amount of heat released within a portion of the detonation cycle can be defined by integrating under the phase average OH* emission curve. Four heat release values are defined in this study for each combustion region: the total heat release (Q_T), heat release associated with the detonation wave (Q_D), heat release associated with parasitic combustion (Q_P), and the heat release associated with commensal combustion (Q_C). The definition of these four quantities is shown graphically in Figure 2.44. The breakdown between the three regions (parasitic, detonation, commensal) follows what described in previous sections. While not found in this work, a theoretical total heat release (Q_T^o) can be defined for the purpose of discussion. Unless complete combustion would occur within the measurement point, the observed Q_T would be less than Q_T^o. As of now, we do not have a means for evaluating the relationship between Q_T and Q_T^o other than just noting that they liekly are different. However independent of this, the four heat release values defined here satisfy the following relationship:

$$Q_T = Q_D + Q_P + Q_C$$

Before looking into the heat release within the individual combustion regions, we first consider the effects of mass flux and equivalence ratio on Q_T. The results for the entire operation map are displayed in Figure 2.45(a). The total heat release over the cycle depends on the equivalence ratio, with the greatest heat release value being at stoichiometric conditions or for fuel rich cases. The total amount of heat release seen for the fuel rich cases are either approximately the same or slightly less than what is seen at stoichiometric conditions, which is expected based upon the previous discussion (see Figure 2.7). Additionally, the total heat release has a non-linear dependence with mass flux. It should be noted that, as defined here from the OH* chemiluminescence profile, the estimate of the heat release (e.g., Q_T) is the heat release per unit volume. Since the probe volume remains constant for all conditions, the increase in Q_T with mass flow rate (mass flux) is to be attributed to a local increase in gas density as mass flow rate increases.

By utilizing the total heat release of the cycle, a qualitative measurement of the level of completion of the combustion within the cycle can be made. Normalizing Q_T by the mass flow rate of the fuel and plotting it against the mass flow rate of air, as seen in Figure 2.45(b), should result in a constant value across the range of air mass flow rates if the combustion reached completion within the probe volume. If all the available fuel and oxidizer underwent combustion, a constant value of the energy would be released. However, based upon our results, we observe that this is not the case. While there are some equivalence ratios (such as $\phi = 1.0$) where the value is nearly constant, this is not the case for all equivalence ratios. Therefore, the degree of completion of combustion may have a dependence upon mass flow rate. This dependence may be controlled by the degree of mixing between fuel and oxidizer, or the overall morphology of the flowfield produced by the injection conditions and geometry. Additionally, all cases at different equivalence ratios should collapse to a single constant value. This indicates that even though there may be some equivalence

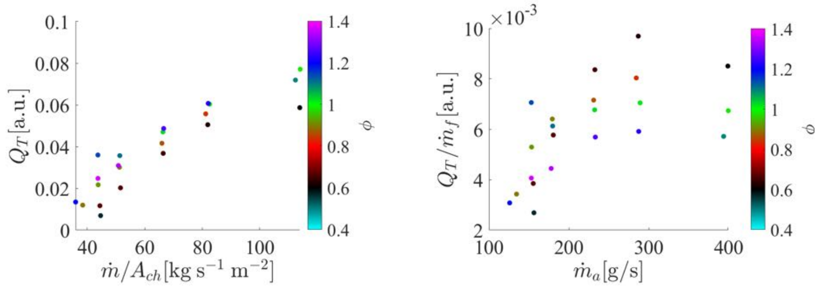

(a) (b)

Figure 2.45: a) Total heat release seen across entire operation map with strong dependency on mass flux. b) Total heat release normalized by fuel mass flow rate shows varying degrees of combustion completeness.

ratios at which the completion level is constant with mass flow rate, there remains an effect associated with the equivalence ratio. This may be due to chemistry or mixing effects. While quantitatively the level of completion cannot be found, nor can a concrete explanation to the variations observed be provided, it is important to note that complete combustion does not appear to be occurring consistently at the measurement point within the RDC. However, we can not conclude anything about whether complete combustion is reached by the exit of the RDC or not.

2.6.3.4 Variations in Profile with Mass Flux

Although detonative operation was seen in the unstable region of the operation map, the detonation wave under those conditions exhibited a wider spread of cycle-average instantaneous wave speeds when compared to the stable operation points. This more chaotic behavior of the detonation wave caused the phase-average shapes to not converge to a smooth profile for the lower mass fluxes and higher equivalence ratios. For instance, three phase averaged profiles at a constant equivalence ratio of 1.0, but with increasing mass fluxes are shown in Figure 2.46. The lowest mass flux case shown has not converged to a smooth profile and it exhibits a smaller range of values. Nevertheless, the overall phase-average profile of heat release distribution can still be inferred. Note, that in order to compare the timing between the three profiles, the point of ignition ahead of the detonation wave were aligned and made so that the detonation arrival is set to be around half of the average cycle rotational time ($\bar{\tau}_R$). By doing

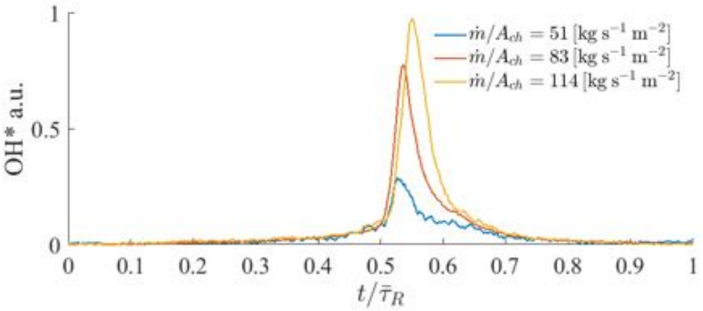

Figure 2.46: Phase averaged OH* profiles at a fixed equivalence ratio of 1.0 with varying mass fluxes.

this, the slight differences in delay between ignition and detonation wave arrival can be properly shown.

2.6.3.5 Dependence of Heat Release Regions on Operating Condition

After defining the combustion regions for each set of conditions, the heat release for each combustion region in the cycle can be found. The results of these heat releases are displayed in Figure 2.47. Both Q_D and Q_P increase with mass flux, though Q_D increases at a much greater rate than Q_P. Furthermore, Q_D is generally significantly greater than Q_P, except at lower mass fluxes where the two are comparable. As was demonstrated during the discussion of the ignition point, the point at which parasitic combustion begins in the detonation cycle relative to the detonation wave is constant for a given equivalence ratio. While the time parasitic combustion exists is constant, the amount of parasitic combustion increases in this constant window with mass flux. This indicates that the source of ignition for the parasitic combustion may be independent of the relative distribution of fuel and oxidizer or overall conditions of operation, but may instead depend on a mechanism that is associated with the global equivalence ratio. An increase in Q_P with mass flux may remain linked to an increase of gas density as discussed previously in regard of Q_T.

The scale of commensal combustion is similar to that of parasitic combustion, though is on average slightly greater and remains fairly constant with mass flux for a given equivalence ratio This is true except at low mass flow rates where depending on equivalence ratio, Q_C is either greater or less than the nearly constant value ob-

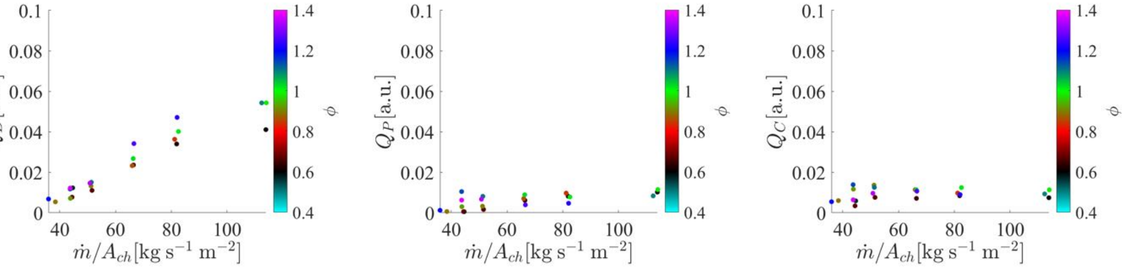

(a)

(b)

(c)

Figure 2.47: Variation of heat release associated with the three combustion regions: a) detonation b) parasitic c) commensal, as a function of operating condition.

served at higher mass flow rates. This suggests that the unknown phenomena that causes commensal combustion is likely independent of the mechanism that causes parasitic. If they were linked, increasing parasitic combustion would cause a change in commensal combustion, which was not observed. We also hypothesize that commensal combustion can continue to evolve as the flow expands further downstream as it moves along the detonation channel. While no measurements have been taken to demonstrate this, at this stage we cannot conclude that commensal combustion remains a constant amount for the average cycle at all locations in the channel.

2.6.3.6 Fractions of Total Heat Release

Additional information can be learned about the combustion occurring in a cycle when looking at the fraction of the heat release from the individual combustion regions to the total heat release, as shown in Figure 2.48. This fraction is termed the relative heat release of the combustion region. The equivalence ratio causes the data to spread out, but clear trends at constant equivalence ratio can be seen for both detonation and commensal combustion. At higher mass fluxes, the relative heat release of the detonation is greater than what is seen at lower mass fluxes. At low mass fluxes, the relative heat release associated with detonation can reach as low as about 30% of the total across the cycle at the probe point. However, at higher mass fluxes the relative detonation heat release can reach about 80%, which approaches an ideal cycle, since in an ideal cycle, 100% of the chemical energy would be released within the detonation wave, and possibly within the measurement probe volume.

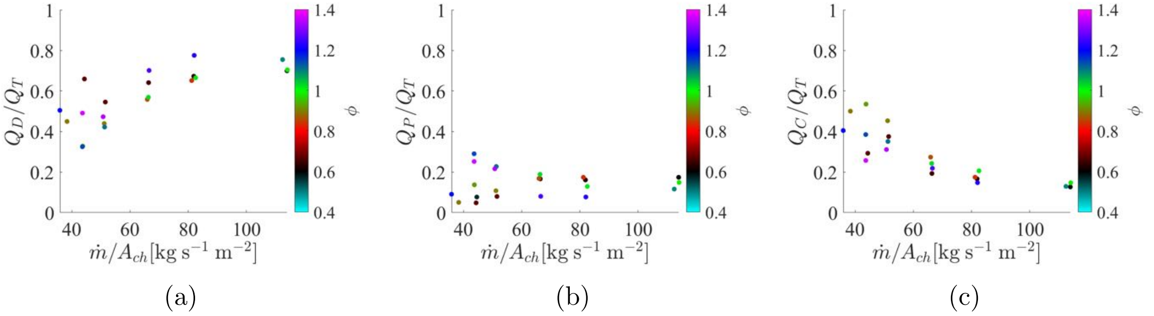

(a) (b) (c)

Figure 2.48: Heat release of the three distinct combustion regions a) detonation b) parasitic c) commensal relative to the total heat release seen across the cycle.

Interestingly, the relative heat release of commensal combustion has the opposite trend of the relative heat release of detonation. In fact, it appears that the relative heat release of commensal and detonation are linked together such that when one increases the other decreases. To determine the link between these combustion regions requires the consideration of the parasitic combustion. Parasitic combustion quickly reaches a constant value for a given equivalence ratio. The highest relative heat release was 25% though on average the relative strength is 15% or less for most conditions. It was observed in Figure 2.47(c) that the total heat release in the commensal combustion region does not vary much across the different conditions. Thus, an overall increase in heat release in the cycle would result predominantly in an increase to the heat release supporting the detonation wave. If commensal combustion does increase further downstream as theorized, this relative heat release for the detonation may be an upper bound of different spatial locations in the channel.

2.6.3.7 Variations in Detonation Speed

According to the ZND model, a detonation wave is a thin shock wave followed by a region of heat release that sustains the wave. Thus, it would follow that an increased amount of heat release in the detonation wave should positively affect the properties of the detonation wave, such as its speed. In order to draw proper comparisons between the different operating conditions, the measured (average) detonation velocity was normalized by the Chapman-Jouguet velocity. When this normalized velocity is plotted against the total heat release across the cycle, as seen in Figure 2.49(a), a

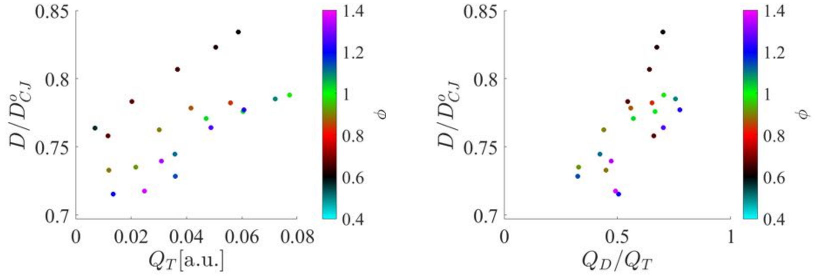

(a) (b)

Figure 2.49: Normalized wave speed plotted against the a) total heat release b) relative heat release of the detonation wave.

direct relationship is seen, where an increase in Q_T corresponds to a larger normalized velocity. However, this relationship varies between different equivalent ratios, with larger (normalized) detonation speed values occurring for lean operating conditions.

While the normalized detonation velocity has a dependence on Q_T, the presence of parasitic and commensal combustion cause the relationship to have an additional layer of complexity. Since there is heat release associated with both of these, the increase in Q_T does not linearly correlate to an increase Q_D. A better measure, then, would be the relative heat release of the detonation, as this should remove the dependence on the secondary combustion regions. Figure 2.49(b) shows how the normalized detonation velocity varies with this fraction. While not as obvious as the relationship with Q_T, the normalized speed increases when more of the heat release is associated with the detonation wave, for a given equivalence ratio. This supports the idea that the existence of secondary combustion regions cause the detonation wave to be slower than what would be expected from an ideal case. It should be pointed out, that the presence of parasitic combustion has a direct effect on the propagation properties of the detonation wave that is not directly captured by the results and discussion of Figure 2.49(b). In particular, a zero-dimensional analysis assessing the impact of vitiation of the fresh mixtures that the detonation wave propagates through, suggests that the detonation speed is somewhat reduced by vitiation. Furthermore, this analysis suggests that the peak pressure behind the detonation wave is strongly attenuated. Therefore, decoupling the effects of parasitic combustion from the effects of mixture or heat release leaking through the detonation wave (and contributing to parasitic combustion) will require an additional level of analysis of these results,

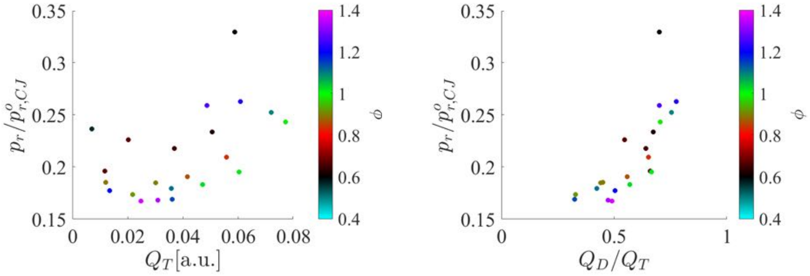

(a) (b)

Figure 2.50: Normalized pressure ratio across detonation wave plotted against the relative heat release of the detonation wave.

which we are currently exploring.

2.6.3.8 Variations in Pressure Ratio across the Detonation Wave

In addition to reported detonation wave speeds being less than the ideal model, the pressure ratio across the detonation wave as seen in experimental RDCs is typically significantly less than what is predicted by ideal models. Although a primary contribution to the attenuation of the peak pressure at the detonation wave must be attributed to the finite response of the methods used to measure the dynamic pressure, another significant contribution is associated with the effects of secondary combustion. In general, it is likely that the effects altering wave speed equally alter the pressure ratio. Therefore, a relationship between reduced wave speed and reduced pressure ratio may be expected, both of which controlled by how the heat release is distributed across the detonation wave.

Figure 2.50(a) summarizes the pressure ratio measured across the detonation wave normalized by the ideal C-J value at the nominal conditions ($p_r/p^o_{r_{CJ}}$, where p_r is the ratio of the maximum to minimum pressure in the cycle, as a function of Q_T. The pressure ratio was defined based upon the high-speed pressure measurement taken from a similar axial location. Despite the near direct relationship found between Q_T and wave speed, there is significantly more variation in the dependence between the (normalized) pressure ratio and Q_T across the equivalence ratio and mass flux ranges.

To emphasize any relationship between detonation wave properties and heat released at the detonation wave, the results of Figure 2.50(a) are cast as a function of relative heat release of detonation in Figure 2.50(b). In this form, there is a noticeable trend between the relative heat release at the detonation and the measured pressure rise. If one follows the relationship for a constant equivalence ratio, this relationship is not constant, but on average the pressure ratio increases as the relative heat release of the detonation wave increases. The explanation of this trend follows a similar explanation for the similar trend seen in detonation wave speed. However, it has to be pointed out again that the presence of parasitic combustion and its direct effect on detonation properties, render a direct interpretation of the effects of the heat released at the detonation wave more difficult, and additional work is required to clarify these aspects.

Chapter 3

Computational Activities

3.1 Introduction

Rotating detonation engines (RDEs) are a promising technology for stationary and mobile power generation applications. A form of pressure gain combustion, detonation engines allow for the recovery of the gas pressure lost in traditional constant pressure combustion and the fuel and oxidizer injection schemes. The RDE system is characterized by a highly unsteady flow field, with multiple reflected pressure waves following the strong detonations and the existence of partially-burnt gases entrained within the detonation annulus during the injector recovery process. While experimental efforts have provided macroscopic properties of an RDE with a given fuel-oxidizer mixture and geometry, limited optical access and flow-field diagnostic equipment constrain understanding of the mechanisms that lend to wave stability, controllability, and sustainability. To this end, high-fidelity numerical simulations with detailed chemical kinetics of full-scale RDE systems are performed to provide insight into the detailed detonation physics and anomalous behavior within the system.

3.2 Numerical studies to assess discretization schemes

In determining the relevant discretization and computational models for RDE-type flows, three different aspects need to be tested. First, shock-type discontinuities are captured in Eulerian approaches through the use of dissipative numerics that reduce dispersion errors near the shock-front. In this regard, reducing dissipation while ensuring smooth solutions is important. Second, in turbulent flows, the notion of secondary conservation needs to be considered [20]. Essentially, CFD techniques evolve primary variables such as momentum or velocity. However, due to non-zero discretization errors, the evolution of secondary quantities such as kinetic energy may not be accurate. In other words, if a transport equation for kinetic energy is solved alongside, the solution obtained from this approach and that evaluated using the velocity fields may not agree. In many cases, these differences can lead to suppression of turbulence or numerical instabilities. Hence, minimizing the secondary conservation errors is also important.

Below, two different test cases are conducted, each with a specific goal of assessing the preferred qualities discussed above.

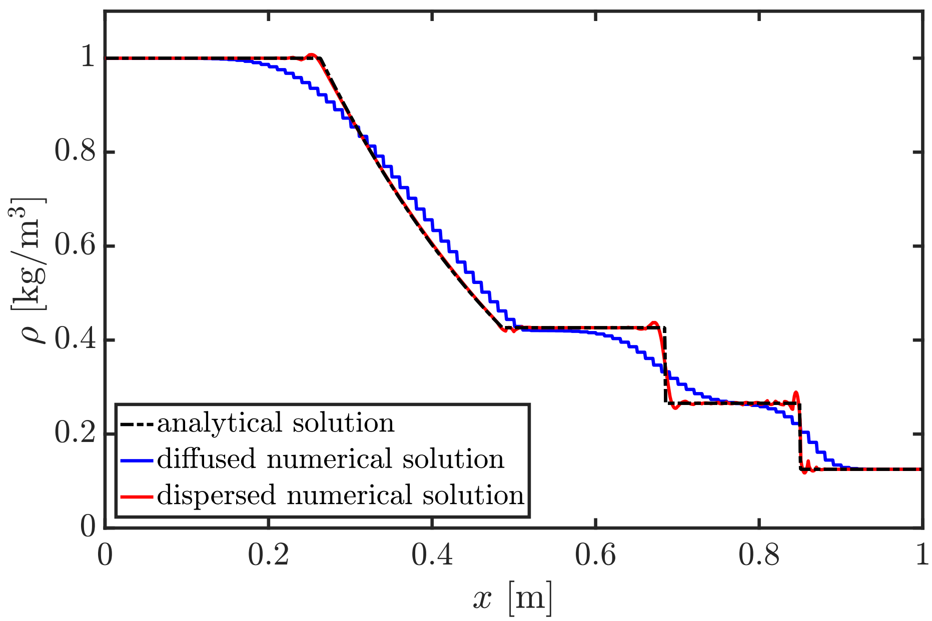

Figure 3.1: Density profile for 1D Sod shock tube at $t = 0.2\,\mathrm{s}$.

3.2.1 One-dimensional Sod Tube Case

The 1D Sod test [21] is a common canonical flow used to study numerical discretization performance. The one-dimensional Euler inviscid equations are solved. For a spatial domain $x \in [0, 1]\,\mathrm{m}$, the density, velocity, and pressure initial conditions, denoted by (ρ_o, u_o, p_o), were taken as

$$(\rho_o, u_o, p_o) \quad = \quad \begin{cases} (1.000,\ 0.0,\ 1.0) & \text{for} \quad x \leq 0.5\,\mathrm{m} \\ (0.125,\ 0.0,\ 0.1) & \text{for} \quad x > 0.5\,\mathrm{m} \end{cases} \tag{3.1}$$

Here, the units of ρ, u, and p are kg/m^3, m/s, and N/m^2, respectively. The analytical solution of this system is defined using the Rankine-Hugoniot shock jump conditions [21]. Figure 3.1 shows the density for $t = 0.2\,\mathrm{s}$, including the analytical solution and two coarse-scale numerical solutions. The diffused solution corresponds to a 0$^{\mathrm{th}}$-order DG simulation, which is equivalent to a FV simulation, and the dispersed solution corresponds to a 2$^{\mathrm{nd}}$-order DG simulation.

The three key features of this system are the leading shock, a contact discontinuity, and a rarefaction wave. In the first numerical solution, these features are diffused, a result of numerical dissipation. In the second numerical solution, the neighborhoods of these features contain spurious oscillations, a result of numerical dispersion. Regardless of the method, FV or DG, the goal is to minimize both diffusion and dispersion of these features.

The convergence of the density profile (see Fig. 3.1) for the several FV and DG schemes were compared. For each scheme, a 3rd-order Runge-Kutta method was employed, and the fluxes were calculated using the HLLC method [22]. The L_1-error was recorded at the end of each simulation based on the average value within each element:

$$\varepsilon = \frac{1}{N}\sum_{j=1}^{N}\left|\overline{\rho}_j - \overline{\rho}_{e,j}\right| \tag{3.2}$$

where ρ_e denotes the analytical density, and $\overline{\rho}_j$ is the average density of element j. Two finite volume schemes were considered: (1) a Godunov scheme, and (2) a MUSCL scheme. The difference between these methods is how the solution at element faces is defined when calculating the flux. For the Godunov scheme, the solution is the same as the cell average, whereas for the MUSCL scheme, the solution at the cell faces is based on a linear extrapolation [23]. For DG, solutions were calculated using 0^{th}, 1^{st}, and 2^{nd}-order polynomial representations. Also, for the $1^{\text{st}}$and 2^{nd}-order representations, both limited and non-limited solutions were considered. That is, in a limited simulation the solution is modified to reduce spurious oscillations. Here, the limiter presented by Cockburn and Shu [24] was implemented.

Figure 3.2 shows the convergence trends for the methods and schemes tested based on the L_1-error as defined in Eq. 3.2 (here, DG-0 refers to 0^{th}-order polynomial basis representation, DG-1 is 1^{st}-order, etc.). The error is plotted versus the degrees of freedom in the simulation N_{dof} as opposed to the number of elements, which gives a better representation of the CPU cost for each method.

Figure 3.2 shows the relative effect of the limiting function in DG simulations. Regardless of the polynomial order or limiting scheme, the solutions converge as $\mathcal{O}(N_{\text{dof}})$ (or 1^{st}-order) because ε is dominated by the errors near the shock and contact discontinuity. For the non-limited methods, large spurious oscillations reduce the global accuracy to 1^{st}-order. For limited methods, the simulation is reduced to a first-order representation at and near discontinuities by construction. So, regardless of the scheme employed, the convergence is limited to 1^{st}-order when capturing discontinuities. Note that for smooth systems, the convergence for each of these schemes follows the expected convergence (i.e., as the polynomial order increases, so to does

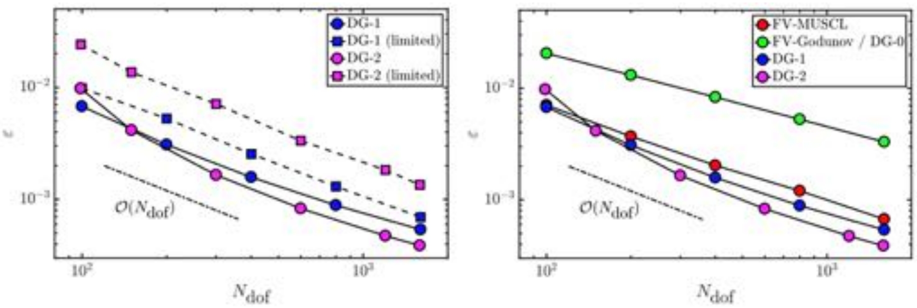

Figure 3.2: Convergence of FV and DG solutions for 1D Sod shock tube.

the convergence rate). However, such convergence is less relevant here as the leading quantity of interest in this work is to accurately capture discontinuities.

Figure 3.2 also shows effect between the FV and DG methods (note that only the non-limited DG schemes are shown). As described in the first section, the errors associated with the base FV method (Godunov scheme) and the 0^{th}-order DG method are the same. Comparing the higher-order methods, the DG methods are slightly more accurate than the ones obtained via the FV-MUSCL method. However, the error remains comparable in magnitude for the DG-1, DG-2, and FV-MUSCL simulations. In fact, the FV-MUSCL scheme yields an error that is very close to that of the DG-1 method. That can be justified by the fact that MUSCL relies on effectively calculating fluxes by reconstructing a piecewise linear solution from average cell values, therefore getting close to the 1^{st}-order polynomial representation of the solution from DG-1. Furthermore, for each simulation, the convergence is limited to $\mathcal{O}(N_{\text{dof}})$ for the same reasons associated with the convergence plot in Fig. 3.2.

To conclude the analysis of these results on the Sod shock tube problem, it is necessary to mention that using the number of cells to evaluate error convergence is not representative of the true computing cost associated with the methods. Indeed, increasing polynomial order also means higher cost, as the number of degrees of freedom of the system is equal to the number of coefficients necessary to describe the piecewise polynomial solution over the whole computational domain. Moreover, the stricter CFL condition associated with DG methods also implies an increase in computational expenses [25]. Therefore, as the polynomial order of the DG increases, not only are the degrees of freedom increased, but also the CFL decreases, resulting in a larger relative CPU cost compared to the FV methods. In summary, the FV methods are able compete with DG methods, at least in shock dominated systems.

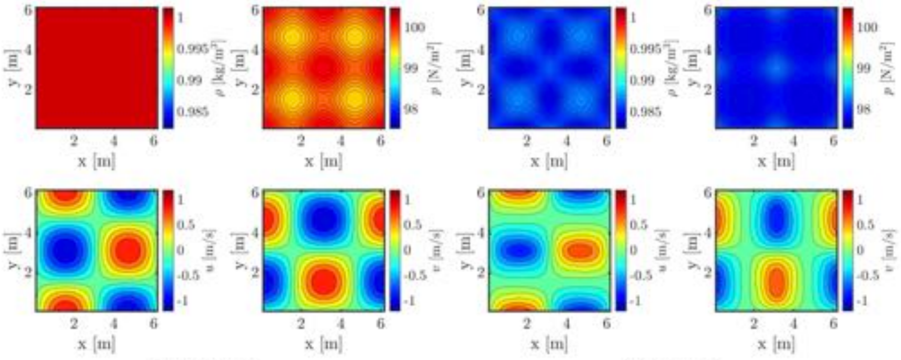

(a) Initial field

(b) Final field

Figure 3.3: Velocity magnitude (a) at $t = 0.1$ s, (b) at $t = 10.0$ s of the constant density Taylor-Green vortex.

The rest of this work will therefore be focused on evaluating FV-MUSCL performance on relevant systems and the effect of AMR on this performance.

3.2.2 Taylor-Green Vortex case

The inviscid Taylor-Green Vortex 2D problem is simulated to assess kinetic energy conservation of the solvers. The initial condition consists of a series of vortices inside a periodic domain. Since the flow is inviscid, the only dissipation effect is due to numerical errors. Initial conditions for this problem have been chosen to match those described by Johnsen *et al.* [26], which were used to study numerical schemes for compressible turbulence. For any TVD solver, numerical diffusion distorts the flow field over time, as shown in Fig. 3.3.

However, minimizing this numerically-induced diffusion is critical for capturing post-detonation cell structures. With this in mind, Fig. 3.4 shows the time evolution of local and initial total kinetic energy ratio for a selection of meshes, including uniform and AMR-based meshes. Analytically, kinetic energy should be invariant with time, but the presence of numerical dissipation leads to a progressive decrease in the domain-integrated kinetic energy.

The three baseline calculations, performed using uniform grids, confirm that decreasing the cell size reduces kinetic energy dissipation. Three AMR calculations are performed, using kinetic energy gradient as a criterion for refinement. The AMR results show an initial fast decay, due to the relatively coarse grid at the start of the

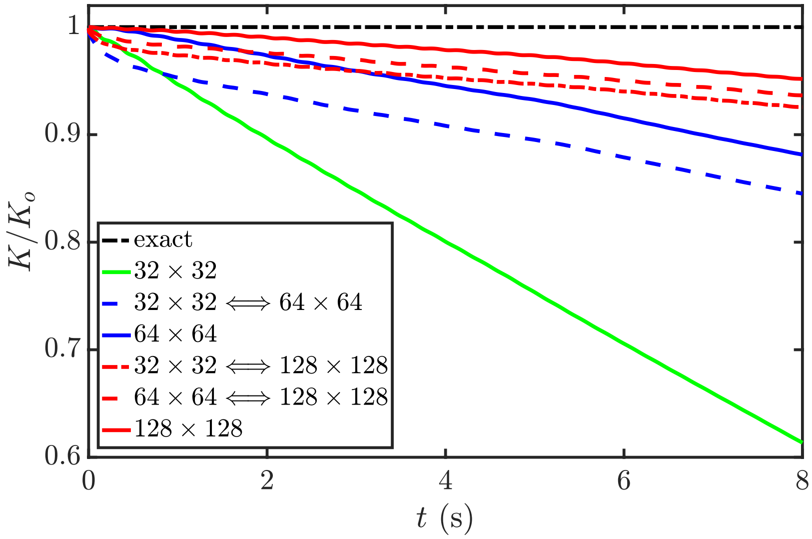

Figure 3.4: Kinetic energy time evolution for varied meshes and refinement strategies.

simulation. However, as more cells are added based on the refinement criteria, the decay rate has the same slope as the corresponding uniform grid solution. However, AMR only added grid points near the features of interest, and will incur a lower overall computational cost due to the reduced number of cells.

3.3 Detonation tube cases

1-D Detonation

The first test case involves a one-dimensional detonation problem conducted in a semi-closed tube, schematically shown in Fig. 3.5. The tube is filled with a premixed hydrogen and air mixture at 1 atm pressure and 300 K initial temperature. A small section at the left end of the tube is filled with a high pressure (27.1 atm), high temperature (3000 K) post-detonation mixture. The detonation wave then propagates towards the right over a distance of 0.3 m. After an initial transient phase, the detonation wave develops into a one-dimensional structure, which should be similar to the ZND theoretical structure. In the past, other techniques such as the conversion

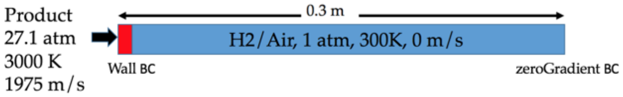

Figure 3.5: 1D DETONATION TUBE CONFIGURATION.

of the governing equations to a set of ordinary differential equations in time has been used to solve this problem [27]. Here, the partial differential equations are directly solved on a set of computational grids.

Figures 3.6 and 3.7 show the pressure and temperature fields after the wave is fully developed. As predicted by the ZND theory, there exists a sharp jump in pressure denoting a shock wave, with a high peak pressure. An equivalent spike in temperature is also observed. After this initial region, expansion of the gases lead to a drop in pressure and temperature from approximately 0.1 m to 0.24 m, where ignition causes consumption of the fuel-air mixture. The species profiles (Fig. 3.8) show a similar structure, where the consumption of the fuel-oxidizer mixture starts around 0.01 cm from the shock location. It is interesting to note that the H and O concentrations remain high at large distances from the shock location, indicating a slow return to equilibrium. This is caused by the expansion of the post-detonation gases that are moving at velocities slower than the wave velocity [leading to a spatially-expanding region of post-detonation products].

To understand the numerical properties of the solver, spatial convergence studies were conducted. Two different quantities of interest were considered: a) the von Neumann pressure, which is the highest pressure obtained in the post-shock region, and b) a numerically extracted Chapman-Jouguet velocity. This latter quantity is obtained as follows. At each time step, the location of 10% pressure rise from the ambient (1 atm) condition is noted. The velocity, the slope of the location versus time curve, is obtained. It was noted that once steady state is reached, this slope remained nearly a constant. Two different sets of simulations were conducted. One set used uniform mesh but with varying grid sizes, while the other uses AMR. In the latter case, the base initial grid is kept the same across the simulations, but the levels of refinement was adjusted in order to obtain progressively finer grid sizes during the course of the simulation. The error is taken as the absolute difference in the quantity of interest between a specific case and the finest resolution case using that solver (AMR or uniform mesh solver). The finest mesh size used for both AMR and

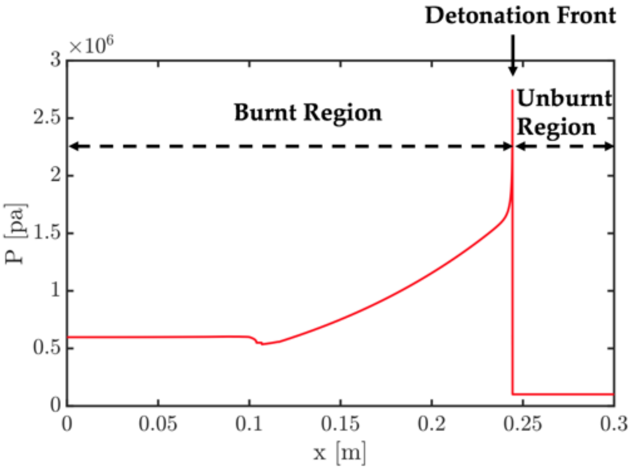

Figure 3.6: PRESSURE PROPERTY AT $P_\infty = 1$ ATM, $T_\infty = 300$ K WITH DETAILED CHEMISTRY.

uniform grid solver is with $\Delta x = 1.25 \times 10^{-5}$ m.

Figures 3.9 and 3.10 show the convergence the two quantities of interest. The pressure convergence follows nearly first-order rate, consistent with the upwinding necessary to stabilize the solver. Interestingly, the AMR solver shows higher errors compared to the uniform grid solver. This trend is more visible in the CJ velocity convergence, where the AMR errors are significantly higher compared to the uniform grid. This can be primarily explained by the nature of the refinement used. The criteria is based on the density gradient, which is maximized near the location of the von Neumann spike. However, the post-shock reaction region is not adequately resolved. This leads to errors in the prediction of ignition, which results in increased overall error in the quantities of interest. Interestingly, even though the AMR refinement criterion is related to the initial density gradient, the lack of accuracy in predicting the reaction zone leads to errors in capturing the von Neumann pressure as well. This provides a cautionary example, where refinement without considering the inherent physics of the problem might lead to loss of accuracy. In the future, other refinement criteria will be tested in order to determine the optimal choice for detonation problems.

In spite of these differences, the use of the AMR approach provides substantial decrease in computational expense. Figure 3.11 shows the variation in the number of

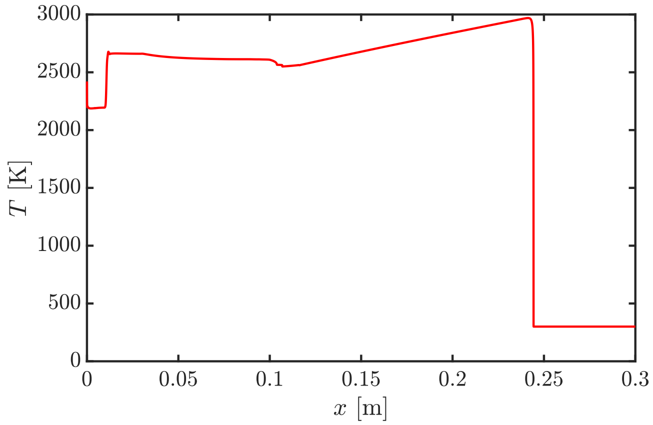

Figure 3.7: TEMPERATURE PROPERTY AT $P_\infty = 1$ ATM, $T_\infty = 300$ K WITH DETAILED CHEMISTRY.

grid points with minimum grid size for the uniform and AMR cases. It is seen that the use of the AMR case provides nearly an order of magnitude advantage for the finest grid sizes. By properly defining the refinement criterion, it will be possible to leverage this speed-up while maintaining computational accuracy.

Although AMR is able to reduce the number of grid points for the required resolution, error convergence does not show significant improvement compared to the uniform grids. Further, the criteria for refinement needs to be analyzed in order to optimize the computational cost of AMR and the achieved reduced error, which will be future work regarding this study. With this mind, uniform grids are utilized in the cases studied below.

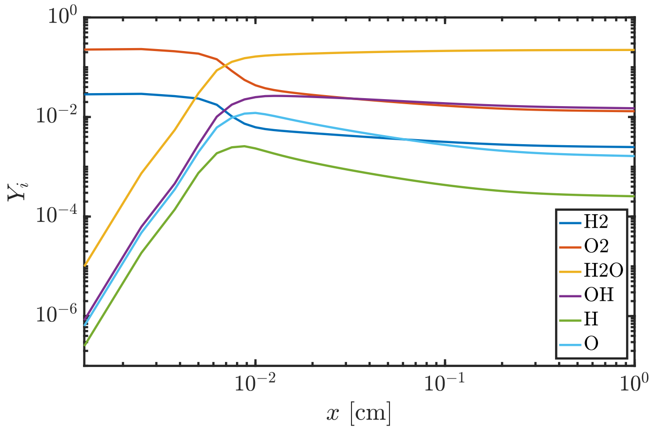

Figure 3.8: SPECIES MASS FRACTION VS. DISTANCE FROM THE SHOCK FRONT.

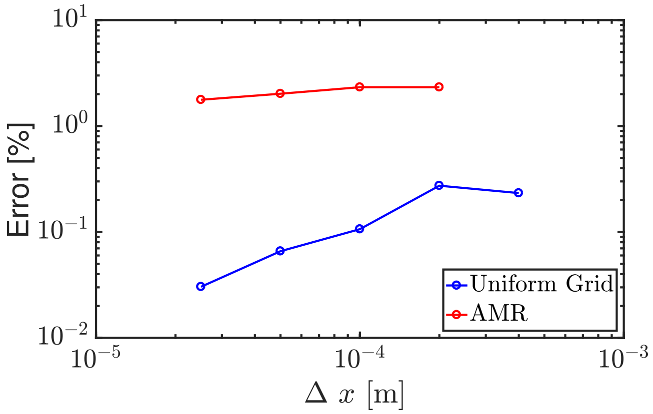

Figure 3.9: ERROR CONVERGENCE FOR CHAPMAN JOUGUET VELOCITY.

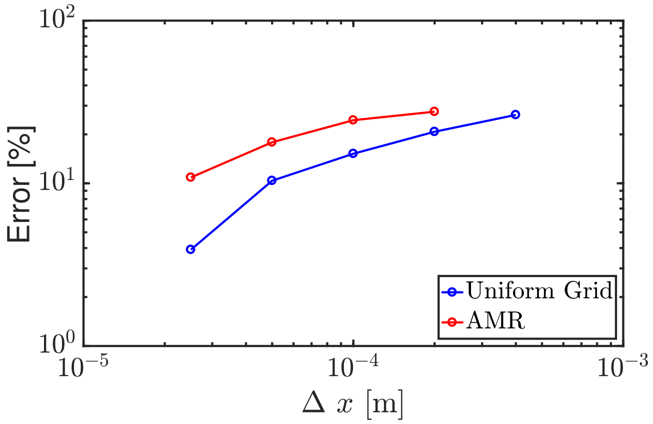

Figure 3.10: ERROR CONVERGENCE FOR VON NEUMANN PRESSURE.

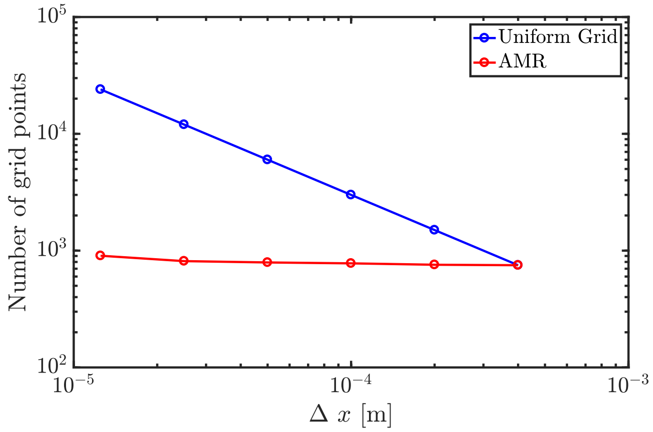

Figure 3.11: COMPARISON OF TOTAL GRID NUMBER BETWEEN UNIFORM GRID AND AMR.

Two-dimensional Detonation in a Wall-bounded Channel

Cellular structures formed by detonations confined to two-dimensional channels have been routinely used to understand detonation structures as well as the rates of chemical reaction. The detonation waves reflect from the channel wall and create local peak pressure points at the detonation front [28, 29, 30]. The trace of the maximum pressure on the wall forms a cellular structure, the size of which could be used to assess the strength of detonation. In particular, smaller cells are associated with highly detonable mixtures.

The simulation configuration is shown in Fig. 3.12. The stoichiometric mixture of hydrogen and air is at a pressure of 1 atm and temperature of 300 K. The domain extends 100 × 2 mm with $dx = 50\mu m$. These simulation conditions have been used to represent prior studies [28]. In order to initiate the transverse wave structure, 3 discrete blocks of 0.15 × 0.5 mm are initialized at a higher temperature, and positioned equidistant from each other in the stream-normal direction at a short distance from the inflow. It is seen that the fully-developed detonation front is formed relatively quickly, and maintains the triple point structure throughout the axial distance. Figure 3.13 shows the evolution of the detonation front, including the high pressure points that are the result of the intersection of transverse waves and the detonation front. These triple points provide the ignition points for the reactive mixture. Figure 3.14 shows the trace of the peak pressure as the detonation front moves through the tube. As expected, the reflection of the triple points due to the bounding walls lead to a cellular structure with highly regular patterns. The size of these cellular structures using the Mueller mechanism are consistent with prior studies utilizing the Jachimowski mechanism [31], as shown in Figure 8 (b) in [28]. This indicates that the current solver is able to reproduce prior data, even with different chemistry mechanism.

Since the simulations are performed using detailed chemistry, it is possible to extract species profiles as the detonation front evolves in space. Figures 3.15 and 3.16 show the evolution of OH and H mass fractions, respectively. Both profiles show complex mixing patterns introduced by instabilities initiated due to the density and pressure gradients across the detonation front. Since the flow is nominally two-dimensional, dissipation of such structures is inherently slow, and may lead to increasingly larger scales as seen in two-dimensional turbulence studies. Since H is produced by the initial dissociation of fuel molecules, it acts as a marker for the chain initiation steps behind the detonation front. It can be seen that H radicals are formed

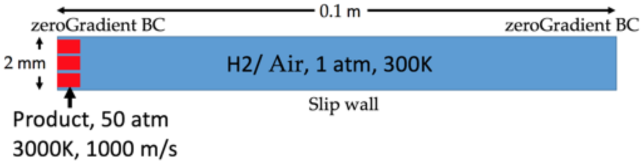

Figure 3.12: 2D DETONATION TUBE CONFIGURATION.

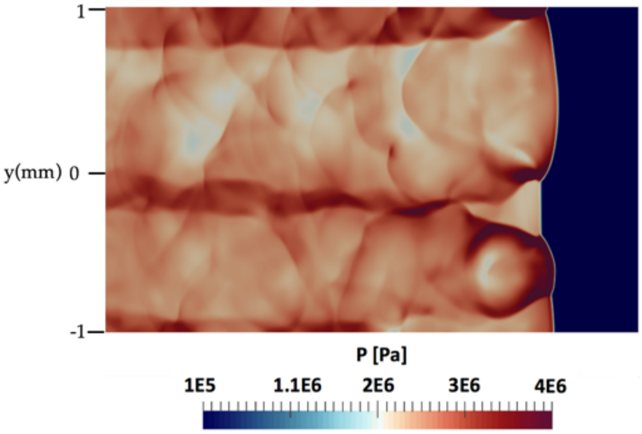

Figure 3.13: TRIPLE POINTS AT THE DETONATION FRONT.

right behind the initial shock, and are consumed over several detonation thicknesses, leading to nearly zero mass fractions at a sufficient distance from the front. OH formation also happens immediately behind the shock, but its complete consumption is delayed due to significant OH concentrations at large distances from the front.

An alternative view of the detonation structure is to observe the evolution of the scalars in composition space [32, 33, 34], which provides information on the inner structure of the detonation processes. Figures 3.17 and 3.18 show OH and H_2O concentrations plotted against temperature. In typical one-dimensional laminar flames, there will be a monotonic relation between these quantities, since temperature increase is directly related to the consumption of H radicals and the generation of OH free radicals. Even in two-dimensional detonations, which are canonical flows compared to practical applications, this structure between temperature and mass fractions is highly complex. It is seen that the increase in OH and H occur at different temperature levels between 1500 and 1800 K. This is due to the fact that the detonation front that passes the fresh gas does not have uniform properties but contains triple points

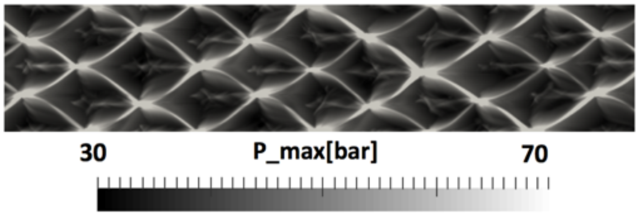

Figure 3.14: CELLULAR STRUCTURE VISUALIZED BY TIME HISTORY OF THE LOCAL MAXIMUM PRESSURE.

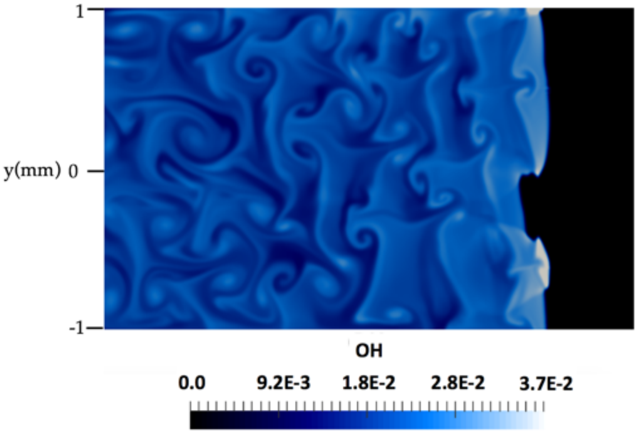

Figure 3.15: OH PROPERTY BEHIND THE DETONATION.

as well as interacting transverse waves. Consequently, different parts of the domain experience different detonation front properties, which is reflected in this scatter plot. Furthermore, it is seen that at relatively high temperatures, there is a sudden drop in OH concentrations and a corresponding increase in H_2O concentrations, which is linked to the final oxidation process that terminates the combustion reactions.

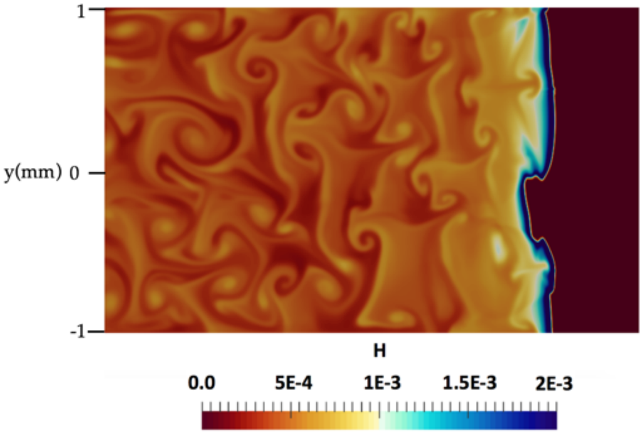

Figure 3.16: H PROPERTY BEHIND THE DETONATION.

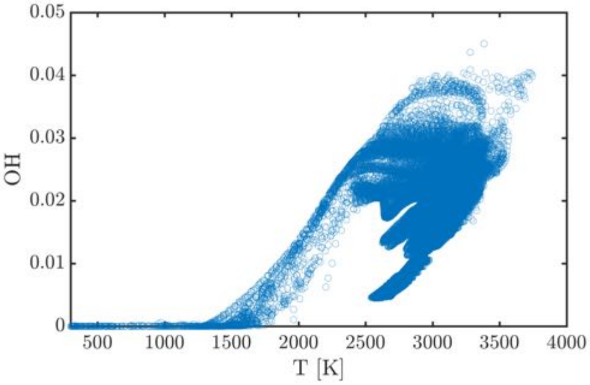

Figure 3.17: SCATTER PLOT OH VS. T.

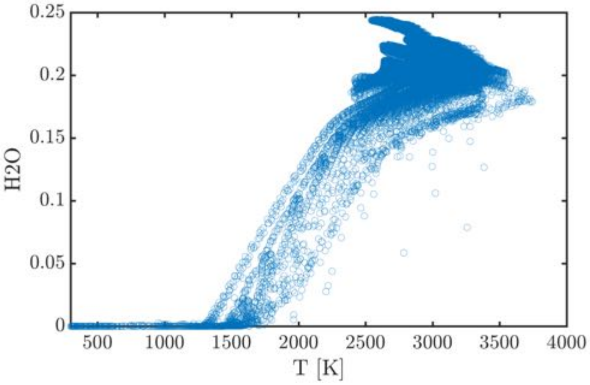

Figure 3.18: SCATTER PLOT H_2O VS. T.

3.4 Full scale RDE simulation with hydrogen/air chemistry

3.4.1 RDE configuration and numerical details

The RDE configuration considered in this work is the axial air injection system [35], shown schematically in Fig. 3.19. Fuel is injected using $n = 120$ discrete ports positioned at an angle to the oxidizer stream. For the case simulated, the air mass flow rate is 404.2 g/s, with a global equivalence ratio of 1.01. In the experiment, the detonation chamber exhausts to a larger plenum. In the simulations, this plenum exit (outflow plane) is assumed to be at atmospheric conditions. The flow is subsonic in this region.

The simulations use the UMdetFOAM solver developed for handling complex geometries using detailed chemical kinetics [36, 37]. The compressible formulation solves Navier-Stokes equations along with continuity, energy and species transport equations. The chemical source terms, transport, and thermochemical properties are obtained by coupling the OpenFOAM framework with CANTERA [38]. In this study, a hydrogen/air mechanism with 9 species and 19 reactions is used [39]. The convection terms are discretized using the MUSCL-based HLLC scheme. A second-order Runge-Kutta scheme is used for advancing in time [22]. The diffusion terms are discretized using the Kurganov, Noelle and Petrova (KNP) method [40]. The solver has been extensively validated in the past, specifically for detonation applications [36, 37]. MPI-based domain decomposition is used on roughly 4000 cores.

The simulation domain is shown in Fig. 3.19. Grid points are clustered in the near-injector region to fully resolve fuel-air mixing. The mesh size is approximately 10^{-4}m in the injector region, and 2×10^{-4}m in the region up to 0.4m in the axial direction. A total of 25×10^{6} control volumes are present in the entire domain. For convergence tests, simulations with 2 and 3 times the control volumes of this baseline grid were carried out, but no significant differences in results were seen. In order to collect long term statistics needed for the analysis below, the baseline grid was used. For comparison, these resolutions are similar or finer than other full system RDE simulations [41, 42]. The results show that the detonation front is resolved by 10-20 cells in the shock-normal direction. It will also be seen that the reaction zone is distributed along the circumference, similar to prior linear model results [43].

The inflow is described using a constant mass flow rate, with the fluid properties interpolated from within the fluid domain. Adiabatic walls (zero-gradient in temper-

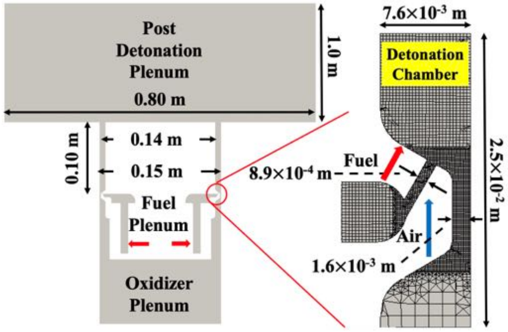

Figure 3.19: (Left) Computational geometry; (Right) Details of the fuel injector and air inlet along with computational mesh.

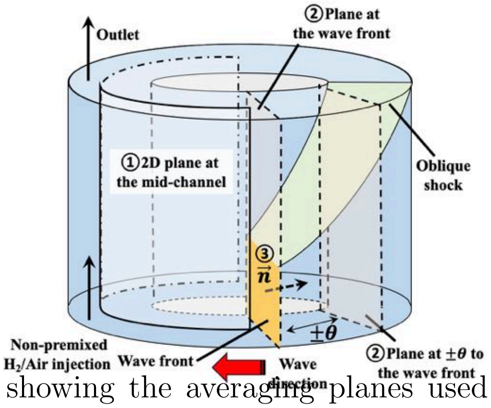

Figure 3.20: Schematic showing the averaging planes used for the analysis in this work.

ature) along with no-slip wall boundary conditions are used. The simulation is first run for 15 cycles to ensure statistical stationarity, after which data is collected for 10 cycles. The analysis is based on different types of averaging (Fig. 3.20). For these analyses, the wave front is defined by the location of maximum pressure gradient.

3.4.2 Structure of RDE flow

Figure 3.21 shows the mid-plane of the annulus unwrapped as a two-dimensional field (① in Fig. 3.20); the images show LIF signal strengths scaled relative to the 98th percentile values of the respective datasets. Compared to ideal two-dimensional simulations [44], the three-dimensional discrete injection results show a much richer flow

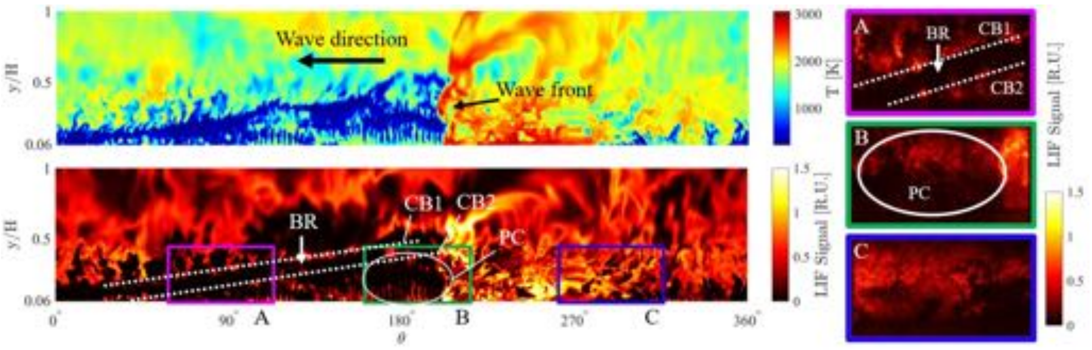

Figure 3.21: (Left) RDE temperature field and numerical synthetic OH-PLIF computed using a two-level model [48] shown as an unwrapped 2D image. Right: OH-PLIF images obtained from experiment, reproduced from [45].

structure characterized by multiple regions where combustion occurs. The notation followed here is similar to that of Chacon et al. [45, 46]. The wavefront is highly corrugated, which is a result of the turbulence and highly non-uniform fuel-air mixture that is being processed by the wave. This leads to substantial local variations in wave velocity [43, 47], including post-detonation pressures and temperatures.

The reacting flowfield predicted by the computations is qualitatively similar to what was observed experimentally. As observed in experiments in this configuration [46, 45], the fuel-air mixture begins burning at various locations upstream of the detonation wave, an effect that has been termed *parasitic combustion* [46]. This includes a first contact burning region (CB1) at the contact surface between unburnt and burnt gases from the previous cycle, and a second contact burning region (CB2) close to injection where the second deflagration zone is observed. This second region is likely supported by the injector design where flow recirculation around the injectors entrain burnt gases and fuel, leading to rich mixtures in a radical pool that facilitates stabilization (flameholding) of parasitic combustion.

The CB1 and CB2 regions have slightly differing slopes and are separated by a buffer region (BR). The width of the buffer region depends on the relative response time of the injectors, especially the oxidizer injector. The overall effect of these contact burning regions is to partially consume the mixture ahead of the wave through what collectively is referred to as parasitic combustion (PC) [45]. The first order effect is to weaken the detonation wave (lower speed and pressure rise) [46]. These effects are accentuated by the details of the injection process and thus emphasizes its importance.

3.4.3 Injection dynamics and wave-relative structure

One of the unique features of RDEs is the time-varying injection of fuel and oxidizer. The high pressure in the post-detonation region blocks or unchokes the flow, leading to a finite recovery time. Figure 3.22 shows the average injection plane velocity for the fuel and oxidizer inlets as a function of cycle-normalized time (i.e., the time taken for the detonation wave to complete one cycle). It is seen that both injectors are nearly blocked as the detonation wave passes (at $\bar{t} \approx 0.4$), and take nearly the rest of the cycle time to reach the steady flow. Since the mass flow rate upstream is fixed, this temporary blocking of certain injectors close to the wave pressurizes the fluid in the plenum, and redirects the flow towards unblocked injectors. The fuel injector is generally more stiff, and relaxes to the full flow faster compared to the oxidizer. This in turns creates local variations in equivalence ratio as a function of cycle time.

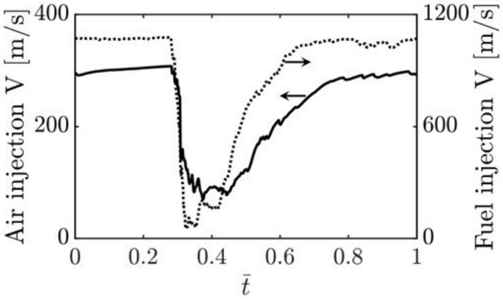

Figure 3.22: Variation in injection velocity with cycle-averaged time for oxidizer and fuel inlets.

The fuel distribution is analyzed in Fig. 3.23, which shows the phase-averaged mixture fraction distribution in the domain. For this purpose, the detonation wave was defined as the location of maximum pressure gradient along a plane aligned with the axial direction. Then, data slices at angular increments of 15° were averaged to obtain the phase-averaged data (② in Fig. 3.20). Since the fuel ports are discrete, the wave might be located at several instances in between injectors. It is seen that 15° ahead of the wave, the fuel jet is well-developed, and penetrates far downstream. The equivalence ratio in the core of the jet is roughly 5. It is also seen that pockets of rich mixture exist further downstream, roughly at the height where the PC region is found. At the wave front, the sudden pressure rise reduces jet penetration. Further, 30° degrees behind the wave, the jet length remains short, which is consistent with the recovery times seen in Fig. 3.22. In spite of these variations, the peak mixture fraction drops from 1 to roughly 0.1 quickly shows fast but incomplete mixing.

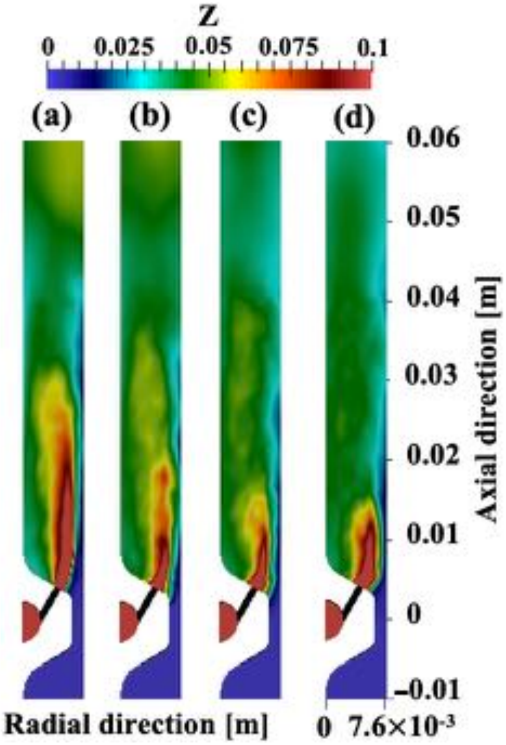

Figure 3.23: Phase-averaged mixture fraction plotted at a) 15° ahead the wave front, b) the wave front, c) 15° behind the wave front, d) 30° behind the wave front.

Figure 3.24 shows the pressure and temperature averaged at the wave front over the entire simulation time (② in Fig. 3.20). The temperature field shows considerable asymmetry, with peak temperatures found close to the inner wall. As described earlier, the deflagration below CB2 is caused by recirculation of the fuel-air mixture in this region between the fuel jets and the inner wall. This causes sustained high temperature in this region, which is further increased by the passing detonation wave through compression. The pressure field shows much more symmetry except for a small region of high pressure near the outer wall. This result seems counter-intuitive given the fuel distribution shown in Fig. 3.23. The peak pressure in the simulations is substantially lower than the ideal detonation cases. This is indicative not only of the losses due to parasitic combustion, but also the large variations in the detonation structure with time. This inhomogeneity is a result of temporal variations in the shock front, including its sensitivity to the fuel-air stratification and parasitic combustion. As a result, this homogeneity is feasible on an average, but considerable instantaneous fluctuations about the mean exist.

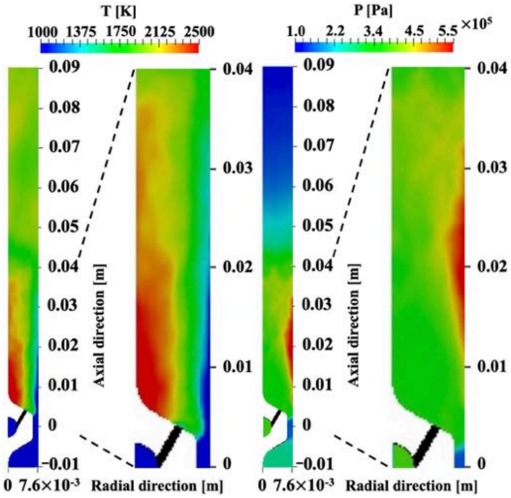

Figure 3.24: Phase-averaged (left) temperature and (right) pressure field at the detonation front.

3.4.4 Statistical Features of Detonation Process

In order to understand the overall structure in composition space, unconditional time averages at steady-state conditions are presented. Figure 3.25 shows comparison of experimental data with simulation results for the axial variation of normalized pressure, where the normalization factor is the plenum pressure. It is seen that the simulations predict the decay in pressure across the plenum throat and in the near-field of the injection plane. The simulations predict a stronger detonation wave, which is also reflected in the faster wave speed of 1804 m/s as compared to 1566 m/s in the experiments. But overall, the continued drop in pressure beyond the detonation region is also captured in the simulations.

Figures 3.26 and 3.27 show one-dimensional profiles across the shock (based on ③ in Fig. 3.20). At the detonation front, H_2O mass fraction is already high, indicating

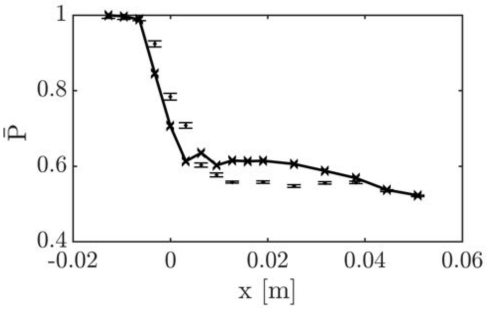

Figure 3.25: Comparison of pressure measurement on the chamber wall with time-averaged simulation data. The simulation and the experiment pressures are normalized by 254 kPa and 296 kPa, respectively. The circle symbol denotes the experimental data and the cross symbol with line denotes the simulation results.

residual gases from the previous cycle are present in the mixture. It is also seen that the pressure profile shows an inflection point around 4×10^{-4}m, which corresponds to the start of the oxidation process. Hence, the region of gradual O_2 consumption can be considered as the induction zone. The reactions occur over an appreciable length. This further indicates that the fluid reaches chemical equilibrium over timescales comparable to the induction time and is not a jump process. The temperature profile shows a more gradual increase due to the distributed heat release caused by the parasitic combustion and the extended reaction zone behind the shock front. The heat release plot shows that the presence of burnt gases causes sustained heat release behind the shock wave, but the peak exothermicity is reached when fresh gases react past the induction zone.

3.4.5 Detonation structure in composition space

Conditional averages of key quantities such as temperature and species mass fractions conditioned on mixture-fraction provide insight into the reaction structure of flames. Figure 3.28 shows the conditional average of temperature at three different locations (at the wave, ±12.5° from the wave) (② in Fig. 3.20). The averages are obtained over the entire plane shown in Fig. 3.24. It is seen that ahead of the wave, there is already significant heat release leading to a higher temperature than the plenum value of 300 K. The near-stoichiometric value is slightly higher than 1000K, which is higher than the temperature needed for chain branching reactions to be dominant

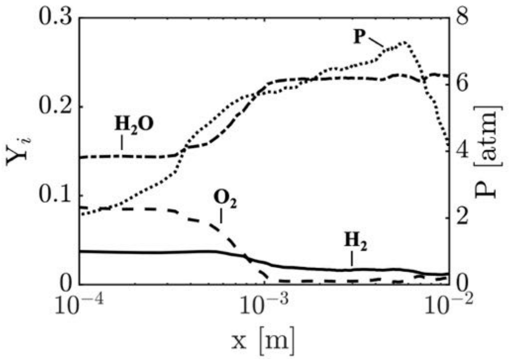

Figure 3.26: One-dimensional shock-normal averaged species and pressure profile. $x = 0$ indicates shock location. The data is obtained at mid-channel 2 cm from the center of the air inlet throat.

for hydrogen-air chemistry. As a result, the mixture that is being processed by the wave is highly reactive and the conditional averages at and behind the wave are nearly the same. It should be noted that the peak in temperature is at slightly richer mixture fraction values than stoichiometric, which is consistent with the observation that the highest detonation velocities occur for richer mixtures. Figure 3.29 shows the conditional species profiles for the reactants. It is seen that at the wave and behind the wave, there is non-zero oxygen concentration on the rich side, indicating some leakage due to inefficiencies in the mixing process. Ahead of the wave, there is already significant consumption of the fuel and oxidizer, leading to the higher temperatures in the CB1/CB2 region.

Figure 3.30 shows the conditional heat release average. Overall, heat release rates do not show the same structure as the other species profiles discussed above. Instead, much of the heat release is on the lean side, and is significantly higher at the detonation front compared to either ahead or behind the wave. Note that the one-dimensional shock profile shown in Fig. 3.27 covers roughly 2° in azumithal angle. This is an indication that although the reaction structure is quite distributed, the non-ideal detonation wave could be compared to a thickened flame front. Heat release after the wave is confined to a narrow region but it is much more spatially distributed before the wave. This feature has been observed in linear detonation models as well [43, 49].

Figures 3.31 show the conditional fluctuations of temperature. First, it is seen

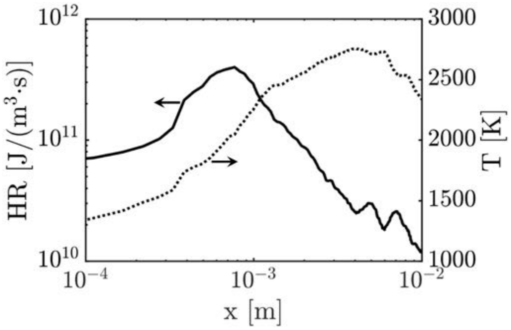

Figure 3.27: One-dimensional shock-normal averaged heat release rate and temperature profile. $x = 0$ indicates shock location. The data is obtained at the mid-channel 2 cm from the center of the air inlet throat.

that the conditional deviation is quite high, often comparable to the mean values themselves. This indicates strong bi-modal behavior, with intermittent regions of high products and reactants at all locations. The conditional variance of reactants reveals that the near-stoichiometric region has lower fluctuations compared to the region of high heat release on the lean side. Moreover, there is considerable variation at rich conditions, where there is still significant fuel left after the detonation wave. These regions correspond to downstream locations (> 0.03m in Fig. 3.23).

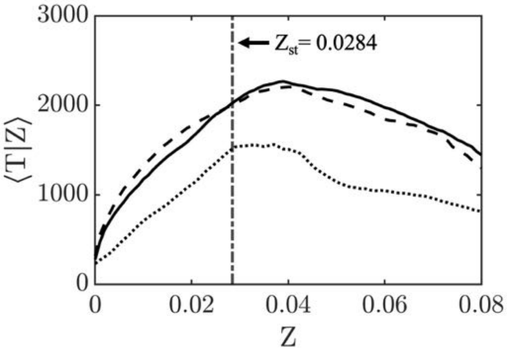

Figure 3.28: Conditional temperature (K) averaged conditioned on mixture fraction. The solid line, dashed line, and dotted line show the wave front, 12.5° behind of the wave front, and 12.5° ahead of the wave front, respectively.

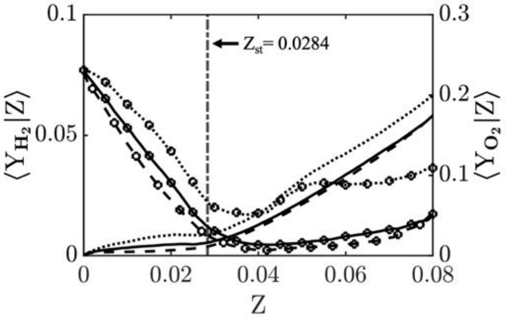

Figure 3.29: Conditionally average species mass fraction conditioned on mixture fraction. The solid line, dashed line, and dotted line show the wave front, 12.5° behind of the wave front, and 12.5° ahead of the wave front, respectively. (Line without markers:⟨Y_{H_2}|Z⟩, line with markers:⟨Y_{O_2}|Z⟩)

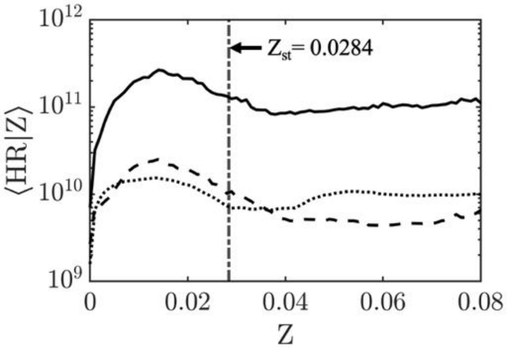

Figure 3.30: Conditionally average heat release (J/(m^3·s)) conditioned on mixture fraction. The solid line, dashed line, and dotted line show the wave front, 12.5° behind of the wave front, and 12.5° ahead of the wave front, respectively.

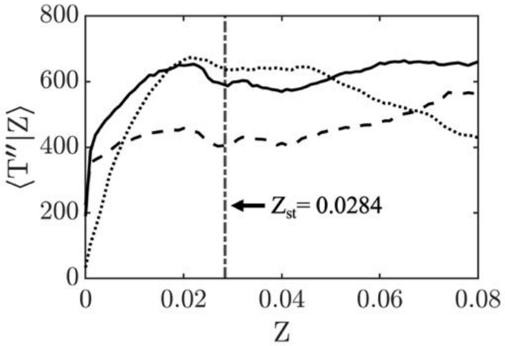

Figure 3.31: Conditional standard deviation of temperature (K) conditioned on mixture fraction. The solid line, dashed line, and dotted line show the wave front, 12.5° behind of the wave front, and 12.5° ahead of the wave front, respectively.

3.5 Full system RDE simulations with ethylene/air chemistry

3.5.1 Simulation configuration

The RDE configuration simulated here is based on the AFRL design used in [50]. This design is similar to the hydrogen/air RDEs used in other related studies [51], but has a larger annulus width to account for the slower ethylene/air chemistry. The wider channel width allows for the triple points to stabilize, which is reflected in the larger cell size for more complex hydrocarbons. Due to this change, the fuel-air mixing is different compared to the hydrogen-based RDE. Figure 3.32 shows a schematic of this geometry. The channel width is 22.86 mm, and the area ratio between the oxidizer inlet and the detonation chamber is 0.059 [50]. The air injection slot is 1.778 mm wide. The oxidizer stream and the fuel stream vertically intersect at the bottom of the chamber.

Several different simulations are conducted here, including the dilution of the fuel with hydrogen gas to study its impact. A list of simulations is provided in Tab. 3.1. The air mass flow rate is set to 0.7 kg/s for the pure ethylene fuel cases. The total temperature in the air plenum is varied between 300 K-600 K. $T_0 = 300$ K is used for the fuel plenum in every case. The back pressure is 1 atm and 2 atm for the pure ethylene and ethylene with hydrogen addition cases, respectively. The increase in back pressure for the ethylene with hydrogen addition case increases the baseline pressure in the detonation chamber, thereby increasing the detonability of the mixture. The total pressure in the each plenum is computed by the choke relation as follows,

$$P_0 = \frac{\dot{m}}{A}\left(1 + \frac{1}{2}(\gamma - 1)\right)^{\frac{\gamma+1}{2(\gamma-1)}} \sqrt{\frac{RT_0}{\gamma}} \tag{3.3}$$

where A is the area, R is the gas constant of each stream, γ is the specific heat ratio, and $\dot{m}$ is the target mass flow rate. When the total temperature of the oxidizer plenum is changed, it affects the total pressure and the post-throat conditions. As a result, the velocity and mixing fields inside the detonation chamber are altered, even for the same mass flow rates. For this reason, changing the total temperature will lead to variations in the combustor behavior that could help understand the detonation features.

To obtain performance related metrics for the RDE, the mass flow rate is computed as

$$\dot{m} = \int_{inlet} \rho u dA_{inj}, \tag{3.4}$$

The net force is obtained as

$$F = \int_{exit} \rho u^2 + (p - p_{back}) dA_{exit}, \tag{3.5}$$

where p_{back} is the imposed back pressure, and u indicates the face-normal velocity. Based on these quantities, the specific impulse is computed as

$$I_{sp} = \frac{F}{\dot{m}_{fuel} g}, \tag{3.6}$$

where g is the gravitational acceleration and $\dot{m}_{fuel}$ is the mass of fuel in a total flow rate of $\dot{m}$.

Composition	P^0_{oxi} [kPa]	P^0_{fuel} [kPa]	T^0_{oxi} [K]	T^0_{fuel} [K]	$\dot{m}_{air}$ [kg/s]	P_{back} [atm]	$W_{Sim.}$ [m/s]	$W_{Expt.}$ [m/s]	$W_{Th.}$ [m/s]	I_{sp} [s]
C_2H_4/Air	441	292	300	300	0.7	1	1070	1020	1824	1936
C_2H_4/Air	509	292	400	300	0.7	1	1171	—	1814	2122
C_2H_4/Air	623	292	600	300	0.7	1	—	—	1797	1783
C_2H_4:H_2(50:50)/Air	441	420	300	300	0.7	2	1328	—	1857	2271

Table 3.1: Test case description as well as summary of macroscopic results from the simulations.

A baseline computational grid is generated with the minimum grid spacing of 3 $\times 10^{-4}$ m. This mesh spacing is similar to other related studies [52, 36]. The mesh near the injection system is shown in Fig. 3.32. The total number of computational volumes is about 30 million cells. In this study, heat transfer to the walls is not considered, primarily because the total run time will not allow any meaningful steady state to be reached. Due to the supersonic flow in the domain caused by detonation waves and the short operation time of RDEs (approximately a few seconds), the heat transfer to the wall is neglected in this study. With the similar reason, the slip wall boundary condition is used for the following simulations.

The simulations are performed as follows. Starting with a uniform flow field, the fuel and oxidizer jets are allowed to evolve in the domain without any chemical reactions. Once this development is complete and fully-choked conditions are established

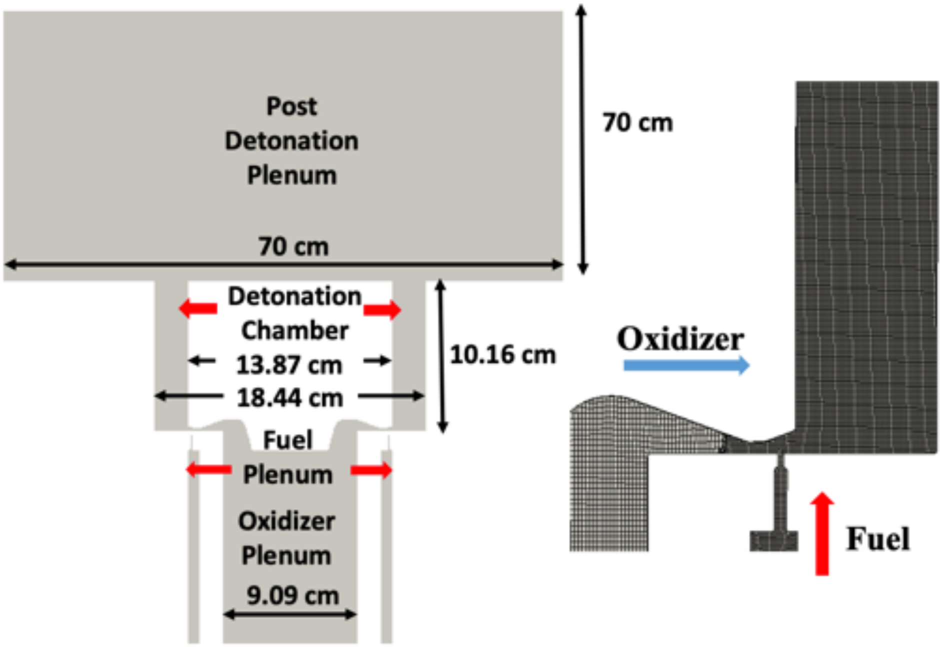

Figure 3.32: Left: computational geometry and RDE configuration with dimensions. Right: the fuel and oxidizer injection scheme with computational mesh.

for both sets of injectors, a high temperature region is patched within the annulus with gas conditions replicating the one-dimensional post-detonation values (obtained from 1D simulation data). This flow is allowed to evolve for sufficient time until a statistically stationary detonation field is observed. Note that the time required to reach this state is highly dependent on the flow and initial conditions. After reaching this stationary state, the simulation is continued and data is collected for evaluating statistics such as wave velocity or shock structure. The total simulation time for this phase is equivalent to roughly 4-5 cycle periods after reaching steady state operation. In the discussions below, only results from this phase will be presented.

3.5.2 Pure ethylene cases

The case of the pure ethylene without hydrogen dilution is discussed first since a) it serves as a baseline for the discussion about the ethylene and hydrogen case, and b) the experimental data of the wave speed is available to validate the computed result.

Figures 3.33, 3.34 and 3.35 show the general behavior of RDEs for different inflow temperatures. The wave front is denoted in a red box in each figure. While the 300 K and 400 K air cases reveal a visible wave front, it is indistinct for the 600 K air case. The high temperature region behind the wave front indicates that the wave is sustained due to the chemical reaction for the lower inlet temperature cases. Interestingly, the high pressure region appears farther downstream of the lower wall for the 300 K case compared to the 400 K case. This observation is also reported in the experiment, where the wave front is offset from the base [50].

The equivalence ratio distributions show interesting trends. In the lowest temperature (300 K) and highest temperature (600 K) cases, the fuel is reasonably well mixed across the channel width, with near stoichiometric conditions. On the other hand, the 400 K simulation shows larger variations near the outer wall of the chamber. While these are instantaneous snapshots, this non-mixedness was observed at many time instances, indicating a difference in the mixing behavior of these systems. Moreover, all cases show significant fluctuation in the temperature field across the detonation cross-section, indicating a highly non-uniform detonation process. For instance, the wave appears weaker near the mid-channel while the temperature fields show a clear post-detonation condition at this location. This indicates that the wave is undergoing some radial motion, akin to slapping modes, which sets up a radial entrainment process locally.

Figure 3.36 and 3.37 show the species and pressure behavior plotted as a function of distance from the shock front for the 300 K and 400 K air cases. Profiles are extracted along the circumference at mid-channel distance and outer wall at 5 mm from the chamber bottom. Since the wave structure is highly three dimensional and unsteady, six different snapshots are processed to obtain the averaged profiles. Compared to the 1D profile, the peak pressure drops significantly for the full system simulation, which is about 60% of the ideal case. It is also seen that the pre-detonation pressure is almost 1 atm and close to the exit backpressure. The oxidization process at the mid-channel is much slower and the peak pressure is lower compared to values at the outer wall. Furthermore, there is residual product gases from the previous cycle mixed with fresh gases, leading to partial combustion before the wave arrives. This parasitic combustion is one of the reasons for the weak detonation observed here. In fact, the computed wave speed is almost 60% of the CJ velocity as tabulated in the Table 3.1. This low wave speed is also observed in the experiment [50].

Figures 3.38 and 3.39 show the temperature and pressure as a function of distance from the shock front for the 300 K and 400 K cases. As observed in the contour images

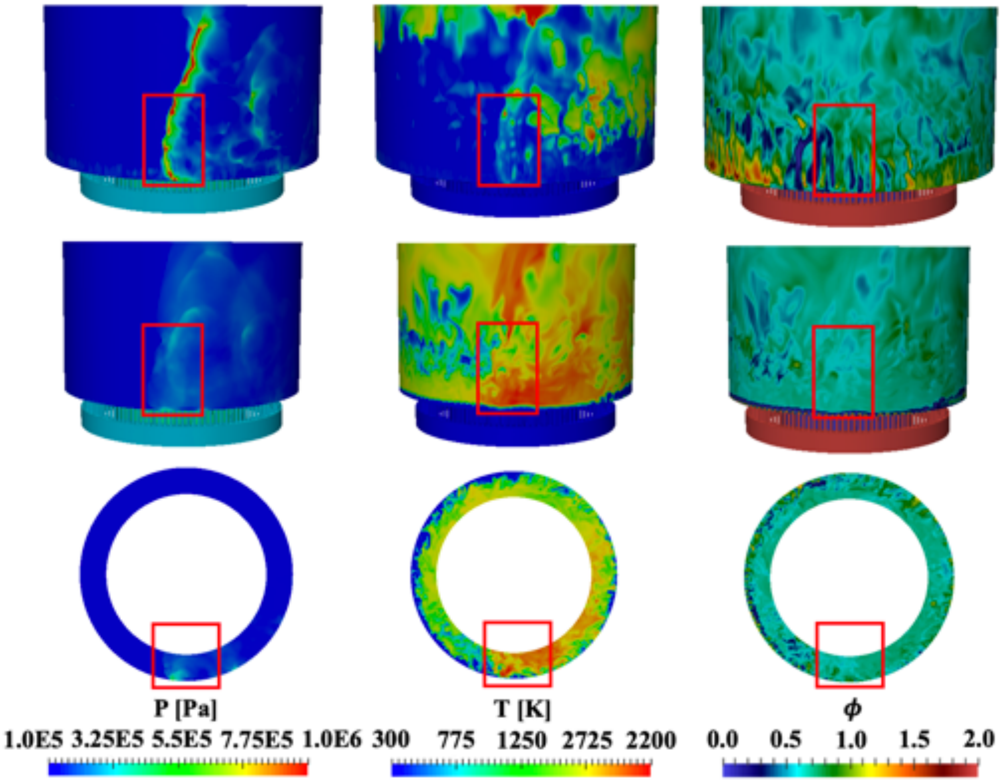

Figure 3.33: Pressure, temperature, and equivalence ratio fields for $T^0_{oxi} = 300$ K. Top: outer wall. Middle: mid-channel. Bottom: cutting plane 2 cm from the chamber bottom.

(Fig. 3.33), the 300 K case has higher temperatures near the mid-channel compared to the outer wall. In fact, the post-wave increase in temperature is extremely weak. On the other hand, the 400 K case shows higher temperature near the outer wall, and comparable profiles near the mid-channel. In both cases, the temperature is higher near the mid-channel and is sustained for longer distances behind the shock, compared to the outer wall profiles. This is possibly due to larger fluctuations in equivalence ratio near the outer wall. Note that the peak value of the 400 K air case (1800 K) is still much lower than the CJ state value (approximately 2800 K). The 300 K air case does not show a similar increase in temperature because the profile is an averaged profile. In other words, the reaction is not continuously sustained behind

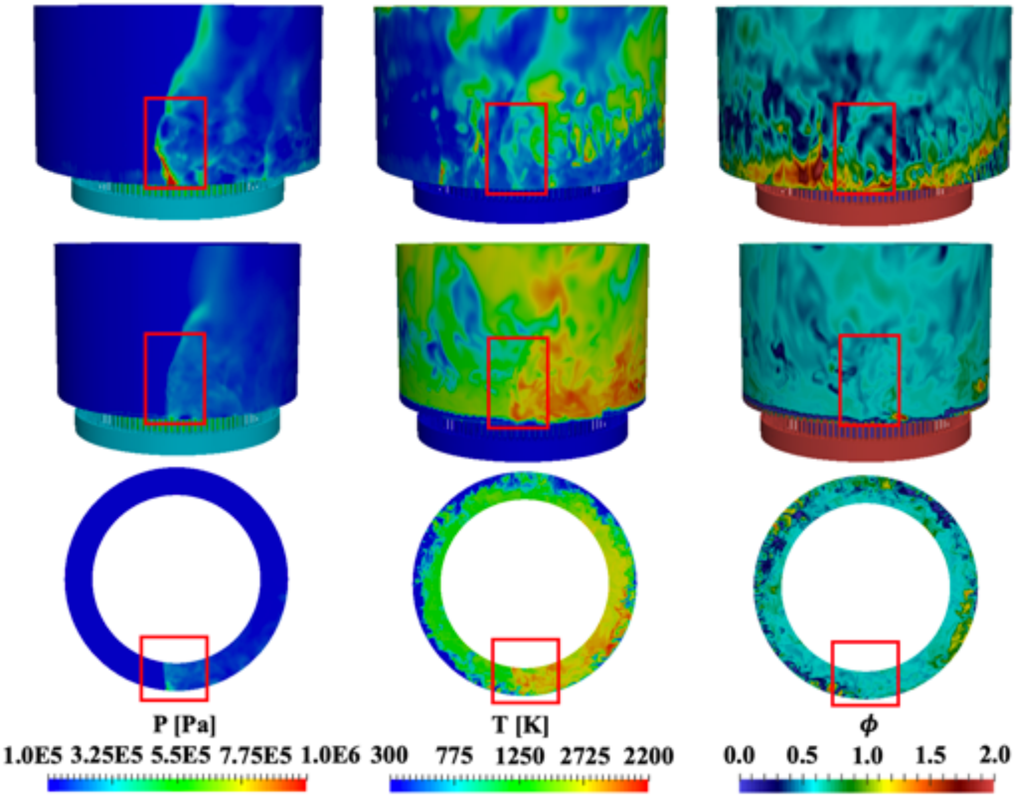

Figure 3.34: Pressure, temperature, and equivalence ratio fields for $T^0_{oxi} = 400$ K. Top: outer wall. Middle: mid-channel. Bottom: cutting plane 2 cm from the chamber bottom.

the shock at a height 3 mm from the base of the chamber for the 300 K air case unlike for the 400 K air case. This is also due to dependency of the mixing process on the air temperature, which will be discussed later. At the the mid-channel, both cases exhibit almost flat temperature profiles along with a smooth pressure rise. This indicates that the reaction happens in the broad region behind the shock (or a strong pressure wave) without a Von Neumann spike as seen in a one-dimensional detonation structure or in practical pulse detonation devices [53].

To understand the source of this incomplete detonation process, it is useful to analyze the mixing process near the fuel-air injection region. Figure 3.40 shows the time sequence of equivalence ratio for all three cases. The time shifts from the left

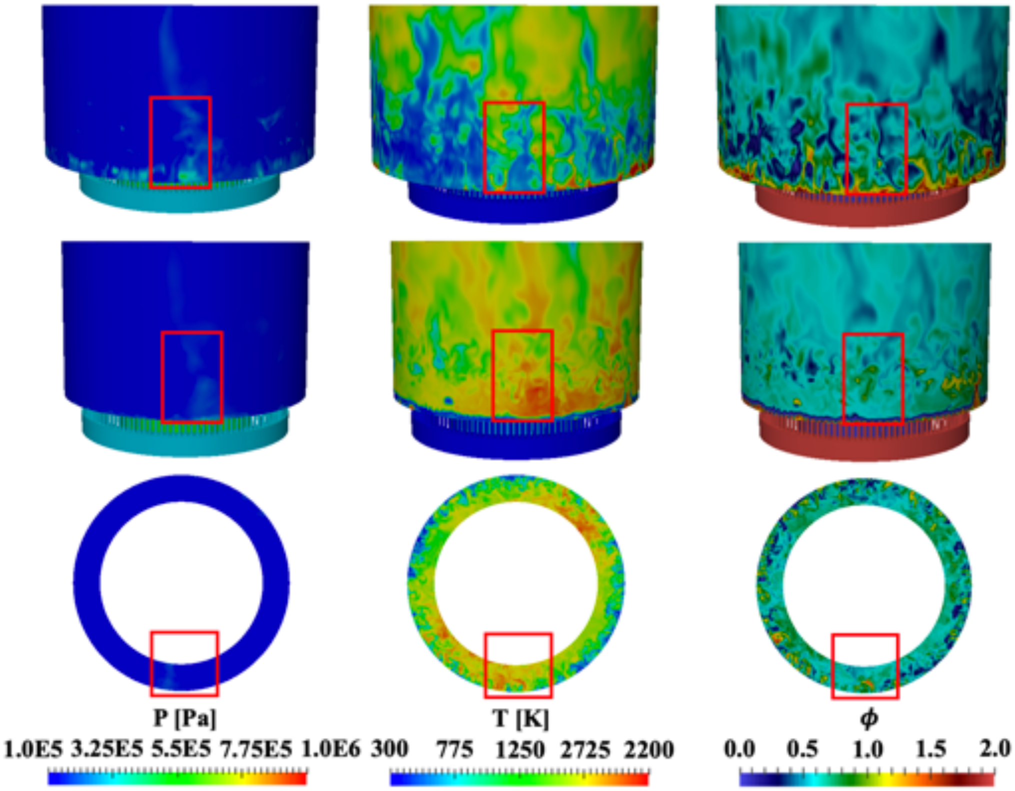

Figure 3.35: Pressure, temperature, and equivalence ratio fields for $T^0_{oxi} = 600$K. Top: outer wall. Middle row: mid-channel. Bottom: cutting plane 2 cm from the chamber bottom.

figure to the right figure by 40 μs between each frame. Since the mass flow rate is identical for all cases but the inflow density changes, the velocities of the fuel and air streams are different. This creates a difference in the mixing process among the different cases. The 300 K case shows that leaner mixtures form in the lower part of the domain, leading to near stoichiometric values further downstream. Further, the oxidizer stream enters the chamber along the bottom wall and creates a recirculation region supported by the inner chamber wall. Recalling that the detonation wave is weaker near the bottom of the domain for this case (Fig. 3.38), this feature may be attributed to poorer mixing in this region. On the other hand, 400 K and 600 K cases show a more stratified structure in the axial direction. The 400 K case shows

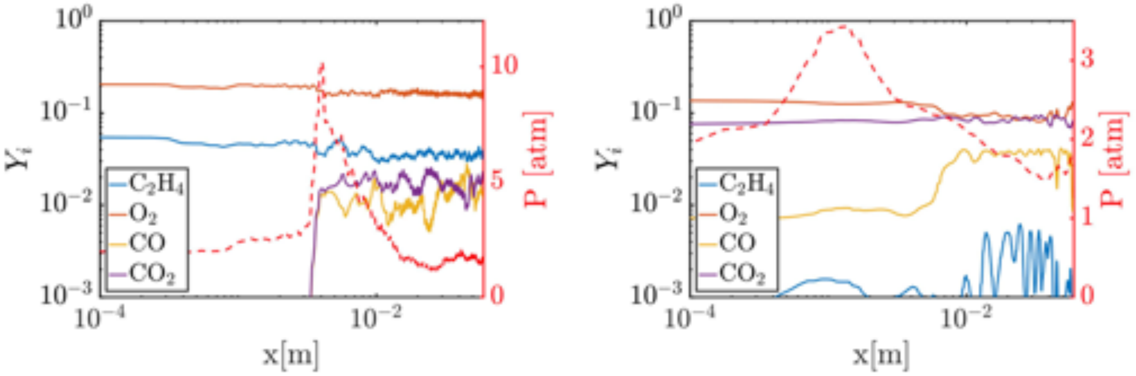

Figure 3.36: Species behavior and pressure profile across the shock for $T^0_{oxi} = 300$ K case. Left: outer wall. Right: mid-channel.

that the $\phi = 1.0$ region exists at the chamber bottom near the outer wall while these regions are found near the inner wall for the 600 K case. The interesting point here is that a stable wave cannot be formed for the 600 K air case as shown in Fig. 3.35. These results indicate that a higher degree of stratification leads to a reduction in detonation efficiency. Prior canonical simulations [54] show that stratification alters the detonation cell size and propagation features. Given this result, the current set of observations is not surprising. It is interesting that even when the air inflow is heated (600 K), the lack of adequate mixing can lead to unstable wave propagation.

Figure 3.41 shows the time history of the injection velocity for the fuel and oxidizer injector. The velocity is measured at the center of each injector on its exit plane. The time is normalized by the time required for a detonation wave to complete one cycle. Since the wave velocity cannot be calculated for the 600 K case, the wave speed of the 400 K case is used to normalize the time of the 600 K case. For all the cases, the velocity of the oxidizer injector is almost constant during the operation. This indicates that the wave in the chamber is too weak to affect the oxidizer injection behavior. This behavior is different from prior studies of hydrogen/air RDEs [51, 36], where the strong wave feedback into the oxidizer plenums would lead to periodically unchoked flow. More importantly, burnt gases from the detonation chamber could travel into the feed plenums, leading to changes in the ignition characteristics of the reactant gases. Here, however, the injection velocity recovers immediately after a wave passes through, thereby minimizing any flow back into the feed plenums.

Another useful metric in analyzing detonation performance is the heat release rate

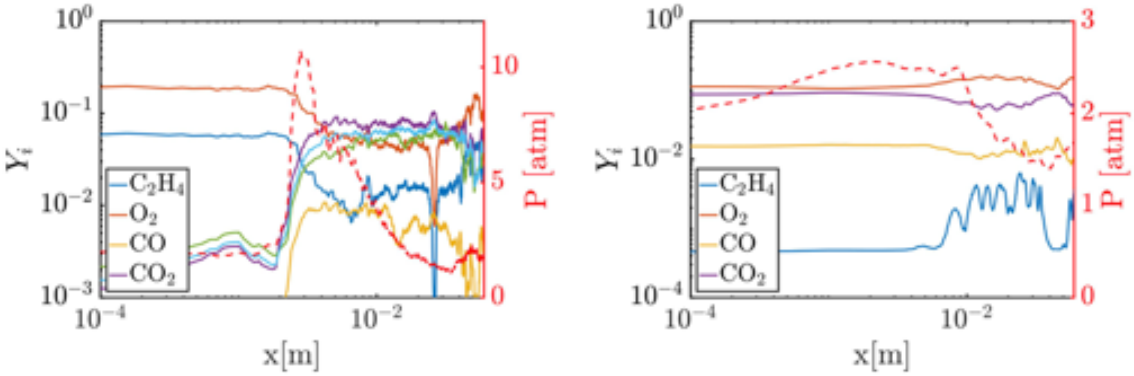

Figure 3.37: Species behavior and pressure profile across the shock for T^0_{oxi} = 400 K case. Left: outer wall. Right: mid-channel.

plotted as a function of pressure. In such pressure gain devices, the design goal is to support heat release at higher pressures. However, due to mixing inefficiencies and the finite rate of chemical reactions, achieving this ideal scenario is difficult. Figure 3.42 shows the heat release fraction for the three cases. In spite of the differences in spatial structure, all three cases produce similar heat release rates. While the peak pressure behind the wave can be significantly higher than the baseline pressure of 1 atm, much of the heat release happens in the 1-3 atm pressure range. This suggests that the compression wave is detached from the heat release region, and that the shock wave itself is not a continuous planar front but marked by small regions of compression waves. To complete the picture, Fig. 3.41 shows the Rankine-Hugoniot plot obtained from the pressure and specific volume at each grid point in the domain as a scatter plot. It is important to recognize that this data does not signal the progression of a single fluid element in the pressure-specific volume space (which is the original intent of this plot), but only shows the instantaneous states of the fluid inside the domain. It is seen that only the 400 K case shows fluid states with high degree of compression, corresponding to a detonation process. The other cases show lower pressure in much of the domain. These results can then be compared to the macroscopic quantities evaluated in Tab. 3.1. As expected, the 400 K case shows a higher specific impulse, due to the presence of high pressure regions within the domain.

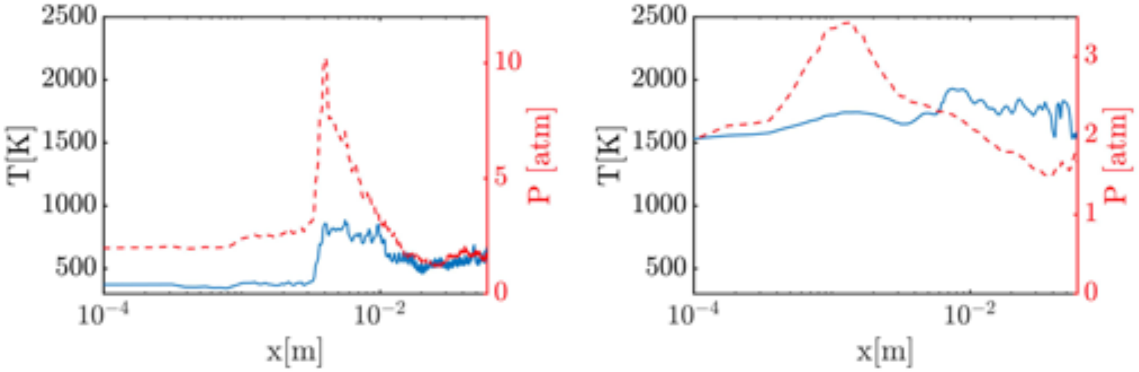

Figure 3.38: Temperature and pressure profiles across the shock for $T^0_{oxi} = 300$ K case. Left: outer wall. Right: mid-channel.

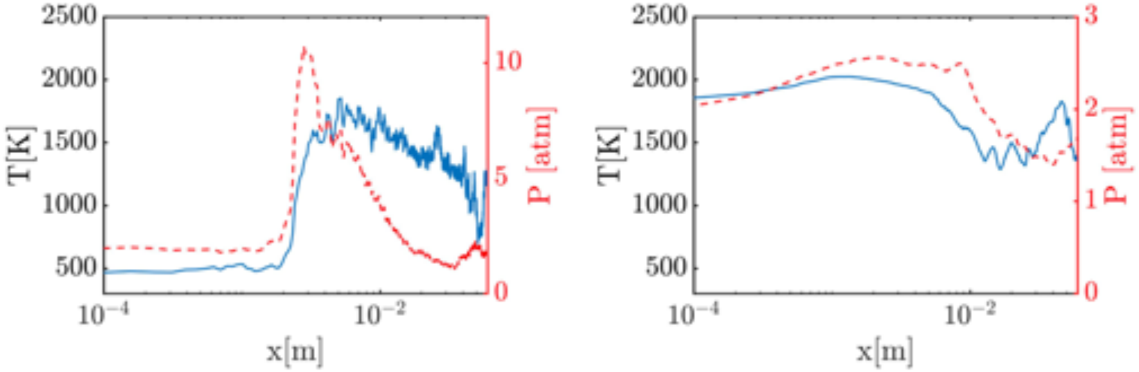

Figure 3.39: Temperature and pressure profiles across the shock for $T^0_{oxi} = 400$ K case. Left: outer wall. Right: mid-channel.

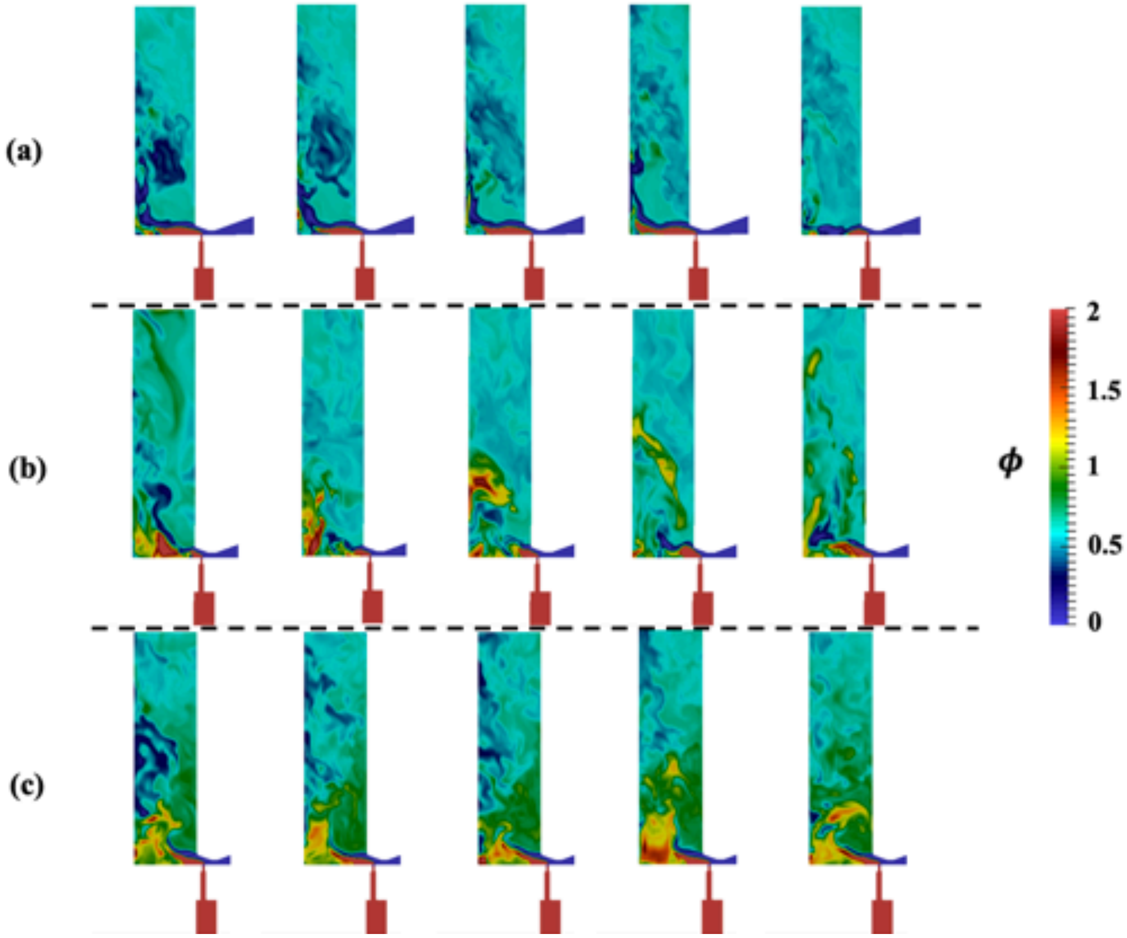

Figure 3.40: Time history of equivalence ratio at a cutting plane at the injector location for: a) $T^0_{oxi} = 300$ K, b) $T^0_{oxi} = 400$ K, and c) $T^0_{oxi} = 600$ K air cases.

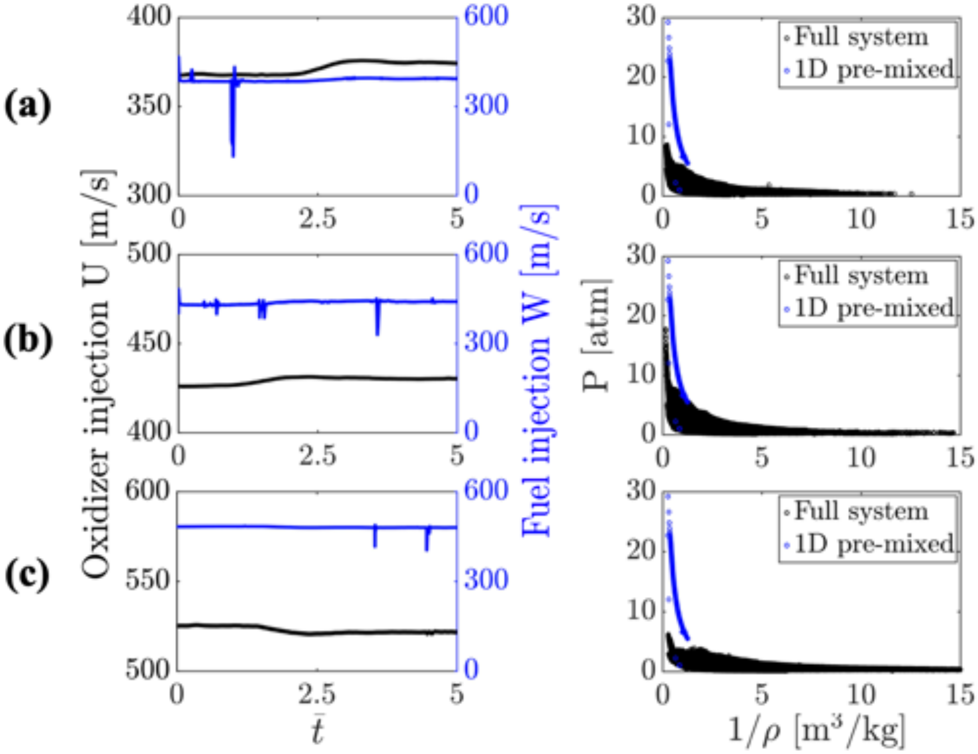

Figure 3.41: Left: time history of the injection velocity. Right: pressure vs. specific volume relation for a) T^0_{oxi} = 300 K, b) T^0_{oxi} = 400 K, and c) T^0_{oxi} = 600 K cases.

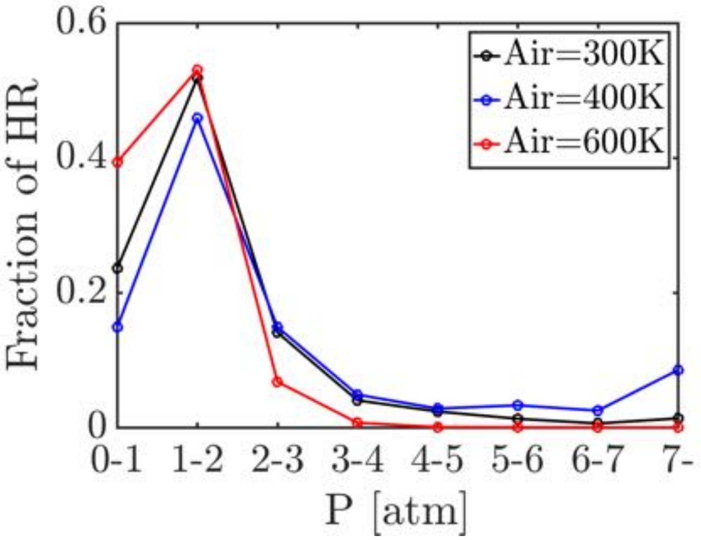

Figure 3.42: Heat release rate fraction plotted as a function of the local pressure for each case.

Bibliography

[1] Rankin, B. A., Richardson, D. R., Caswell, A. W., Naples, A., Hoke, J., and Schauer, F., “Imaging of OH$*Chemiluminescenceinan Optically Accessible Nonpremixed Rotating Detonation Engine,''$ 53

[2] Fotia, M. L., Schauer, F., Kaemming, T., and Hoke, J., “Experimental Study of the Performance of a Rotating Detonation Engine with Nozzle,” *Journal of Propulsion and Power*, Vol. 32, No. 3, May 2016, pp. 674–681.

[3] Roy, A., Ferguson, D. H., Sidwell, T., O'Meara, B., Strakey, P., Bedick, C., and Sisler, A., “Experimental Study of Rotating Detonation Combustor Performance under Preheat and Back Pressure Operation,” *55th AIAA Aerospace Sciences Meeting*, American Institute of Aeronautics and Astronautics, Jan. 2017.

[4] Schwer, D. and Kailasanath, K., “Feedback into Mixture Plenums in Rotating Detonation Engines,” *50th AIAA Aerospace Sciences Meeting including the New Horizons Forum and Aerospace Exposition*, American Institute of Aeronautics and Astronautics (AIAA), jan 2012.

[5] Rankin, B. A., Fotia, M. L., Naples, A. G., Stevens, C. A., Hoke, J. L., Kaemming, T. A., Theuerkauf, S. W., and Schauer, F. R., “Overview of Performance, Application, and Analysis of Rotating Detonation Engine Technologies,” *Journal of Propulsion and Power*, Vol. 33, No. 1, Jan. 2017, pp. 131–143.

[6] Gaillard, T., Davidenko, D., and Dupoirieux, F., “Numerical Optimisation in Non Reacting Conditions of the Injector Geometry for a Continuous Detonation Wave Rocket Engine,” *Acta Astronautica*, Vol. 111, jun 2015, pp. 334–344.

[7] Hall, J. M. and Petersen, E. L., "An optimized kinetics model for OH chemiluminescence at high temperatures and atmospheric pressures," *International Journal of Chemical Kinetics*, Vol. 38, No. 12, 2006, pp. 714–724.

[8] Hong, Z., Davidson, D. F., and Hanson, R. K., "An improved H2/O2 mechanism based on recent shock tube/laser absorption measurements," *Combustion and Flame*, Vol. 158, No. 4, April 2011, pp. 633–644.

[9] E, S. and J, S., "Validation of Detailed Reaction Mechanisms for Detonation Simulation," Tech. rep., Graduate Aeronautical Laboratories of the California Institute of Technology, 1999.

[10] White, L. and Gamba, M., "Underresolved absorption spectroscopy of OH radicals in flames using broadband UV LEDs," *Journal of Quantitative Spectroscopy and Radiative Transfer*, 2018.

[11] Gordon, S. and McBride, B. J., "Computer program for calculation of complex chemical equilibrium compositions and applications. Part 1: Analysis," 1994.

[12] Bykovskii, F. A., Zhdan, S. A., and Vedernikov, E. F., "Continuous Spin Detonations," *Journal of Propulsion and Power*, Vol. 22, No. 6, nov 2006, pp. 1204–1216.

[13] Frolov, S., Aksenov, V., Ivanov, V., and Shamshin, I., "Large-scale hydrogen–air continuous detonation combustor," *International Journal of Hydrogen Energy*, Vol. 40, No. 3, jan 2015, pp. 1616–1623.

[14] Anand, V., George, A. S., Driscoll, R., and Gutmark, E., "Longitudinal pulsed detonation instability in a rotating detonation combustor," *Experimental Thermal and Fluid Science*, Vol. 77, Oct. 2016, pp. 212–225.

[15] Alters, S., *Biology: Understanding Life*, Human and Introductory Biology Series, Jones and Barlette Publishers, 2000.

[16] Chacon, F., Feleo, A., and Gamba, M., "Impact of Inlet Area Ratio on the Operation of an Axial Air Inlet Configuration Rotating Detonation Combustor," *In proceedings AIAA Propulsion and Energy Forum*, 2019.

[17] Prakash, S., Fievet, R., and Raman, V., "Analysis of the detonation wave structure in a linearized rotating detonation engine," *Submitted to AIAA Journal*, 2019.

[18] Sato, T. and Raman, V., “Hydrocarbon Fuel Effects on Non-premixed Rotating Detonation Engine Performance,” *AIAA Scitech 2019 Forum*, , No. January, 2019.

[19] Chacon, F. and Gamba, M., “Detonation Wave Dynamics in a Rotating Detonation Engine,” *AIAA Scitech 2019 Forum*, American Institute of Aeronautics and Astronautics, jan 2019.

[20] Akselvoll, K. and Moin, P., “Large Eddy Simulation of Turbulent Confined Coannular Jets,” *J. Fluid Mech.*, Vol. 315, 1996, pp. 387–411.

[21] Sod, G. A., “A survey of several finite difference methods for systems of nonlinear hyperbolic conservation laws,” *J. Comput. Phys.*, Vol. 27, No. 1, 1978, pp. 1–31.

[22] Toro, E. F., Spruce, M., and Speares, W., “Restoration of the contact surface in the HLL-Riemann solver,” *Shock Waves*, Vol. 4, No. 1, 1994, pp. 25–34.

[23] Van Leer, B., “Towards the ultimate conservative difference scheme. V. A second-order sequel to Godunov’s method,” *J. Comput. Phys.*, Vol. 32, No. 1, 1979, pp. 101–136.

[24] Cockburn, B. and Shu, C.-W., “The Runge–Kutta discontinuous Galerkin method for conservation laws V: multidimensional systems,” *J. Comput. Phys.*, Vol. 141, No. 2, 1998, pp. 199–224.

[25] Cockburn, B. and Shu, C.-W., “TVB Runge-Kutta local projection discontinuous Galerkin finite element method for conservation laws. II. General framework,” *Math. Comp.*, Vol. 52, No. 186, 1989, pp. 411–435.

[26] Johnsen, E., Larsson, J., Bhagatwala, A. V., Cabot, W. H., Moin, P., Olson, B. J., Rawat, P. S., Shankar, S. K., SjÃ¶green, B., Yee, H., Zhong, X., and Lele, S. K., “Assessment of high-resolution methods for numerical simulations of compressible turbulence with shock waves,” *J. Comput. Phys.*, Vol. 229, No. 4, 2010, pp. 1213 – 1237.

[27] Powers, J. and Paolucci, S., “Accurate spatial resolution estimates for reactive supersonic flow with detailed chemistry,” *AIAA JOURNAL*, Vol. 43, No. 5, MAY 2005, pp. 1088–1099, AIAA 43rd Aerospace Sciences Meeting and Exhibit, Reno, NV, JAN 10-13, 2005.

[28] Shimizu, H., Tsuboi, N., and Hayashi, A., "Study of detailed chemical reaction model on hydrogen–air detonation," *39th AIAA aerospace sciences meeting and exhibit, Reno, AIAA paper*, Vol. 478, 2001, p. 2001.

[29] Oran, E. S., Weber., J. W., Stefaniw, E. I., Lefebvre, M. H., and Anderson., J. D., "A Numerical Study of a Two-Dimensional H2-O2-Ar Detonation Using a Detailed Chemical Reaction Model," *Combust. Flame*, Vol. 113, No. 1–2, 1998, pp. 147 – 163.

[30] Irvin Glassman, Richard A. Yetter, N. G. G., *Combustion*, 5th Edition, Academic Press, New York, 2014.

[31] Jachimowski, C. J., "Analytical study of the hydrogen-air reaction mechanism with application to scramjet combustion," Tech. rep., National Aeronautics and Space Administration, Hampton, VA (USA). Langley Research Center, 1988.

[32] Peters, N., *Turbulent Combustion*, Cambridge University Press, 2000.

[33] A. Cuoci, A. Frassoldati, T. F. a. E. R., "Laminar Diffusion Flamelet Models in Non-premixed Turbulent Combustion," *Progress in Energy and Combustion Science*, Vol. 10, 1984, pp. 319–339.

[34] Barlow, R. S. and Frank, J. H., "Effects of Turbulence on Specific Mass Fractions in Methane/Air Jet Flames," *Twenty-Seventh Symposium (International) on Combustion*, Vol. 27, 1998, pp. 1087–1095.

[35] Chacon, F. and Gamba, M., "Detonation Wave Dynamics in a Rotating Detonation Engine," AIAA Paper 2019-0198, (2019).

[36] Sato, T., Voelkel, S., and Raman, V., "Detailed Chemical Kinetics Based Simulation of Detonation-Containing Flows," American Society of Mechanical Engineers, Paper GT2018-75878, June (2018).

[37] Sato, T., Voelkel, S., and Raman, V., "Analysis of Detonation Structures with Hydrocarbon Fuels for Application Towards Rotating Detonation Engines," Analysis of detonation structures with hydrocarbon fuels for application towards rotating detonation engines, AIAA Paper 2018-4965, 2018, AIAA Paper 2018-4965, 2018.

[38] Goodwin, D. G., Moffat, H. K., and Speth, R. L., "Cantera: an object-oriented software toolkit for chemical kinetics, thermodynamics, and transport processes," `https://www.cantera.org`, 2017. Version 2.3.0.

[39] Mueller, M., Kim, T., Yetter, R., and Dryer, F., "Flow reactor studies and kinetic modeling of the H2/O2 reaction," *International Journal of Chemical Kinetics*, Vol. 31, No. 2, 1999, pp. 113–125.

[40] Greenshields, C. J., Weller, H. G., Gasparini, L., and Reese, J. M., "Implementation of Semi-discrete, Non-staggered Central Schemes in a Colocated, Polyhedral, Finite Volume Framework, for High-speed Viscous Flows," *International J. for Numerical Methods in Fluids*, Vol. 63, No. 1, 2010, pp. 1–21.

[41] Cocks, P. A., Holley, A. T., and Rankin, B. A., "High Fidelity Simulations of a Non-premixed Rotating Detonation Engine," AIAA Paper 2016-0125, 2016.

[42] Lietz, C., Desai, Y., Munipalli, R., Schumaker, S. A., and Sankaran, V., "Flowfield analysis of a 3D simulation of a rotating detonation rocket engine," Flowfield analysis of a 3D simulation of a rotating detonation rocket engine, AIAA Paper, 2019-1009, 2019, AIAA Paper, 2019-1009, 2019.

[43] Prakash, S., Fiévet, R., Raman, V., Burr, J., and Yu, K. H., "Analysis of the Detonation Wave Structure in a Linearized Rotating Detonation Engine," *AIAA Journal*, 2019, pp. 1–15.

[44] Schwer, D. and Kailasanath, K., "Fluid Dynamics of Rotating Detonation Engines with Hydrogen and Hydrocarbon Fuels," *Proc. Combust. Inst.*, Vol. 34, No. 2, 2013, pp. 1991–1998.

[45] Chacon, F. and Gamba, M., "OH PLIF Visualization of an Optically Accessible Rotating Detonation Combustor," AIAA Paper, 2019-4217, (2019).

[46] Chacon, F. and Gamba, M., "Study of Parasitic Combustion in an Optically Accessible Continuous Wave Rotating Detonation Engine," AIAA Paper, 2019-0473, (2019).

[47] Prakash, S., Fiévet, R., and Raman, V., "The Effect of Fuel Stratification on the Detonation Wave Structure," AIAA Paper 2019-1511, (2019).

[48] Daily, J. W., "Laser induced fluorescence spectroscopy in flames," *Prog. Energy and Combust. Science*, Vol. 23, No. 2, 1997, pp. 133–199.

[49] Burr, J. and Yu, K., "Detonation Wave Propagation in an Open Channel with Transverse Jets," AIAA Paper 2017-4908. (2017).

[50] Cho, K. Y., Codoni, J. R., Rankin, B. A., Hoke, J., and Schauer, F., "High-Repetition-Rate Chemiluminescence Imaging of a Rotating Detonation Engine," AIAA Paper 2016-1648, (2016).

[51] Rankin, B. A., Richardson, D. R., Caswell, A. W., Naples, A. G., Hoke, J. L., and Schauer, F. R., "Chemiluminescence Imaging of an Optically Accessible Non-premixed Rotating Detonation Engine," *Combustion and Flame*, Vol. 176, 2017, pp. 12–22.

[52] Marcantoni, L. G., Tamagno, J., and Elaskar, S., "Two-dimensional Numerical Simulations of Detonation Cellular Structures in H2O2Ar Mixtures with OpenFOAM®," *International Journal of Hydrogen Energy*, Vol. 42, No. 41, 2017, pp. 26102–26113.

[53] Kailasanath, K., "Recent Developments in the Research on Pulse Detonation Engines," *AIAA Journal*, Vol. 41, No. 2, 2003, pp. 145–159.

[54] Prakash, S., Fievet, R., and Raman, V., "The Effect of Fuel Stratification on the Detonation Wave Structure," AIAA Paper 2019-1511, (2019).